Title
Buoyancy transport mechanisms at continental shelf, surf zone, and estuarine scales

Author
Rodriguez, Angelica R

Publication Date
2019

UNIVERSITY OF CALIFORNIA SAN DIEGO

Buoyancy transport mechanisms at continental shelf, surf zone, and estuarine scales

A dissertation submitted in partial satisfaction of the
requirements for the degree
Doctor of Philosophy

in

Oceanography

by

Angelica Rita Rodriguez

Committee in charge:

Professor Sarah N. Giddings, Chair
Professor Falk Feddersen
Professor Sarah T. Gille
Professor Nirnimesh Kumar
Professor John L. Largier
Professor Eugene R. Pawlak

2019

The dissertation of Angelica Rita Rodriguez is approved, and it is acceptable in quality and form for publication on microfilm and electronically:

Chair

University of California San Diego

2019

DEDICATION

To Lily and Gaby, may your aspirations be limitless.

TABLE OF CONTENTS

LIST OF FIGURES

LIST OF TABLES

ACKNOWLEDGEMENTS

Chapter 1, in full, is a reprint of the paper “An oceanic heat transport pathway to the Amundsen Sea Embayment” published in Journal of Geophysical Research: Oceans by A. R. Rodriguez, M. R. Mazloff, and S. T. Gille in 2016. The dissertation author was the primary investigator and author of this paper.

Chapter 2, in part, is a reprint of the paper “Impacts of nearshore wave-current interaction on transport and mixing of small-scale buoyant plumes” published in Geophysical Research Letters by A. R. Rodriguez, S. N. Giddings, and N. Kumar in 2018. The dissertation author was the primary investigator and author of this paper.

Chapter 3 is currently being prepared for submission for publication of the material, and will be submitted as, “Lateral circulation in a low-inflow, seasonally hypersaline estuary” by Rodriguez, A. R., S. N. Giddings, J. J. Bredvik and S. E. Graham. The dissertation author was the primary investigator and author of this material.

VITA

2013	B. S. in Physics with Specialization in Earth Sciences and minor in Environmental Systems, University of California San Diego
2014	M. S. in Oceanography, University of California San Diego
2019	Ph. D. in Oceanography, University of California San Diego

PUBLICATIONS

Rodriguez, A. R., M. R. Mazloff, and S. T. Gille (2016), An oceanic heat transport pathway to the Amundsen Sea Embayment. *J. Geophys. Res. Oceans*, 121, 3337–3349, doi:10.1002/2015JC011402.131.

Rodriguez, A. R., S. N. Giddings, and N. Kumar (2018), Impacts of nearshore wave-current interaction on transport and mixing of small–scale buoyant plumes, *Geophys. Res. Lett.*, 45, 8379–8389, doi:10.1029/2018GL078328.

Rodriguez, A. R., S. N. Giddings, J. J. Bredvik, and S. E. Graham (2019), Lateral circulation in a low-inflow seasonally hypersaline estuary, in preparation.

ABSTRACT OF THE DISSERTATION

Buoyancy transport mechanisms at continental shelf, surf zone, and estuarine scales

by

Angelica Rita Rodriguez

Doctor of Philosophy in Oceanography

University of California San Diego, 2019

Professor Sarah N. Giddings, Chair

Oceanic uptake of atmospheric heat as well as incorporation of freshwater occurs across a vast range of spatial scales. Subsequently, these buoyant water masses are transported and modified within the ocean interior. Several physical processes relevant to the transport and mixing of heat and freshwater at an array of coastal scales, ranging from 1000s of km at the continental shelf slope to m within estuaries, are the topic of this dissertation. Analysis of a mix of data assimilative and idealized numerical models and field observations has yielded several impactful results that have direct relevance to coastal societies and ecosystems. At the largest scale, a mechanism that

delivers warm water within the Antarctic Circumpolar Current to the continental shelf slope where it crosses into the Amundsen Sea outer shelf has been identified. Vorticity input by wind-stress curl results in the poleward motion of heat that has potential to contribute to Antarctic Ice Sheet mass loss and consequently, global sea level rise. At the much smaller scales of the inner-shelf to surf zone, surface gravity wave induced onshore currents and mixing drastically modify low inflow estuarine freshwater outflows by reducing offshore transport and elongating alongshore and vertical extent within the surf zone. Because the freshwater distribution can be thought of as a proxy for tracers such as pollution, nutrients, or other plume constituents, these results have strong implications for beach contamination among other concerns that frequently arise due to the presence of buoyant outflows in the nearshore region. Within the estuary, lateral circulation moves channelized waters to regions of enhanced productivity over bathymetric shoals. In San Diego Bay, a low inflow estuary that lies in a unique parameter space among estuaries, this process is, at least in part, due to differential advection. Field data suggest that this process is sensitive to seasonal variation in buoyancy inputs and that circulation patterns may be altered in future climate change scenarios, thus impacting the wildlife that utilize the bay for breeding, habitat, and foraging. As such, the findings of this dissertation advance the fundamental science necessary to contribute to many societally relevant coastal management issues.

Introduction

The global ocean receives buoyancy fluxes across its boundaries through the transfer of heat, salt, and freshwater via turbulent and radiative fluxes, geothermal heating, the hydrologic cycle, river runoff, ice-melt, and brine rejection (*Groeskamp et al.*, 2019). Uptake of atmospheric heat as well as the incorporation of freshwater occurs across a vast array of spatial scales (*de Boyer Montégut et al.*, 2004; *Horner-Devine et al.*, 2015) . Subsequently, these water masses are modified and transported within the ocean interior (*Busecke and Abernathey*, 2019; *Ganachaud and Wunsch*, 2000; *Wijffels et al.*, 1992). The transport and mixing of heat and freshwater at three separate scales is the topic of this dissertation.

In the Southern Hemisphere polar region, the Antarctic Ice Sheet is most vulnerable to fluxes of heat from the impinging Southern Ocean where tilted isopycnal surfaces that outcrop within and south of the Antarctic Circumpolar Current give way to atmospheric ventilation and heat uptake (*Marshall and Speer*, 2012; *Sallée*, 2018) which has led to Southern Ocean warming over the last several decades (*Gille*, 2002, 2008; *Purkey et al.*, 2010, 2013; *Roemmich et al.*, 2015) that has been attributed to anthropogenic activity (*Swart et al.*, 2018). Chapter 1 of this dissertation identifies a large scale heat transport pathway in a data assimilative state estimate of the Southern Ocean that brings heat to the continental shelf, where it may contribute to basal melting of the floating ice shelves. Once on the shelf, the dynamics become ever more complicated due to thermohaline processes such as sea ice formation, brine rejection and sub-ice-shelf feedbacks (*Heywood et al.*, 2016; *Jenkins et al.*, 2016).

In temperate climates, freshwater plumes provide large contributions to the overall coastal buoyancy input (*Horner-Devine et al.*, 2015). The region of freshwater influence (ROFI; *Simpson et al.*, 1993) can migrate between the estuary and inner-shelf region. The mid-shelf, inner-shelf, and surf zone each exhibit different dominant cross-shelf exchange processes due to wave, wind, buoyancy, and tidal forcing (*Lentz and Fewings*, 2012). Within and across the surf zone, direct water mass exchange is induced by the onshore-directed flux due to surface wave orbital velocities and the accompanying offshore-directed return flow. Moreover, turbulent mixing is enhanced in the surf zone due to depth-limited wave breaking (*Feddersen*, 2012). The implications of these circulation and mixing processes on the transport and modification of small-scale freshwater plumes, such as those emanating from low-inflow estuaries (LIE; *Largier et al.*, 1997) and storm water outfalls, are examined in Chapter 2 through the use of idealized wave-hydrodynamic coupled simulations and scaling estimates.

In the absence of large river flow, the ROFI often resides within the estuarine region, or for LIEs, may be completely absent (*Largier et al.*, 1997). Inside the estuary, shallow water readily responds to solar heating and varying freshwater input, incorporating these active tracers into the estuarine circulation from tidal to seasonal time scales. On time scales longer than tidal, the classic estuarine balance is between pressure gradients and friction (*Hansen and Rattray*, 1965; *Geyer and MacCready*, 2014), but intratidal variability and lateral processes can alter this balance (*MacCready and Geyer*, 2010), modifying the distribution of salt and heat within the estuary (*Giddings et al.*, 2011). Additionally transverse circulation can generate frontogenesis (*Giddings et al.*, 2012) and facilitate shoal-channel exchange important for tracer transport and dispersion (*Lerczak and Geyer*, 2004; *MacCready and Geyer*, 2010; *Nunes and Simp-*

son, 1985; *Ralston and Stacey*, 2005; *Smith*, 1977). Estuarine transverse circulation in an LIE in the presence of seasonally varying buoyancy input is investigated using field observations in Chapter 3.

While there are many processes and spatio-temporal scales addressed here, this dissertation has advanced current understanding of several oceanographic physical processes pertinent to a number of problems facing coastal societies and ecosystems, including climate change, sea level rise, eutrophication, sediment transport, algal blooms, and pollution management. Moreover, this work has motivated follow-on studies and continued efforts to address these issues.

Chapter 1

An oceanic heat transport pathway to the Amundsen Sea Embayment

1.1 Abstract

The Amundsen Sea Embayment (ASE) on the West Antarctic coastline has been identified as a region of accelerated glacial melting. A Southern Ocean State Estimate (SOSE) is analyzed over the 2005–2010 time period in the Amundsen Sea region. The SOSE oceanic heat budget reveals that the contribution of parameterized small-scale mixing to the heat content of the ASE waters is small compared to advection and local air-sea heat flux, both of which contribute significantly to the heat content of the ASE waters. Above the permanent pycnocline, the local air-sea flux dominates the heat budget and is controlled by seasonal changes in sea ice coverage. Overall, between 2005 and 2010, the model shows a net heating in the surface above the pycnocline within the ASE. Sea water below the permanent pycnocline is isolated from the influence of air-sea heat fluxes, and thus, the divergence of heat advection is the major contributor to increased oceanic heat content of these waters. Oceanic transport of mass and heat

into the ASE is dominated by the cross-shelf input and is primarily geostrophic below the permanent pycnocline. Diagnosis of the time-mean SOSE vorticity budget along the continental shelf slope indicates that the cross-shelf transport is sustained by vorticity input from the localized wind-stress curl over the shelf break.

1.2 Introduction

The West Antarctic Ice Sheet (WAIS) contains 3.8 million km^3 of ice (*Oppenheimer*, 1998) and has the potential to cause global eustatic sea level rise of more than 3 m (*Bamber et al.*, 2009). Thus, the stability of WAIS has been the focus of much current research (*Joughin and Alley*, 2011; *Joughin et al.*, 2014; *Rignot et al.*, 2014). Satellite observations have shown that the most significant ice mass loss occurs along the Amundsen Sea coastline where several outlet glaciers drain into the embayment (*Pritchard et al.*, 2012; *Rignot et al.*, 2008, 2013). Ice flow in this region has increased by 77% since the 1970s (*Mouginot et al.*, 2014). Thinning of the floating ice-shelves and glacial grounding line retreat have been attributed to basal melting forced by heat input from inflowing Circumpolar Deep Water (CDW) (*Payne et al.*, 2004; *Wåhlin et al.*, 2010; *Walker et al.*, 2007). CDW in the Amundsen Sea Embayment (ASE) is typically 3–4°C warmer than the in situ freezing point and can be found as far south as the grounding zone of the Pine Island Glacier (PIG) (*Jacobs et al.*, 2011; *Jenkins et al.*, 2010). On monthly timescales, basal melt is thought to be driven largely by processes outside the subice-shelf cavity (*Heimbach and Losch*, 2012; *Schodlok et al.*, 2012). Hence, knowledge of the ocean state at the continental shelf slope is crucial to modeling studies of subice-shelf processes.

An understanding of the delivery mechanisms of CDW to the ASE is essential to predicting further influence of ocean forcing on the outlet glaciers of the ASE. A modeling study by *Thoma et al.* (2008) linked cross-continental-shelf CDW transport variability to zonal wind variability along the continental shelf edge due to migration of the Amundsen Sea Low. Building upon these results, *Steig et al.* (2012) proposed that tropical Pacific warming brought about the modern period of PIG retreat through a shift in the ASE zonal wind regime.

This study aims to investigate the large-scale pathways of CDW delivery to the ASE. Our primary tool is a Southern Ocean State Estimate (SOSE; *Mazloff et al.*, 2010), which provides a realistic model of the Southern Ocean dynamics and physical properties, as well as atmospheric forcing, through assimilation of all available observations. It uses the OCean Comprehensible Atlas (OCCA) global state estimate (*Forget*, 2010) to constrain the initial and northern boundary conditions and the European Centre for Medium-Range Weather Forecasts (ECMWF) Re-analysis (ERA)-Interim (http://www.ecmwf.int/) to constrain the meteorological boundary conditions at the ocean-atmosphere interface. Because the SOSE solution includes the entire Southern Ocean, it provides a perspective on the delivery of warm water to the ASE that is physically consistent with the Southern Ocean as a whole. This contrasts with previous regional modeling studies (e.g. *Heimbach and Losch*, 2012; *Thoma et al.*, 2008), which may be more sensitive to boundary and initial conditions. Being large-scale, however, does come at the expense of resolution, and we discuss these limitations in section 1.3.

The analysis tool, SOSE, is further discussed in section 1.3. In section 1.4 we compare SOSE to observations in the Amundsen Sea near the continental shelf and within the ASE. We diagnose the heat budget of the ASE waters along the continental shelf slope in section 1.5 with the goal of identifying the factors that most strongly dictate changes in the heat content of these waters. In section 1.6 we quantify mass and heat transports into and out of the embayment, and find that the oceanic transport of heat to the ASE is dominated by a time-mean geostrophic flow across the continental shelf slope. This transport is attributed to forcing by a strong local wind-stress curl that drives waters poleward onto the ASE continental shelf in section 1.7, followed by a summary and discussion in section 1.8.

1.3 The Southern Ocean State Estimate

SOSE, the primary tool in this study, is an eddy-permitting general circulation model constrained to observations. It uses the MITgcm configured with 1/6° horizontal resolution, 42 vertical levels of varying thickness, and a time step of 900 seconds (*Mazloff et al.*, 2010). SOSE employs a sea ice model based on the work of *Semtner* (1976) for the thermodynamics (*Fenty and Heimbach*, 2013) and on the work of *Hibler and Bryan* (1987) for the dynamics (*Losch et al.*, 2010; *Zhang and Hibler III*, 1997). SOSE observational constraints include Argo floats, conductivity-temperature-depth (CTD) casts, Southern Elephant Seals as Oceanographic Samplers (SEaOS) instrument mounted seal profiles, expendable bathythermograph (XBT) profiles, inverted echo sounders (IES), radiometric sea surface temperature measurements, altimetric observations, and sea ice cover observations.

For this study we use a SOSE solution for the years 2005–2010. The output, denoted iteration 100, is available from sose.ucsd.edu. We define the ASE as the region extending from the Antarctic coast to the continental shelf slope defined by an along-shelf coordinate that follows the 2600 m depth contour of the SOSE bathymetry between 124.25°W to 98.42°W, indicated by the red contour in Figure 1.1a. In situ observations in the ASE region, which were minimal from 2005 to 2007, but prevalent from 2008 to 2010, are indicated in Figure 1.1.

While SOSE is eddy-resolving equatorward of the ACC, the horizontal resolution is too coarse to resolve mesoscale structures at the latitude of the Antarctic con-

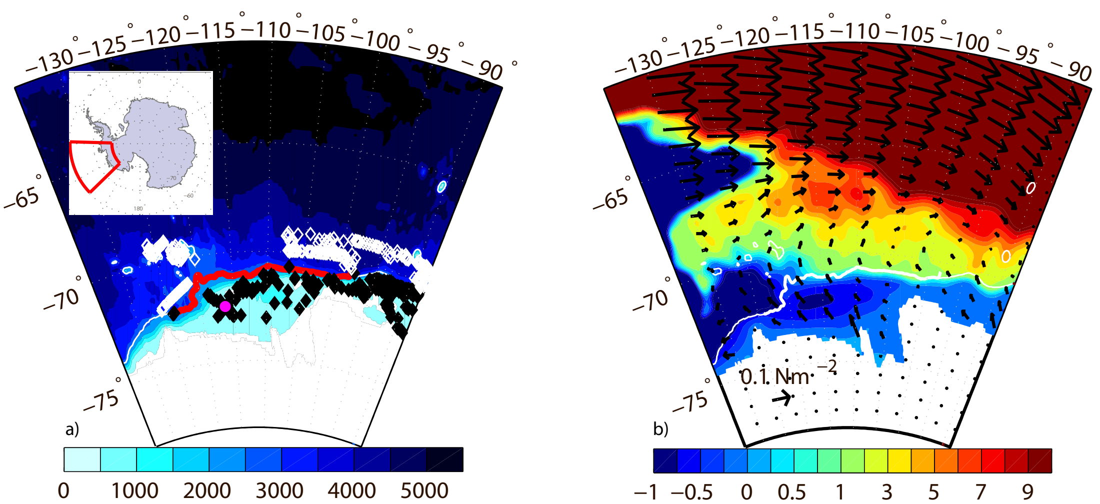

Figure 1.1: (a) The Amundsen Sea bathymetry (m) with 2005–2010 CTD, Argo, and SEaOS observation locations. White diamonds indicate observations north of the shelf break, while black diamonds indicate shallower observations. The magenta circle indicates the location of the mooring data presented in Figure 1.3. The red 2600 m depth contour indicates the perimeter of the ASE. For the purposes of this analysis, lateral boundaries of the ASE are at 124.25°W and 98.42°W. (b) The 2005–2010 time-mean streamfunction (Sv) with 2005–2010 time-mean wind-stress vectors. For reference, the 2600 m bathymetric contour of the continental shelf is also plotted in white to indicate the location of the shelf break relative to the time-mean currents.

tinental shelf slope, where the first baroclinic mode Rossby radius decreases to 5 km (*Venaille et al.*, 2011). However, the modeled heat transport into the ASE at the continental shelf slope is necessarily physically consistent with the ACC to the north, which is constrained to observations. Thus, the analysis carried out here is able to reveal the large-scale (greater than ∼75 km) pathways of heat transport to the ASE, as well as the dynamics governing these pathways on time-scales greater than 2 days. Dynamics occurring at smaller scales, including eddies and tides, also play a significant role in facilitating cross-shelf heat exchange in several different regions along the Antarctic continental shelf (*Martinson and McKee*, 2012; *Nøst et al.*, 2011; *Robertson*, 2013; *Stewart and Thompson*, 2015; *Thompson et al.*, 2014). The roles of these processes, and their interaction with the large-scale flow over sloping topography are beyond the scope of the present study.

1.4 Model Comparison to Observations

To determine if SOSE is consistent with the observed ASE properties we use CTD, Argo, and SEaOS profiles (depicted as diamonds in Figure 1.1a taken between 2005 and 2010. All seasons are represented in the available data sets, with the majority of wintertime observations from the SEaOS program. The last three years of the solution contain significantly more data than the first three years due to an increase in Argo profiling floats in the region. Observations taken south of the 2600 m isobath are indicated by filled black diamonds, while those just north of the ASE study domain are white and unfilled. Figures 1.2a and 1.2b depict the mean (blue) and standard deviation (black) of the observed potential temperature on and off of the shelf respectively. Observed potential temperatures on the shelf exhibit a deeper mixed layer with a more gradual thermocline than those off of the shelf. Both regions show strongest variability in the thermocline. The differences in structure between the model and observations are found in all seasons, with the greatest variability found above the 225 m permanent pycnocline.

The mean of the SOSE equivalent to the 2005–2010 observations of potential temperature is also plotted (cyan), along with the root-mean-squared difference of the model-observation misfit (red). In both regions, SOSE exhibits a mixed layer that is too thin, leading to a modeled thermocline that is shallower than observed. However, all observed water masses are exhibited in SOSE. Thus, though SOSE's mixed layer is biased shallow, it has the same structure and temperature as seen in observations. We are primarily interested in the movement of deep warm water across the continental shelf slope, as this is thought to be the primary source of heat driving increased basal melt rates of ASE outlet glaciers. Although an elevated thermocline indicates that the warm water reaches too high in the water column in SOSE, the modeled ocean temperature does have the same structure and magnitude as observed.

In SOSE, the potential temperature profile, referenced to 0 dbar, averaged along the continental shelf slope is near freezing (∼-1.7°C) at the surface and warms quickly with depth to peak at ∼1.6°C at 439 m depth (Figure 1.2c). The profile then decreases

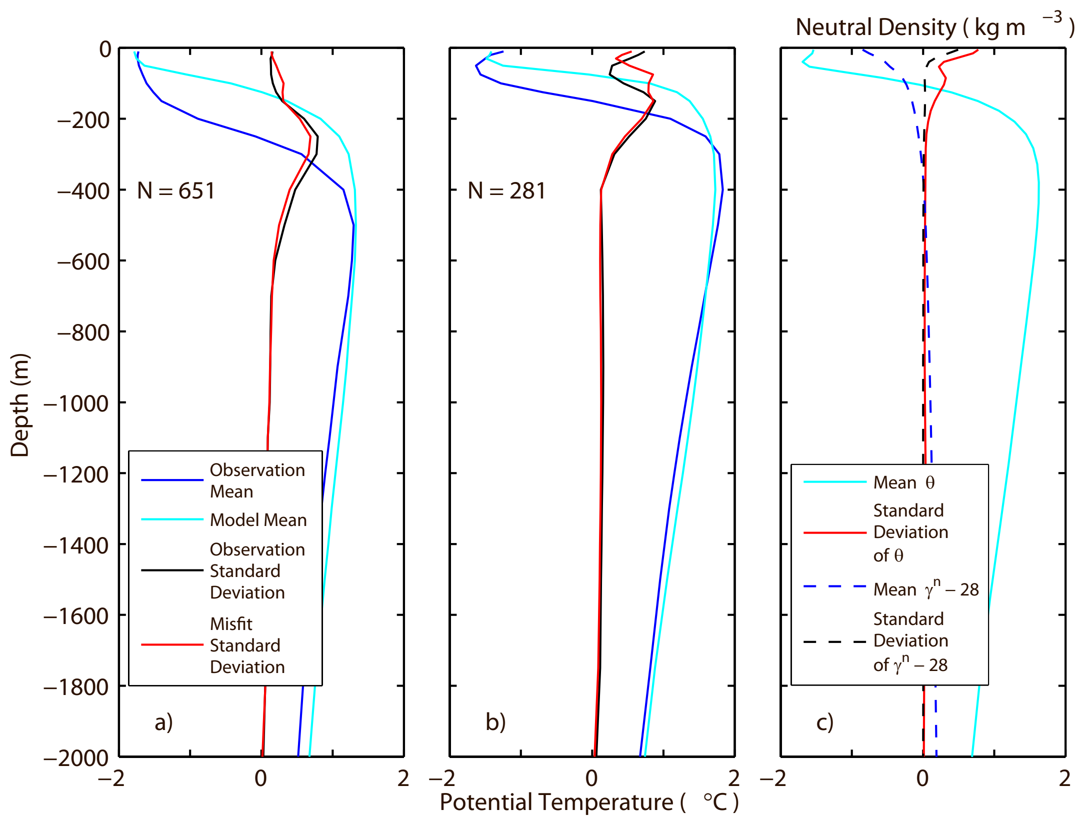

Figure 1.2: Mean potential temperature profiles (blue lines) of the 2005–2010 observations at (a) shallow locations (filled black diamonds in Figure 1.1a) and (b) deep locations (unfilled white diamonds in Figure 1.1a). N is the number of observed profiles for each regime. Also shown are the standard deviations of the mean profiles (black lines), mean potential temperature profiles (cyan lines) of the model equivalents to the observations, and standard deviation of the model misfit $(\text{model}_i - \text{observation}_i)$ (red lines). (c) Time-mean model temperatures (cyan line) and neutral density relative to 28 kg m^{-3} (blue dashed line) averaged along the 2600 m bathymetric contour that defines the northern edge of the ASE and temporal standard deviations (red and black dashed lines respectively).

with depth approaching 0°C at the bottom. These water temperatures have significant atmospheric-driven temporal variability in the upper 225 m but are relatively constant below that depth, as indicated by the temporal standard deviation (Figure 1.2c). Therefore, when discussing calculations involving model temperature, we separate the analysis into surface and subsurface boxes, separated in depth at 225 m.

The 2005–2010 time averaged SOSE neutral density along 225 m depth differs between the west end of the shelf and the east end by only 0.014 kg m^{-3}, with slightly warmer, lighter water to the east. Density classes below 225 m differ even less in the horizontal. Temporal variability below 225 m is minimal as well, as indicated by the black dashed line in Figure 1.2c. *Whitworth et al.* (1998) define CDW to be the water mass with neutral density between 28.00 kg m^{-3} and 28.27 kg m^{-3}. Several studies suggest that this water mass is the most significant to thermal forcing of ASE marine-terminating glaciers. We find this water mass along the continental shelf slope in SOSE, indicated by the mean neutral density profile (blue dashed line). This curve is shifted by the upper limit of CDW in the ASE (*Whitworth et al.*, 1998) ($\gamma^n - 28$ kg m^{-3}), and thus, negative values found in the upper water column indicate water masses lighter than CDW. The variability of water mass properties above and below 225 m depth is the basis for vertical separation of the heat budget and transport analysis described in sections 1.5 and 1.6.

The model velocity field from the year 2010 is compared to mooring observations located at 72.46°S, 116.35°W (Figure 1.1a). Figure 1.3 shows spectral estimates of the salt and temperature components of mass transport at 506-m depth, with transport defined in the direction of the principal component of horizontal velocity at this depth. Both the observed and modeled transports are in the direction of maximum variance. The salinity and temperature transports, uS and uT, are scaled to units of mass transport using $\partial\rho/\partial T|_S$ = -0.11 kg m^{-3} °C^{-1} and $\partial\rho/\partial S|_T$ = 0.80 kg m^{-3} PSU^{-1}. Daily averaged velocity, salinity and temperature in SOSE resolves spectral density at frequencies of 0.5 cycles per day and lower, while higher frequency variability is not resolved. At the resolved frequencies, the model is consistent with observations. The variance in the salinity component of modeled mass transport, 2.4×10^{-2} (kg s^{-1} m^{-2})^2, is five orders of magnitude higher than the variance of the temperature component of mass transport, 6.9×10^{-7} (kg s^{-1} m^{-2})^2, indicating that temperature at this depth is relatively steady during 2010 at this location . For the remainder of the analysis presented here, we focus on dynamics governing the heat budget on monthly time-scales and longer at spatial scales of 75 km and larger.

While SOSE captures the structure and magnitude of observed temperature in the ASE, as well as the energetics of the circulation, it does not employ an ice-shelf

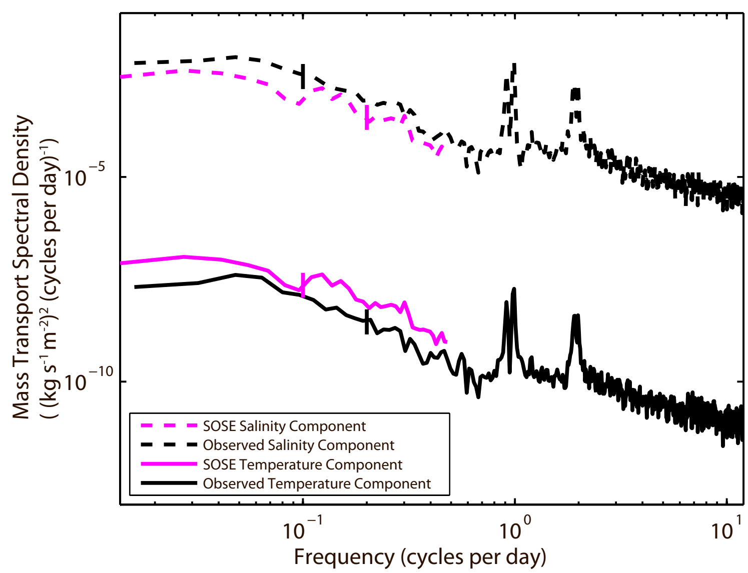

Figure 1.3: Comparison of salinity and temperature data observed from a mooring located at 72.46°S, 116.35°W (*Wåhlin et al.*, 2013) (black lines) to the SOSE equivalents (magenta lines). The figure shows spectral density of the salinity components (dashed lines) and temperature components (solid lines) of mass transports ((kg s^{-1} m^{-2})^2 (cycle per day)$^{-1}$) in the direction of the principal axis of velocity at 506 m depth. Vertical bars correspond to the 95% confidence interval that the estimated spectra is the true spectra.

model, and thus, while the oceanic heat budget is closed, it does not involve ice/ocean interactions that occur along the ice-sheet margin. In addition to modifying the continental shelf circulation that we do not adequately resolve, this interaction would decrease the total temperature tendency and input freshwater to the ocean system. Though ice-shelf and ocean interaction changes water mass properties and is important to quantify, its role in governing the transport of heat across the continental shelf slope is probably small and left for further investigation.

1.5 The Vertically Separated Heat Budget

In order to understand the processes most affecting the heat content of the ASE shelf waters during the years 2005 to 2010, we compute the time-varying potential temperature, referenced to 0 dbar,

$$\begin{aligned}
\underbrace{\theta_t}_{\text{tendency}} &= \underbrace{-u\theta_x - v\theta_y - w\theta_z}_{\text{advection}} + \underbrace{\nabla\cdot\kappa\nabla\theta + \nabla^2\cdot\kappa_4\nabla^2\theta + \mathcal{D}_{KPP} + \mathcal{D}_i}_{\text{diffusion}} + \underbrace{\mathcal{F}_{\text{atm}} + \mathcal{F}_{\text{ice}}}_{\text{forcing}} \\
&= -\mathbf{u}\cdot\nabla\theta + \mathcal{D} + \mathcal{F}, \qquad (1.1)
\end{aligned}$$

where $\mathbf{u} = u\hat{\mathbf{i}} + v\hat{\mathbf{j}} + w\hat{\mathbf{k}}$ is the velocity vector, κ and κ_4 are the harmonic and biharmonic diffusion coefficients, $\mathcal{D}_{KPP}$ represents the parameterization of mixed-layer turbulence by the K-Profile Parameterization (KPP; *Large et al.* 1994), $\mathcal{D}_i$ represents implicit diffusion in the model, and $\mathcal{F}_{\text{ice}}$ and $\mathcal{F}_{\text{atm}}$ represent ocean exchanges with sea ice and the atmosphere. Here the model assumes incompressible flow ($\nabla\cdot\mathbf{u} = 0$). SOSE solves for each individual term in 1.1. We group the divergence of the advective terms into one *advection* term ($\mathbf{u}\cdot\nabla\theta$); the harmonic, bi-harmonic, parameterized, and implicit diffusion terms into a *diffusion* term ($\mathcal{D}$); and fluxes from both sea ice and the atmosphere into one *forcing* term ($\mathcal{F}$). Since we separate surface and subsurface waters by depth, not density, the advective term includes adiabatic vertical advection between the two boxes, discussed in greater detail in subsection 1.6.2 on heat transports. Profiles of $\mathcal{D}_{KPP}$ diffusion coefficient (not shown) indicate strong mixing in the top 50 m of the water column and rapid decay to a constant value of 10^{-5} m^2 s^{-1} below 150 m depth. However, $\mathcal{D}_{KPP}$ has not been validated or tuned for the conditions found on the Amundsen Sea Continental Shelf. The shallow thermocline bias identified in section 1.4 is likely a result of too shallow parameterized mixing.

We consider three components governing the temperature tendency: advection by ocean currents, parameterized turbulent mixing, and external forcing. Over the six years analyzed, the net mass divergence in the modeled ASE is negligible, so the ASE heat budget is well approximated by integrating equation 1.1 over the volume of the ASE and multiplying by the specific heat capacity, $C_v = 3985$ J kg^{-1}°C^{-1}, and mean seawater density, $\rho_0 = 1035$ kg m^{-3}. This formulation is consistent with that of *Warren* (1999).

Time series of the surface heat budget terms integrated over the volume of the ASE study domain reveal that at times of low ice concentration atmospheric forcing dominates the budget, with heat input reaching a magnitude of 46.3 TW (Figure 1.4b). Heat input from advection has a maximum of 17.2 TW and governs the heat content when sea ice is insulating the ocean from the atmosphere. The diffusive heat flux is an order of magnitude smaller than the tendency throughout 2005–2010. Temporal integration of the surface heat budget terms via a cumulative sum in time confirms that the temperature tendency primarily tracks atmospheric forcing throughout 2005–2010 (Figure 1.4d). Strong atmospheric cooling in the fall combined with relatively weak cooling in winter and spring dominate significant atmospheric heating in austral summer, resulting in a net heat flux from the ASE to the atmosphere. Oceanic heat transport compensates the atmospheric cooling, averaging 1.29 TW and thus contributing 24.5×10^{19} J of

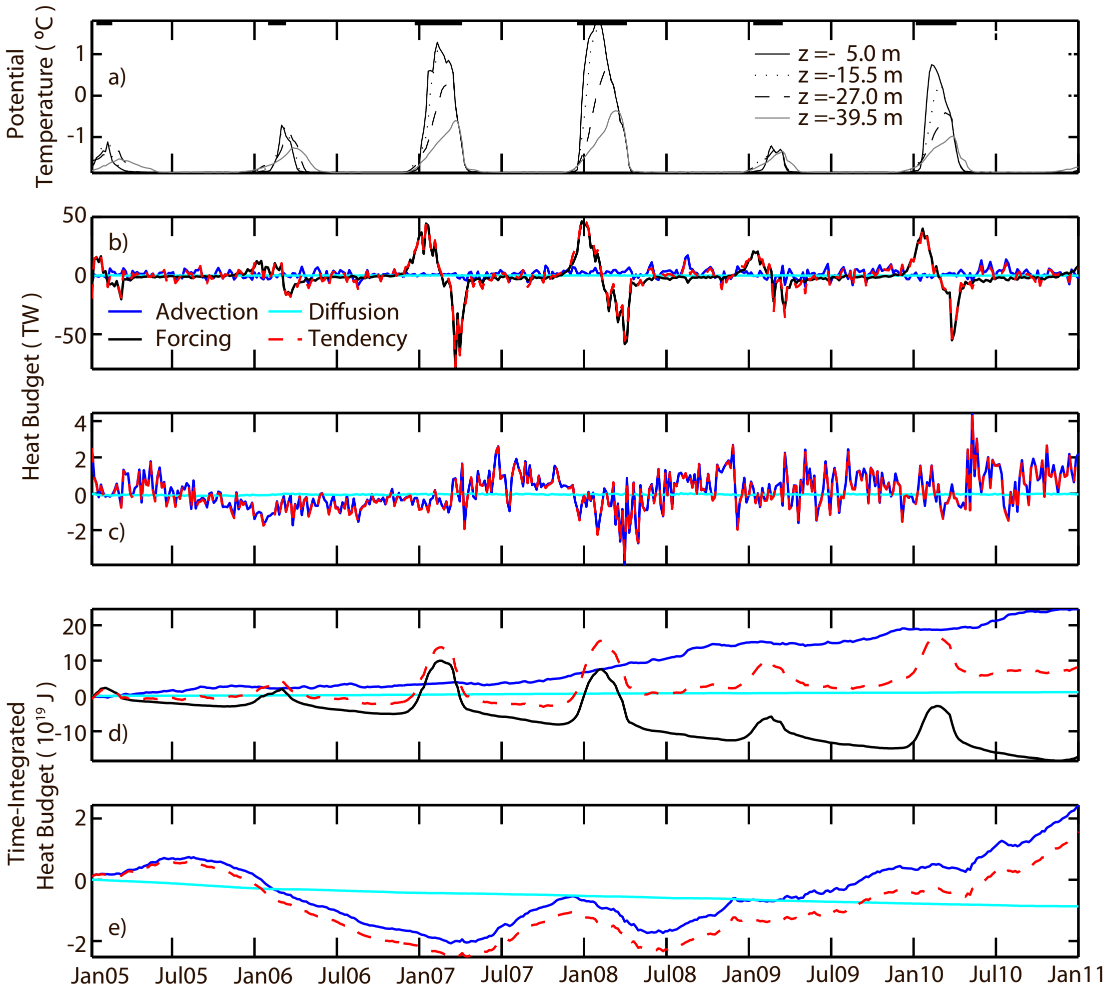

Figure 1.4: (a) Potential temperature averaged along the 2600 m isobath at four depths near the ocean surface with bold black lines placed at the maximum temperature value depicting the length of time that sea ice covers less than 65% of the ASE. (b) Heat budget above 225 m depth (surface). (c) Heat budget below 225 m depth (bottom). The blue lines in Figure 1.4b and 1.4c are the same as the blue lines in Figure 1.5a and 1.5b respectively. (d) Time-integrated surface heat budget. (e) Time-integrated bottom box heat budget. For panels (b)–(e), the red dashed line is the total tendency, the black line is the atmospheric forcing, the blue line is advection, and the cyan line is diffusion.

advective heating between 2005–2010. The combined effect of ocean heat transport and atmospheric and sea ice exchange is a net increase in heat content of the ASE surface waters of 8.24×10^{19} J, equivalent to a warming of 0.34 °C, over the 6 year simulation.

Below 225 meters depth advection and diffusion govern the heat budget, since atmospheric fluxes do not directly reach these depths. Advective heat transport dominates over the diffusive heat fluxes and therefore dictates the tendency (Figure 1.4c). The time-integrated subsurface heat budget (Figure 1.4e) shows a cooling trend between July 2005 and April 2007 with a subsequent increase and decrease over the next year, leading to a consistent warming trend between July 2008 and December 2010. The time-integrated tendency yields a total change in heat content of 1.57×10^{19} J, equivalent to a volume average change in θ of 0.02 °C, in the waters in the ASE below 225 m depth over the 6-year simulation, with much of this heating occurring between 2008 and 2010.

1.6 Transport Calculations

1.6.1 Vertically Separated Mass Transports

Strong currents, which are associated with the Southern Antarctic Circumpolar Current Front (SACCF), are found north of the continental shelf (Figure 1.1b). The southward meander of the Antarctic Circumpolar Current (ACC) in this region can be explained, in part, by wind-stress curl, which is consistent with the local Sverdrup balance. The 2005 to 2010 time-averaged winds over the Amundsen Sea are westerly and almost completely zonal north of 65°S. Over the ASE the mean winds are katabatic, blowing from the continent in the northward direction. The mean winds between the ASE and 65°S transition from northward to eastward, and thus exhibit a significant curl. A measure of how the ASE circulation couples with the Southern Ocean to the north can be evaluated by quantifying the total mass transport across each boundary of the study domain (Table 1.1). The 6-year mean and standard deviation of the transports reveal an on-shelf flow of 1.23 Sv $\pm$ 0.73 Sv, with highly variable compensating outflows at the lateral study domain boundaries. The annual means of the on-shelf flow are low in 2005 and 2006, but significant for the remaining years. The annual means of the along-shelf

Table 1.1: Mass Transports

Transports (Sv)	Along-shelf from the west at 124.25°W	Along-shelf from the east at 98.42°W	Cross-shelf
2005	-0.05±2.22	-1.27±0.93	1.32±0.64
2006	0.72±0.72	-1.36±0.69	0.64±0.51
2007	-0.65±1.08	-0.75±1.00	1.40±0.81
2008	-0.71±1.30	-0.33±1.22	1.04±0.58
2009	-1.02±1.20	-0.25±1.00	1.27±0.65
2010	-1.81±1.13	-0.10±0.94	1.71±0.67
6 year	-0.59±1.36	-0.64±1.10	1.23±0.73

flow have the same sign over most of the time period, but these transports are so variable that the mean is insignificant.

1.6.2 Vertically Separated Heat Transports

The ocean currents of the Amundsen Sea carry significant amounts of heat on and off the shelf. The advective term in equation 1.1 is given by the divergence of potential temperature transport into and out of the ASE. We calculate this transport at each domain boundary by integrating the normal component of $\mathbf{u}\theta$ in the vertical and along the length of the boundary. The sum of temperature transports across each domain boundary is equal to the advective contribution to the temperature tendency and can be expressed in units of heat by multiplying by the C_v and ρ_0.

The heat transport between the upper and lower boxes is taken into account when calculating the net transport, and is shown in Figure 1.5. By definition, the vertical flux that decreases heat content in one box, increases the heat content of the other box. The 2005–2010 mean vertical advective flux is 0.35 TW from the deeper box to the shallower box. However, this transport is adiabatic and not directly indicative of diapycnal fluxes. While this value is comparable to the net transport in the time-mean, the time-varying vertical transport remains an order of magnitude smaller than the horizontal transports.

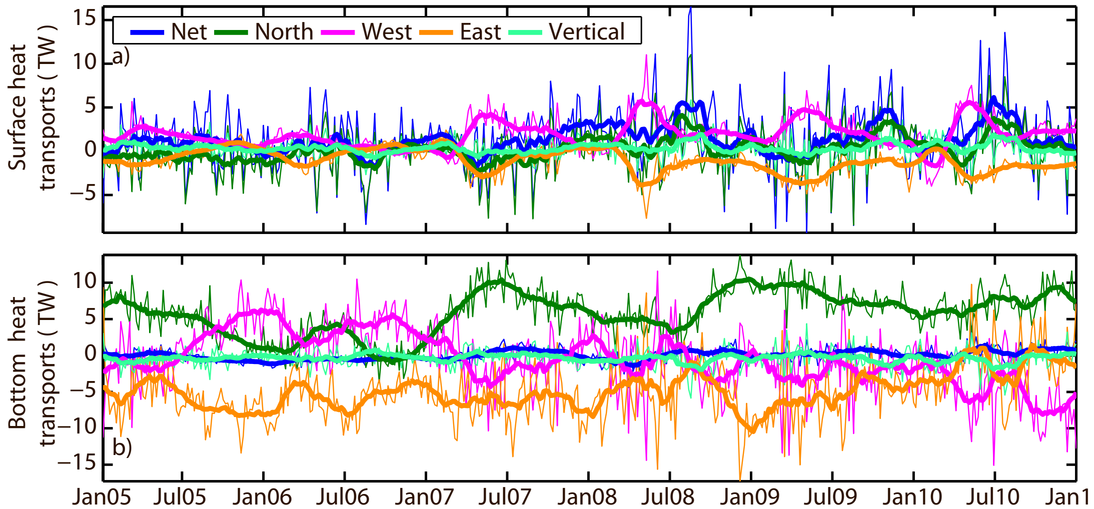

Figure 1.5: (a) Surface box advective heat transports. (b) Bottom box advective heat transports. The blue line is the net transport, the dark green line is the cross-shelf transport, the orange line is the along-shelf transport from the east across 98.42°W, the magenta line is the along-shelf transport from the west across 124.25°W, and the light green line is the vertical transport between the two boxes. The thick lines are a 1 month moving average for easier visualization.

Time series of the heat transports within the surface box (Figure 1.5a) show large temporal variability relative to the mean, particularly in the cross-shelf advective transport (green line) with a maximum net transport of 11.05 TW and a minimum of -8.43 TW. Consequently, the net heat transport divergence (blue line) in the ASE also varies significantly from month to month. Heat transports into the bottom box have lower variance (Figure 1.5b). With the exception of two short periods in 2007, the cross-shelf heat transport remains positive throughout 2005–2010, with a maximum of 13.81 TW occurring in December 2008. As with the mass transports, heat generally flows out of the ASE at the east and west study domain boundaries, offsetting the cross-shelf input.

Table 1.2 provides a summary of the annually averaged heat transport across each border of the study domain, as well as the corresponding net advective heat transport divergence. In the surface box, annually averaged total net fluxes remain positive from 2005 through 2010. Mean values indicate that heat is advected in from the west across 124.25°W with an outflow at 98.42°W. However, these fluxes are highly variable with large standard deviations compared to the mean values. This is also the case for the cross-shelf transport with a 6 year mean flux of 0.20 TW and a standard deviation of 2.74 TW. At depth, the heat advection follows the same circulation pattern as the mass transports, into the ASE across the shelf, and out of the bay at both lateral study domain boundaries except in 2005 and 2006, when heat and mass transport are into the domain from the west across 124.25°W. There is significant variation in the along-shelf flow, as indicated by the standard deviations listed in Table 1.2. The cross-shelf flow, however, maintains a significant positive annual mean, with a 6 year average magnitude of 5.85 TW and standard deviation of 3.35 TW. The dynamics driving cross-shelf

Table 1.2: Advective Heat Transports

Upper box fluxes (TW)	Along-shelf from the west at 124.25°W	Along-shelf from the east at 98.42°W	Cross-shelf	Total net flux
2005	1.54±0.96	-0.38±1.06	-0.79±2.03	0.78±2.85
2006	0.77±0.89	-0.30±0.96	-0.30±2.32	0.32±3.00
2007	1.91±1.91	-0.56±1.57	-0.40±2.40	1.11±2.84
2008	2.42±2.07	-1.37±1.65	1.03±3.07	2.67±3.84
2009	2.28±1.63	-2.18±1.20	0.80±3.17	1.19±4.26
2010	2.11±2.47	-1.61±1.15	0.85±2.74	1.86±3.64

Bottom box fluxes (TW)	Along-shelf from the west at 124.25°W	Along-shelf from the east at 98.42°W	Cross-shelf	Total net flux
2005	1.12±4.12	-5.80±3.49	4.88±2.76	-0.21±0.71
2006	3.84±2.81	-5.64±2.72	1.40±2.31	-0.54±0.46
2007	-0.77±3.66	-6.19±3.21	7.37±2.70	0.22±0.86
2008	-0.71±4.39	-4.85±4.67	6.06±2.90	-0.10±1.16
2009	-2.06±3.81	-5.56±3.75	8.17±2.00	0.26±0.80
2010	-4.81±4.22	-1.27±4.06	7.13±2.20	0.53±1.06

advection into the ASE are further examined in the following sections.

1.6.3 Total Cross-shelf Heat Transport Decomposition

The main source of heat to the ASE is the divergence of temperature advection in the waters below 225 m. The volume-integrated heat budget is highly variable, but further analysis of the circulation of mass and heat in the ASE reveals that the variance is due to the outflow of heat along the shelf at the longitudinal boundaries, while the cross-shelf transports are comparatively steady in time. The cross-shelf transports can be decomposed into geostrophic and ageostrophic components such that $\mathbf{u}^{\perp} = \mathbf{u}_g^{\perp} + \mathbf{u}_a^{\perp}$, where $\mathbf{u}_g = (f\rho)^{-1}(-p_y\hat{\mathbf{i}} + p_x\hat{\mathbf{j}})$ and $\mathbf{u}_g^{\perp}$ is the component of velocity normal to the continental shelf cross section that is in balance with the pressure gradient. The ageostrophic velocity, $\mathbf{u}_a$, includes all motions not in balance with the pressure gradient. Additionally, the total transport can be decomposed into the time-mean and eddy components, such that $\mathbf{u}^{\perp} = \overline{\mathbf{u}^{\perp}} + \mathbf{u}^{\perp\prime}$, where the bar denotes the time-mean and the prime denotes deviations from this mean. The temperature transport then becomes

$$\overline{\mathbf{u}^{\perp}\theta} = \overline{\mathbf{u}_g^{\perp}}\,\overline{\theta} + \overline{\mathbf{u}_g^{\perp\prime}\theta'} + \overline{\mathbf{u}_a^{\perp}\theta}. \tag{1.2}$$

Temperature transports coming into the embayment across the continental shelf slope are dominated by the time-mean geostrophic flow, $\overline{\mathbf{u}_g^{\perp}}\;\overline{\theta}$ (Figure 1.6). The majority of this transport is a result of the meridional flow across the slope towards the ASE ice-shelves. Unsurprisingly, given the resolution of SOSE, the eddy contribution is small, and ageostrophic motions, such as Ekman transport, are surface intensified. Though the shelf slope is steep enough to act as a strong topographic barrier, there is nonetheless significant time-mean cross-shelf flow.

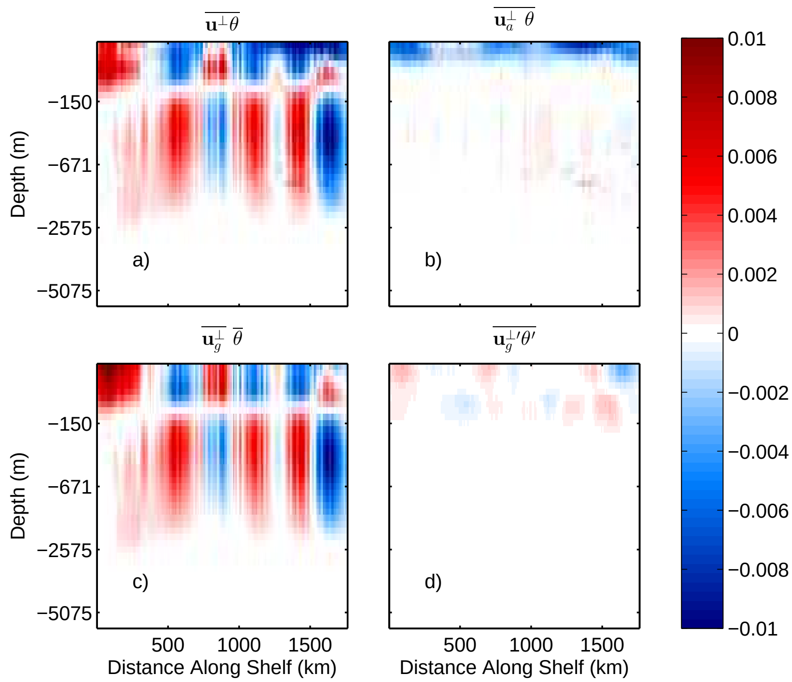

Figure 1.6: Temperature transports, in °C m s^{-1}, across the continental shelf given by equation 1.2, smoothed with a ~160 km running mean. The along-shelf distance is pictured by the red contour in Figure 1.1a from west to east. (a) Total time-mean transport. (b) Total ageostrophic component of the total time-mean transport. (c) Time-mean geostrophic component of the total time-mean transport. (d) Geostrophic eddy transport.

1.7 The Total Vorticity Budget

In order to identify the dominant mechanism driving the time-mean cross-shelf transport shown in Figure 1.6, we assess the full SOSE vorticity budget along the continental shelf slope. The vorticity tendency is

$$\underbrace{\zeta_t}_{\text{tendency}} + \underbrace{\beta v}_{\text{mean transport}} - \underbrace{\nabla \times \frac{\tau}{\rho}}_{\text{wind forcing}} - \underbrace{f w_z}_{\text{stretching}} + \underbrace{\nabla \times (\mathbf{u} \cdot \nabla \mathbf{u})}_{\text{advection}} - \underbrace{\nabla \times (\mathbf{V})}_{\text{viscosity}} = 0. \tag{1.3}$$

A derivation and description of this equation is in the Appendix 1.A. Cross sections of the time-mean vorticity budget terms as a function of along continental shelf distance are shown in Figure 1.7. The time-mean total vorticity tendency is negligible compared to the other terms in equation 1.3. The meridional transport term, βv, provides the dominant contribution to cross-shelf heat transport when the shelf is zonally oriented, as is primarily the case in the Amundsen Sea. In most regions, the continental shelf slope serves as a barrier to flow penetrating the shelf region due to vorticity constraints. Here, however, this is not the case. Figure 1.6 shows temperature transport normal to the shelf-slope to be strong in many regions along the length of the ASE.

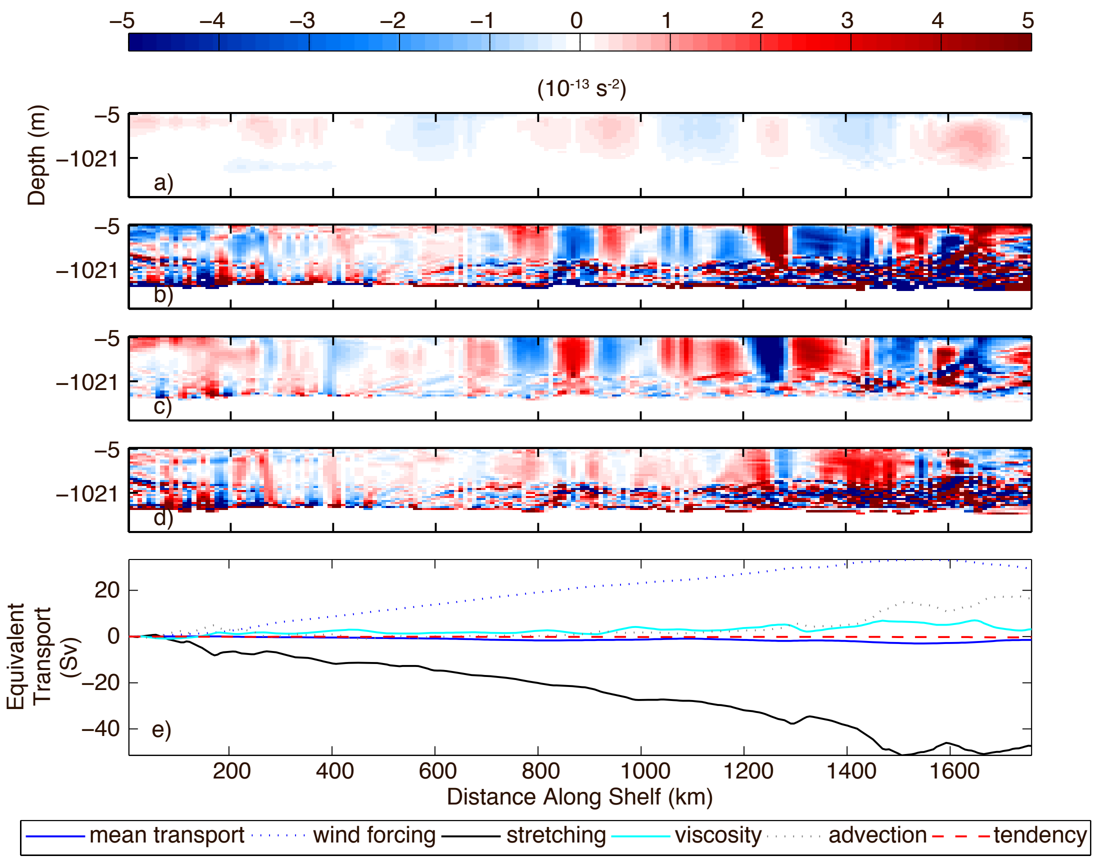

Figure 1.7: Time-mean vorticity budget, in $\times 10^{-13}$ s^{-2}, along the continental shelf given by equation 1.3. The along-shelf distance is pictured by the red contour in Figure 1.1a from west to east. (a) Mean transport: βv. (b) Wind forcing + stretching: $-\nabla \times (\tau/\rho) - f w_z$. (c) Advection: $\nabla \times (\mathbf{u} \cdot \nabla \mathbf{u})$. (d) Viscosity: $-\nabla \times (\mathbf{V})$. (e) Vertically integrated terms as a cumulative integral along the shelf slope, divided by $\beta \times 10^6$, giving units of transport (Sv).

The cross sections shown in Figure 1.7 depict noisy regions near the ocean floor extending into the water column, where the balance is complex. Here the on-shelf flow (βv) reduces to a minimal value, and bottom boundary layer theory may more appropriately describe the dynamics. Figure 1.7e shows the along-shelf integral of the terms in equation 1.3 vertically integrated from the surface to 1904 m divided by $\beta \times 10^6$ so that the units are that of volume transport in Sverdrups. Negative values indicate southward transport, i.e. toward the ASE. From this line plot it is clear that the net transport is primarily negative, as is the stretching term, while the wind-stress curl, nonlinear advection, and viscous terms are primarily positive, balancing the vorticity budget to give 0.31 Sv total tendency over the 6 year mean. The 6 year mean balance integrated along the shelf is

$$\begin{aligned}
(\beta \times 10^6)^{-1} \Big(\zeta_t + \beta v - \nabla \times \frac{\tau}{\rho} - f w_z + \nabla \times (\mathbf{u} \cdot \nabla \mathbf{u}) - \nabla \times (\mathbf{V}) \Big) &= 0 \\
-0.31 \text{ Sv} - 1.50 \text{ Sv} + 29.34 \text{ Sv} - 47.35 \text{ Sv} + 16.64 \text{ Sv} + 3.18 \text{ Sv} &= 0.
\end{aligned}$$

Thus, wind forcing, $-\nabla \times (\tau/\rho)$, along with non-linear and viscous terms, are primarily balanced by water column stretching, $-f w_z$. The residual sustains a time-mean meridional flow, βv, across the shelf slope. Stretching strongly counteracts on-shelf flow, but the input of vorticity from the wind-stress curl, augmented by interactions with open ocean currents, is enough to drive a $\sim$1 Sv flow into the ASE from the open ocean.

1.8 Summary and Discussion

Ice mass loss from the WAIS outlet glaciers along the Amundsen Sea coastline has been attributed to basal melting forced by CDW found on the ASE continental shelf (*Jenkins et al.*, 2010; *Pritchard et al.*, 2012; *Wåhlin et al.*, 2013; *Walker et al.*, 2007). Changing oceanic circulation may play a significant role in delivering heat to the grounding zone of the ASE outlet glaciers (*Holland et al.*, 2008). We have used a state estimate of the Southern Ocean to identify a heat transport pathway to the ASE. Though we do not attempt to describe the circulation that occurs on the continental shelf in detail, we do identify a physical mechanism that delivers CDW to the shelf slope where it crosses into the embayment. In the Amundsen Sea region, the southern branch of the Antarctic Circumpolar Current system veers southeastward with a transport of over 1 Sv just north of the shelf break (Figure 1.1b). Relatively warm CDW crosses the steep continental shelf into the ASE at several places along the shelf, with a consistently positive integrated temperature transport throughout 2005–2010. We find that heat is transported across the shelf at all depths. Our primary focus, however, is on the warm CDW found at depths below the permanent pycnocline ($\gamma^n \geq 28$ kg m^{-3}), as these waters are of the density class most likely to have direct bearing on basal melting. On the ASE shelf the permanent pycnocline in SOSE is found at about 225 m. Below this depth the ASE heat budget is dominated by the divergence of heat advection across the ASE boundaries, while diffusion acts to cool the shelf waters to a lesser extent. The result that heat diffusion across the permanent pycnocline is small should be taken with caution until observations can confirm or refute this hypothesis. Below 225 m depth, heat primarily enters the ASE from across the continental shelf break, exiting along the coast across the longitudinal boundaries of our ASE study region, 124.25°W and 98.42°W.

Previous studies have concurred that there is an oceanic heat transport pathway to the ASE (*Assmann et al.*, 2013; *Martinson and McKee*, 2012; *St-Laurent et al.*, 2013; *Stewart and Thompson*, 2015; *Walker et al.*, 2013). However, there has been no consensus as to what dynamics govern this pathway. There are many possible mechanisms including upwelling facilitated through surface Ekman tranport, eddies, tides, and frictional processes (*Assmann et al.*, 2013; *Robertson*, 2013; *Stewart and Thompson*, 2015; *Thoma et al.*, 2008; *Walker et al.*, 2013). Here we have posed the hypothesis that there is a large-scale advective pathway of heat from the open ocean to the ASE. To address this we diagnose the dynamical budgets in a model of the entire Southern Ocean that is consistent with available observations. We find a cross-shelf heat transport that is primarily geostrophic below the permanent pycnocline. The SOSE vorticity balance indicates that cross-shelf transport is driven by the local wind-stress curl, which is a dynamically relevant quantity that has previously been overlooked in favor of wind-stress (*Thoma et al.*, 2008; *Schmidtko et al.*, 2014; *Spence et al.*, 2014). The large-scale wind-stress curl forcing that we have identified is not the only mechanism at play. Future work must diagnose the relative importance of this large-scale pathway to the other mechanisms. Furthermore, the interplay of the dynamics at different scales needs to be addressed, including how the system responds to extreme or sustained wind changes.

While no study has explicitly examined vorticity dynamics driven by wind-stress curl in this region, the importance has been alluded to in other studies (e.g. *Dutrieux et al.*, 2014; *Thoma et al.*, 2008; *Wåhlin et al.*, 2013), supporting our hypothesis. *Thoma et al.* (2008) find that temporal variability of cross-shelf CDW transport is related to wind forcing over the shelf break. Though vorticity constraints are not identified within their proposed possible transport mechanisms, the evidence for such a pathway presented here is not inconsistent with the model results of *Thoma et al.* (2008). During their observational period, *Dutrieux et al.* (2014) found decreased glacial melt rates due to a depression of the thermocline forced by a weakened wind-stress curl over the shelf break. Additionally, the pseudo wind-stress correlation maps calculated by *Wåhlin et al.* (2013), exhibit a spatial structure characteristic of a system controlled by wind-stress curl, with correlations to the zonal wind that are positive to the south and negative to the north and correlations to the meridional wind that are positive to the east and negative to the west.

The realism of the reanalysis winds in this topographically complex region has only been validated by the few intermittent mean sea-level pressure measurements available in the near-by Bellingshausen Sea (*Bracegirdle*, 2012). Further verification with long-term in situ wind measurements in the Amundsen Sea would be useful. Westerly winds over the Amundsen Sea have been shown to correlate strongly with the El Niño Southern Oscillation (ENSO) (Niño 3.4) during spring, and to a lesser extent, with the Southern Annular Mode (SAM) during the summer on decadal time-scales (*Bracegirdle*, 2012; *Steig et al.*, 2012), while on multidecadal scales, the North Atlantic Oscillation (NAO) is the more important driver of atmospheric variability in the Amundsen Sea (*Li et al.*, 2014). Future work must now determine how the local wind-stress curl over the Amundsen Sea Embayment, and consequently the input of vorticity into the ocean system, is sensitive to changes in modes of large-scale atmospheric variability such as SAM, ENSO, and the NAO.

1.9 Acknowledgements

This work was supported by the National Science Foundation (NSF) Office of Polar Programs (grant ANT0961218), NSF Division of Ocean Sciences (grant OCE-1234473), NSF Scripps Institution of Oceanography Research Experience for Undergraduates (grant 1062305), and the National Oceanic and Atmospheric Administration (grant NA10OAR4310139). Computational resources for the SOSE were provided by NSF XSEDE resource grant OCE130007. The SOSE solution for the years 2005–2010, denoted iteration 100, is available from sose.ucsd.edu. The observations used for model validation are available from the NOAA National Ocean Data Center (http://www.nodc.noaa.gov/). The authors would like to thank Anna Wåhlin, as well as an additional reviewer for their helpful comments and suggestions on an earlier submission of this manuscript.

Chapter 1, in full, is a reprint of the paper "An oceanic heat transport pathway to the Amundsen Sea Embayment" published in Journal of Geophysical Research: Oceans by A. R. Rodriguez, M. R. Mazloff, and S. T. Gille in 2016. The dissertation author was the primary investigator and author of this paper.

1.A Vorticity budget derivation

Ocean circulation generally follows contours of constant f/h, where f is the Coriolis parameter and h is the water column height. However, flow from the open ocean across the Amundsen Sea shelf decreases h and increases f, defying this general concept. This change in f/h necessitates either an increase in relative vorticity, which we do not find, or vorticity forcing through local time-mean wind-stress curl (*Sverdrup*, 1947).

The vorticity balance stands in contrast to the momentum balance, which provides a natural framework for evaluating the geostrophic currents that balance the pressure gradient term. The vorticity balance provides a means to evaluate deviations from the geostrophic balance that are associated with the curvature of the wind stress. In this context, we are primarily interested in the southward flow onto the ASE continental shelf, which is explicitly isolated in this equation. In the presence of strong bottom flows or steep topography one must also consider the vorticity forcing induced from frictional boundary layers and pressure torques (*Hughes and de Cuevas*, 2001; *Spence et al.*, 2012).

The full SOSE vorticity budget is:

$$\zeta_t + \nabla \cdot (f\mathbf{u}) + \nabla \times (\mathbf{u} \cdot \nabla \mathbf{u}) = \nabla \times \left(\frac{\tau}{\rho} + \mathbf{V} \right), \tag{1.A.1}$$

where $\mathbf{u}$ is the horizontal velocity vector, τ is wind-stress, and $\mathbf{V}$ is the parameterized viscous term. Utilizing the nondivergent flow constraint ($\nabla \cdot \mathbf{u} = 0$), allows isolation of the meridional flow in the planetary advection term:

$$\nabla \cdot (f\mathbf{u}) = (fu)_x - (-fv)_y = -fw_z + \beta v, \tag{1.A.2}$$

where $\beta = f_y$. Due to the model discretization on a spherical grid, the pressure term does not vanish. In consistency with the model pressure solver formulation, we have added this contribution to the divergence term, and thus, it appears as a stretching term, $-fw_z$, in the vorticity budget.

Substituting 1.A.2 into 1.A.1 and rearranging we find the following vorticity balance

$$\underbrace{\zeta_t}_{\text{tendency}} + \underbrace{\beta v}_{\text{mean transport}} - \underbrace{\nabla \times \frac{\tau}{\rho}}_{\text{wind forcing}} - \underbrace{fw_z}_{\text{stretching}} + \underbrace{\nabla \times (\mathbf{u} \cdot \nabla \mathbf{u})}_{\text{advection}} - \underbrace{\nabla \times (\mathbf{V})}_{\text{viscosity}} = 0. \tag{1.A.3}$$

Chapter 2

Impacts of nearshore wave-current interaction on transport and mixing of small-scale buoyant plumes

2.1 Abstract

Small-scale buoyant outflows have the potential to impact beach contamination, nutrient exchange, productivity, larval recruitment, and carbon chemistry in the nearshore region where surface gravity waves influence momentum and energy transport. This study aims to understand the dynamics leading to the fate and structure of an idealized small-scale outflow in the presence of surface waves using a fully coupled 3-D hydrodynamic and spectral wave model. Wave-current interactions significantly alter plume structure when compared to hydrodynamics-only simulations. Wave dissipation injected into the water column as a flux of turbulent kinetic energy at the sea surface mixes the plume in the surf zone, while wave-driven velocities reduce offshore plume propagation and enhance alongshore spreading. A series of simulations varying

flow rate and offshore wave height indicate a log linear relationship between the surf zone volume-integrated freshwater fraction and the ratio of wave to outflow momentum fluxes.

2.2 Introduction

The chemistry and biology of coastal waters are strongly altered by terrestrially derived nutrients and contaminants transported to the nearshore region by estuarine outflows and storm water runoff (*Howard et al.*, 2014). These outflows, or plumes, are typically fresher than the ambient ocean and laden with constituents of the urban and agricultural landscape from which they are derived (*Walters et al.*, 2011). Consideration of the underlying physical mechanisms that affect plume structure, transport, and mixing in the coastal ocean is necessary to adequately understand beach contamination (*Grant et al.*, 2005; *Reeves et al.*, 2004), nutrient exchange (*Howard et al.*, 2014), productivity (*Anderson et al.*, 2002), larval recruitment (*Grimes and Kingsford*, 1996), and acidification (*Salisbury et al.*, 2008).

Garvine (1995) classified buoyant coastal outflows into two categories based on the Kelvin number, $K = \frac{W}{R_d}$ (*Wiseman and Garvine*, 1995), which compares the width of the outflow region, W, to the baroclinic Rossby radius of deformation, $R_d = \frac{\sqrt{g'h}}{f}$, where $g' = g\frac{\Delta\rho}{\rho_0}$ and h are the reduced gravity and depth at the estuary mouth, and f is the local Coriolis frequency. When $K \gg 1$, the outflow is considered to be large-scale based on location, geometry, and outflow buoyancy. The predominant focus of many dynamical investigations has been on large K plumes (e.g., *Akan et al.*, 2017; *Fong and Geyer*, 2001; *Gerbi et al.*, 2013; *Lentz*, 2004; *Moffat and Lentz*, 2012). It is also worth noting that these studies examined plume dynamics under large discharge conditions ($O(10^{-3})$ m^3 s^{-1} or larger), which is typical of many large-scale systems.

The distinction between large and small-scales in this study is based on both K and volumetric flow rate, Q. Relatively few dynamical studies have been done on small-scale plumes ($K \ll 1$ and small Q). Yet, examples of small-scale outflows, such as those emanating from narrow estuary mouths, creeks, or engineered structures are abundant along modern coastlines (Figure 2.1a) and are often accompanied by much smaller Q than their large scale counterparts (e.g., *Lahet and Stramski*, 2010; *Mazzini et al.*, 2014; *Nezlin et al.*, 2005; *Romero et al.*, 2016; *Warrick and Fong*, 2004; *Warrick et al.*, 2007).

Plume transport and structure can be described by the dominant dynamical balances (*Horner-Devine et al.*, 2015). In the source region, freshwater discharge reaches the bed until the flow becomes supercritical and the plume lifts off due to horizontal (*Armi and Farmer*, 1986) or vertical (*Farmer and Armi*, 1986) flow expansion. Once the plume detaches from the bed it behaves as a buoyant jet (*Jones et al.*, 2007) with a dominant balance between the barotropic and baroclinic pressure gradients, turbulent interfacial stress, and flow acceleration. If $K \ll 1$, the effects of Earth's rotation can be neglected, and the plume is expected to spread radially in the nearshore region (*Garvine*, 1995; *Horner-Devine et al.*, 2015).

While the dynamical regimes of buoyant outflows are fairly well understood under a variety of conditions, their superposition upon surf zone to inner-shelf circulation has yet to be examined in detail. Surface gravity waves greatly impact inner-shelf (*Lentz and Fewings*, 2012) and surf zone (*Thornton and Guza*, 1986) circulation and may strongly influence the fate of buoyant coastal discharges. *Gerbi et al.* (2013) parameterized wind wave breaking turbulence in a hydrodynamic model and found that the structure and offshore propagation of a large scale plume were altered, but the study did not resolve the surf zone or the inner shelf and did not include wave-current interactions. Expanding upon this work by examining wave-current interactions, *Rong et al.* (2014) found that 3-D wave forces and surface mixing reduced surface salinity of the Mississippi-Atchafalaya river plume ($K \gg 1$). Recently, *Akan et al.* (2017) investigated wave impacts on the Columbia river plume ($K \gg 1$) and identified increased wave heights near the river mouth and at the expanding plume edge, accompanied by an overall plume movement in the down-wave direction. However, the surf zone and the inner shelf were not resolved in these studies either. Realistic simulations by *Delpey et al.* (2014) and *Johnson et al.* (2013) indicate that waves strongly impact specific small-scale outflows but have little discussion of the dynamics leading to these results. Thus, a mechanistic study that can be used to draw conclusions about a range of outflow and wave conditions for small-scale plumes is desired.

Studies investigating the influence of surface waves on lock-exchange gravity currents reveal that frontal propagation is altered by wave-driven Stokes drift, and mixing is enhanced due to wave orbital motion (*Stancanelli et al.*, 2018; *Viviano et al.*, 2018). While the gravity current problem is informative to environmental buoyancy driven flows, it lacks outflow momentum and a dissipative surf zone which are included at realistic geophysical scales here.

These results describe the structure and dynamics of an idealized small-scale buoyant outflow into a surf zone and inner shelf subject to normally incident waves in the absence of additional forcing mechanisms to isolate wave impacts. Using a fully coupled ocean and wave modeling system, detailed understanding of the dynamics is gained through analysis of the 3-D flow and salinity fields, while contextualization is provided through variation of the relevant parameter space, which is presented as a freshwater index of plume structure plotted as a function of a nondimensional wave/plume momentum scaling. The model framework and setup is outlined in section 2.3. In section 2.4 model results with and without wave-current coupling are presented to highlight the differences in the dynamics and resultant overall nearshore plume structure. Simulations varying Q and significant wave height, H_s, model validity and limitations, and implications for these findings are discussed in section 2.5. A summary is given in section 2.6.

2.3 Methods

A series of numerical simulations coupling a wave-averaged spectral wave model, Simulating Waves in the Nearshore (SWAN; *Booij et al.*, 1999), to a free surface, hydrostatic, primitive equation model, the Regional Ocean Modeling System (ROMS; *Shchepetkin and McWilliams*, 2005), within the Coupled Ocean Atmosphere Wave Sediment Transport (COAWST) framework (*Warner et al.*, 2010), are conducted. ROMS and SWAN have both been used to study a variety of coastal environments with great success, and COAWST has been validated in several studies including investigations of wave-current interaction in the surf zone (*Kumar et al.*, 2012) and a tidal inlet (*Olabarrieta et al.*, 2014).

The relevant physical processes included in ROMS-SWAN coupling are wave shoaling, wave refraction due to both bathymetry and mean currents, wave energy loss due to bottom friction, and depth-limited wave breaking. A key aspect of the ROMS-SWAN coupling in COAWST is that the depth varying flow field is decomposed into Eulerian and wave-induced velocities. The following sections discuss Lagrangian mean velocity, which is the sum of the quasi-Eulerian mean velocities and Stokes drift (*Jenkins*, 1989). The coupled momentum equations account for the vortex force and the Bernoulli head, which are conservative wave forces, as well as depth-induced wave breaking, which is a nonconservative wave force. In addition to providing a depth-varying force in the momentum equations, 25% of wave energy dissipation is used for the surface boundary condition of turbulent kinetic energy (TKE; *Craig and Banner*, 1994; *Feddersen and Trowbridge*, 2005) in the generic length scale turbulence closure scheme (*Umlauf and Burchard*, 2003) as implemented in *Warner et al.* (2005), which includes buoyant and shear production of TKE. Findings presented here are not sensitive to changes in the percentage of wave dissipation as surface TKE flux for a range of values measured in the surf zone (10-15%; *Feddersen*, 2012; *Zippel and Thomson*, 2015) and used in previous numerical modeling studies (25%; *Feddersen and Trowbridge*, 2005; *Kumar et al.*, 2012) (see Appendix 2.B).

The idealized model domain is formulated based on analysis of average channel and mouth widths of 60 bays, lagoons, and estuaries in the Southern California Bight region. Key features of these systems include bathymetric sills near the mouth and shallow beach slopes. The bathymetry upcoast, downcoast, and offshore of the sill is alongshore uniform following a typical beach profile (*Dean*, 1991). Thus, our model is intended to represent a variety of small-scale plume regions with episodic discharge events of low to moderate Q flowing into a surf zone generated over a broad shelf, such as those found along the entire U.S. West Coast and elsewhere (e.g., *Mazzini et al.*, 2014). The model domain is 12×10 km with with a maximum offshore depth of 45 m and a minimum depth of 0.32 m. The horizontal rectangular grid discretization is stretched in the cross-shore direction from 100 m at the western boundary, to 15 m within the channel while the alongshore resolution is 15 m everywhere (see blue tick marks in Figure 2.1e). There are 20 terrain following vertical levels with enhanced surface resolution (light gray lines in Figure 2.2m). Thus, the model setup utilized in this study resolves wave-current interactions and plume dynamics within the surf zone and the surf zone to inner-shelf transition region.

The quiescent ocean state is initialized with a constant temperature and salinity representative of southern California shelf waters, $T_0 = 15°\text{C}$ and $S_0 = 33.35$ PSU, everywhere in the basin and channel. The ROMS-SWAN coupled simulations are forced via wave spectra that include spectral modification induced by wave shoaling imposed

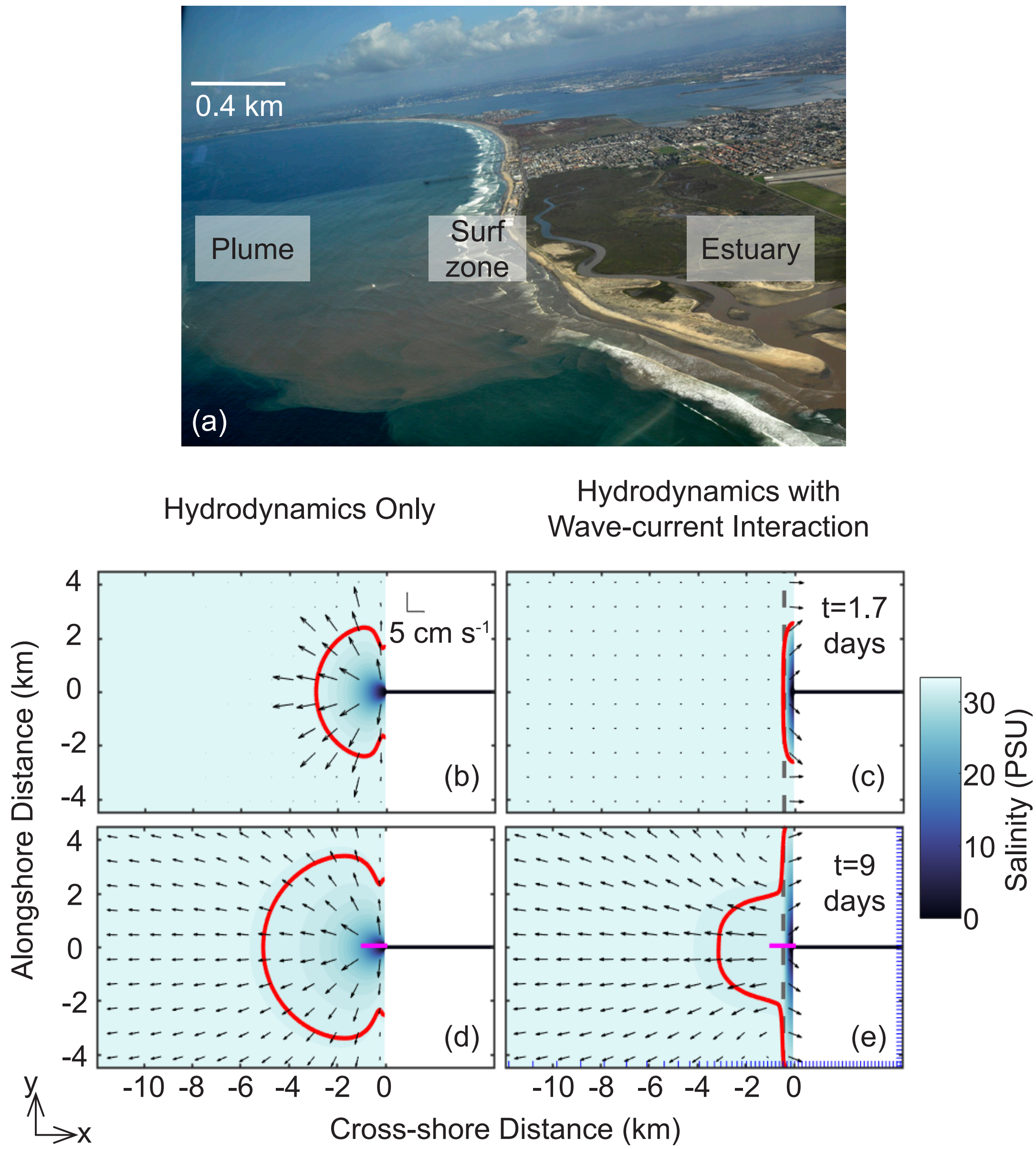

Figure 2.1: Aerial image of a contaminated small-scale plume in southern California and the idealized model results. (a) Tijuana River plume (photo credited to Wildcoast). (b–e) Surface salinity (PSU) and surface current vectors (cm s^{-1}) throughout the domain after 1.7 (b, c) and 9 (d, e) days of Q=20 m^3 s^{-1}. The plume edge (red) is taken to be the 97th percentile of the salinity range. (b) and (d) show results for the hydrodynamics-only solution, while (c) and (e) show coupled model results which simulate wave-current interactions with $H_s = 1$ m. Blue tick marks on (e) indicate every tenth numerical grid cell. Magenta lines in panels (d) and (e) represent the location of the cross sections in Figure 2.2.

along the offshore, northern, and southern domain edges. Spectra are normally incident with a directional spread of 10°, a peak period of 10 s and H_s of 0.5, 0.75, or 1 m, conditions typical of southern California swell. Freshwater flow is introduced at the eastern boundary along the channel edge after 1 day of wave-current interaction spin-up. Time, t, is referenced to the start of river flow, that is, $Q(-1 \text{ day} < t < 0) = 0$ while $H_s(-1 \text{ day} < t < 0) > 0$. Flow rates are based on low-inflow estuary hydrographs, which are dominated by episodic discharge events. The values simulated here range from 5 to 100 $\text{m}^3\ \text{s}^{-1}$. The prescribed outflow is constant for 9 days, allowing the circulation to reach a quasi-steady state. Though the duration of small-scale outflows is often less than 1 week, the steady state analysis presented in section 2.4 provides a dynamical understanding of wave-current interaction plume impacts that have not previously been identified. The impact of unsteady conditions is elaborated upon in the discussion.

2.4 Results

2.4.1 Plume Structure and Transport

Figures 2.1 and 2.2 compare a simulated outflow of $Q = 20$ $\text{m}^3\ \text{s}^{-1}$ with and without interaction with $H_s = 1$ m waves at the offshore boundary. Surface salinity and Lagrangian velocity vectors at sequential times for the hydrodynamics-only simulation (Figures 2.1b and 2.1d) indicate that in the absence of wave-current interaction, the buoyant outflow spreads radially from the channel mouth, consistent with classical plume theory, with the exception of side lobes located very near the coast. However, comparison of the leading plume edge at the surface, defined as 97% of the salinity range (red lines in Figures 2.1b–2.1e), indicates that this structure is greatly altered by wave-current interactions. In the presence of wave-current interactions, freshwater travels through the channel and 2 km alongshore from the mouth over 1.7 days, after which the plume lifts off of the seabed and the flow ejects freshwater beyond the surf zone edge, defined as the cross-shore location of maximum H_s (gray dashed line in Figure 2.1c and 2.1e). While the leading edge of the classical plume front, delineated by 97% of S_0 (red contour in Figures 2.1 and 2.2), has spread 2.5 km offshore by $t = 1.7$ days (Figure 2.1b), the wave-impacted plume edge does not extend beyond the surf zone (Figure 2.1c) at this time. Upon liftoff and surf zone ejection, the plume spreads most strongly in the cross-shore direction, and also alongshore (Figure 2.1e) and remains surface intensified (Figure 2.2j). While the magnitude of the horizontal salinity gradient tapers offshore radially in the classical plume, there is a strong cross-shore salinity front between the surf zone and inner shelf with waves.

Onshore-directed surface velocity arrows within the surf zone (Figure 2.1c and 2.1e) are a manifestation of the surface intensified onshore-directed wave breaking body force (momentum budget analysis in Appendix 2.A), which counteracts the offshore barotropic and baroclinic pressure gradients, inhibiting cross-shore plume spreading. The slight northward and southward flow angle within the surf zone is the result of alongshore pressure gradients and advection directed away from the mouth, driving the plume along the coast. By day 9 of the coupled simulation, surface velocities reach several centimeters per second throughout the domain, yet most of the freshwater is shoreward of $x = -4$ km (Figure 2.1e). This stark contrast in structure and transport between the two cases, as well as the time evolution to the quasi-steady state, has strong implications for realistic nearshore plume influence.

2.4.2 Wave-Current Interaction: Currents and Mixing

Compared to the hydrodynamics-only simulation, cross-shore frontal propagation in the presence of wave-current interaction is suppressed due to the onshore-directed nonconservative wave breaking force and increased surf zone mixing. Consequently, alongshore plume spreading is enhanced through the conservation of mass, which requires nondivergence of the flow field. Further understanding of the differences in surface structure is gained from Figure 2.2, which shows cross sections near the plume center without and with wave-current coupling at $t = 9$ days (see magenta line in Figures 2.1d and 2.1e). The presence of waves induces a sea surface setdown and setup in the cross-shore direction which shifts the sea surface height, η (blue line in Figure 2.2b), to a higher value at the channel mouth, where H_s (black line in Figure 2.2b) decreases to a minimum value and the slope, $\frac{\partial \eta}{\partial x}$, decreases to match that of the classical plume. In both simulations, η increases in the positive x direction for $x > 0$ km with similar values of $\frac{\partial \eta}{\partial x}$, indicating that the freshwater surface expression is consistent between the two simulations.

Lateral gradients in η and density traditionally dominate plume momentum balances, but in the presence of wave-current interaction, flow structure deviates from the classical case. The cross-shore flow structure of the hydrodynamics-only simulation is similar to a two-layer estuarine exchange flow (Figure 2.2c), with strong river flow at the surface offshore of the sill and an induced weaker, onshore flow at depth. Vertical velocities (Figure 2.2g) are intensified near the sill, where positive vertical flow is associated with plume liftoff. Cross-shore and vertical flow structure is much more complex with wave-current coupling (Figures 2.2d and 2.2j). The Lagrangian mean flow consists of wave-driven Stokes drift and the quasi-Eulerian mean velocity (i.e., anti-Stokes flow and the river flow). The resultant structure shows distinct flow regions in the channel, surf zone (region between the sill and the vertical gray dashed line in Figure 2.2), and inner shelf. Wave influence within the channel is negligible and the flow is indistinguishable from the hydrodynamics-only simulation (Figure 2.2d). Just offshore of the sill (~ 0 km $< x < -0.2$ km), velocities are directed offshore and downward at the bed (Figures 2.2d and 2.2n respectively). In the surf zone, onshore-directed wave-driven velocities (i.e.,

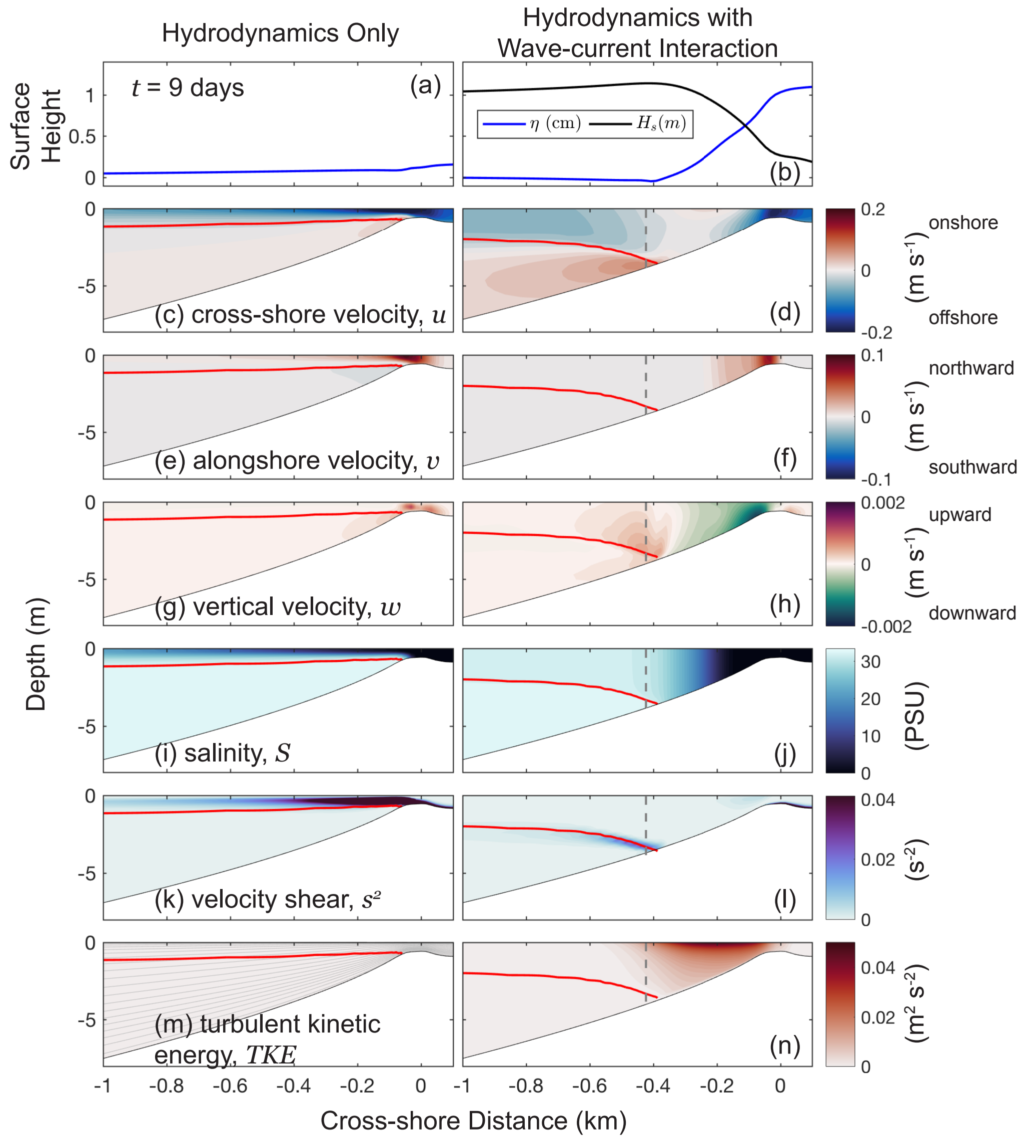

Figure 2.2: Cross sections through the plume after 9 days of Q=20 m^3 s^{-1} outflow located at y=0.045 km within the surf zone to inner-shelf transition region (see Figure 2.1 magenta line) showing: (a, b) sea surface height (cm) and significant wave height (m), (c, d) cross-shore velocity (m s^{-1}), (e, f) alongshore velocity (m s^{-1}), (g, h) vertical velocity (m s^{-1}), (i, j) salinity (PSU), (k, l) velocity shear squared (s^{-2}), and (m, n) turbulent kinetic energy (m^2 s^{-2}). The thick, vertical dashed gray line indicates the offshore surf zone edge determined by the maximum H_s location. The red line indicates the plume edge taken to be the 97th percentile of the salinity range as in Figure 2.1. Light gray lines in panel (m) show the numerical grid vertical discretization. TKE = turbulent kinetic energy; PSU = practical salinity unit.

Stokes drift), which are strongest at the surface and decrease with depth, dominate river outflow velocities, resulting in slightly positive surface velocities, which decay to near zero with depth in the surf zone region between -0.4 km $< x < -0.2$ km (Figure 2.2d). Additionally, wave breaking induces strong downward velocities over and offshore of the sill that extend through the water column, suppressing liftoff at the sill and shifting strong positive vertical velocities associated with plume liftoff to the surf zone edge (Figure 2.2h). Offshore of liftoff, outflow velocities dominate the Stokes drift, and the velocity structure relaxes to the typical estuarine exchange flow. Alongshore velocities are strongest in the surf zone (Figure 2.2f) and are symmetric about the plume center (Figure 2.1e).

The drastic differences in horizontal plume structure depicted in Figure 2.1 are largely due to surf zone circulation. However, vertical salinity structure (Figures 2.2i and 2.2j) indicates that mixing also plays an important role in the horizontal distribution of surface salinity (Figure 2.1). In the absence of wave-current interaction, the region offshore of the sill is strongly stratified (Figure 2.2i) due to the plume surface intensification and a lack of mixing mechanisms beyond shear instability. The outflow momentum leads to high levels of shear, $s^2 = \left(\frac{\partial u}{\partial z}\right)^2 + \left(\frac{\partial v}{\partial z}\right)^2$, along the lower edge of the plume (Figures 2.2k and 2.2l). Both simulations exhibit high shear within the channel near the bed, and in the vicinity of plume liftoff. In the absence of wave-current interaction, high values of shear are continuous from the channel through the plume core, tapering offshore. However, with waves, shear is minimized in the surf zone until the liftoff point (Figure 2.2l). This shear is much less than in the hydrodynamics-only simulation, indicating that the outflow momentum has been significantly reduced in the transition from the channel to the inner shelf in the presence of waves. Additionally, isohalines are vertically oriented within the surf zone (Figure 2.2j), indicating the presence of a strong mixing source. Wave breaking within the surf zone induces high vertical diffusivities, which act to homogenize the water column within the surf zone via TKE input from wave breaking dissipation (Figures 2.2m and 2.2n). This sets up a large cross-shore salinity gradient that extends through the water column until plume liftoff (Figure 2.2j). The resultant surface intensified flow is significantly saltier and deeper than the classical plume (Figure 2.2i). The flow structure and dynamics are similar at cross sections to the north and south of that shown in Figure 2.2.

2.5 Discussion

2.5.1 Riverine versus Wave Momentum Fluxes—Parameter Space Variation

It has been shown that wave-current interaction for $H_s = 1$ m waves significantly impacts the transport and distribution of freshwater emanating from a 20 m^3 s^{-1} outflow. However, variation of the relevant flow and wave parameters will alter the described surf zone to inner-shelf freshwater distribution. While Q dictates plume momentum and freshwater input, H_s determines wave-driven current magnitudes, wave energy flux/dissipation, and the surf zone width, L_{sz}, which in turn impact circulation and mixing. Thus, simulations of low-inflow estuary flow rates (5 m^3 s^{-1} $\leq Q \leq$ 100 m^3 s^{-1}) combined with typical offshore wave heights (0.5 m $\leq H_s \leq$ 1 m) have been analyzed in terms of the 3-D freshwater distributions and momentum fluxes. The relative role of wave period, T_p, versus plume surf zone crossing time can be described by the ratio $\tau = T_p/(\frac{L_{sz}}{U})$, where U is the outflow velocity. For $T_p = 13$ s, $H_s = 1$ m, τ is $O(10^{-3})$ for $Q \leq 40$ m^3 s^{-1} and $O(10^{-2})$ for $Q > 40$ m^3 s^{-1}, indicating that the plume advective time scale is much longer than the peak period of the waves at the simulated flow rates. Thus, the parameter space variation discussed below considers only changes in Q and

H_s for fixed $T_p = 10$ s and normally incident wave angle.

The freshwater fraction, defined as

$$\delta S = \frac{S_0 - S}{S_0} \tag{2.5.1}$$

is a unitless quantity which measures how fresh or saline a water mass is relative to the open ocean (*Hetland*, 2005). Completely freshwater results in $\delta S = 1$, while $\delta S = 0$ corresponds to the background ocean salinity. Red contours distinguishing the plume edge in Figures 2.1 and 2.2 are equivalent to $\delta S = 0.03$.

Volume integrals of the plume freshwater fraction within the surf zone and inner shelf are calculated separately to quantify the partition of freshwater between the two regions. The freshwater volume is defined as

$$V_i = \iiint\limits_{\delta S > 0.03} \delta S \, \mathrm{d}V_i \tag{2.5.2}$$

where the integral is calculated over the plume volume ($\delta S > 0.03$) in the surf zone, V_{sz}, and inner shelf, V_{is}, separately after 9 days of simulated outflow. The surf zone freshwater volume as a fraction of the total volume-integrated freshwater, $\frac{V_{\mathrm{sz}}}{V_{\mathrm{sz}}+V_{\mathrm{is}}}$, provides an index for plume structure, indicating the relative amount of freshwater that is trapped along the coast. As $\frac{V_{\mathrm{sz}}}{V_{\mathrm{sz}}+V_{\mathrm{is}}}$ approaches 1, all freshwater is trapped within the surf zone.

As a means of comparing the contributions of outflow momentum and wave-driven momentum, a nondimensional scaling based on the associated cross-shore momentum contributions is formed. The cross-shore depth-averaged momentum equation, assuming steady state, hydrostatic flow, small sea level variations compared to the water depth, and neglecting the Coriolis force is

$$\frac{1}{h}\frac{\partial}{\partial x}\int_{-h}^{0} u^2 \mathrm{d}z + \frac{1}{h}\frac{\partial}{\partial y}\int_{-h}^{0} uv \mathrm{d}z = -\frac{1}{\rho_0}\frac{\partial P}{\partial x} - \frac{\tau^{bx}}{\rho_0 h} - \frac{1}{\rho_0 h}\frac{\partial S_{xx}}{\partial x} \tag{2.5.3}$$

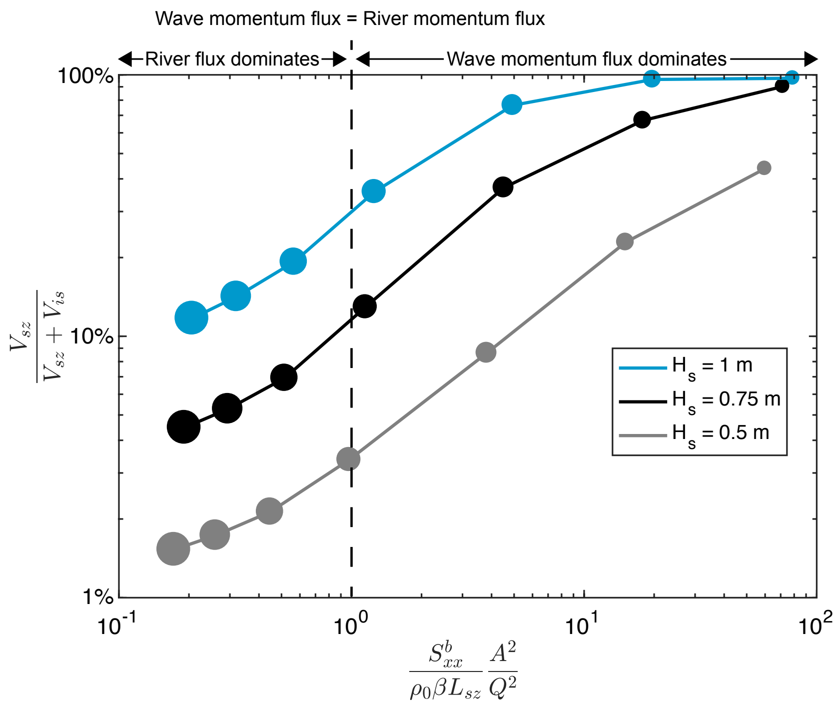

Figure 2.3: Percentage of freshwater volume within the surf zone as a function of the ratio of the wave and river momentum fluxes for simulations varying both Q and H_s. Results are plotted on log scales to display the range of values. Circle size indicates flow rate, which ranges from 100 m^3 s^{-1} (largest) to 5 m^3 s^{-1} (smallest circles).

where u and v are the cross-shelf (x) and alongshelf (y) velocity components, h is the water depth, $\rho_0 = 1,025$ kg m^{-3} is the background density, $\frac{\partial P}{\partial x}$ is the depth-averaged cross-shore pressure gradient, τ^{bx} is the bottom stress, and S_{xx} is the wave radiation stress. A scaling of the ratio of the radiation stress gradient term and the first advective term is given by

$$\frac{\frac{1}{\rho_0 h}\frac{\partial S_{xx}}{\partial x}}{\frac{1}{h}\frac{\partial}{\partial x}\int_{-h}^{0} u^2 \mathrm{d}z} \sim \frac{\frac{1}{\rho_0 \hat{h}} S_{xx}}{U^2} \tag{2.5.4}$$

where $\hat{h}$ is the vertical length scale associated with the water depth and U is the velocity scaling. The numerator is maximum at the offshore surf zone edge just before H_s decreases due to depth limited wave breaking. The denominator is maximum within the channel before alongshore momentum becomes important. Evaluating the numerator at the surf zone edge and the denominator at the mouth,

$$\frac{\frac{1}{\rho_0 \hat{h}_b} S_{xx}^b}{U^2} = \frac{S_{xx}^b}{\rho_0 \beta L_{sz}} \frac{A^2}{Q^2} \tag{2.5.5}$$

where S_{xx}^b and $\hat{h}_b = \beta L_{sz}$ are the radiation stress and the water depth at the breaking point respectively, assuming a linear beach slope (β), and A is the channel mouth cross sectional area. This quantity provides a comparison of the maximum wave and outflow momentum fluxes to help determine under what conditions surface gravity wave forcing significantly impacts plume structure. Further manipulation of this nondimensional momentum flux comparison reveals that the relevant quantity is also a comparison of wave dissipation to outflow kinetic energy. Specifically, assuming narrow-banded frequency and direction in shallow water and neglecting alongshore outflow velocity at the mouth, the quantity becomes $\frac{D}{8\beta c_g KE}$, where D is the wave dissipation across the surf zone, c_g is the group speed, and KE is the kinetic energy of the plume at the mouth. Written in terms of momentum, (2.5.5) can be easily estimated from relatively simple observations without a 3-D numerical model. For example, S_{xx} can be determined from offshore buoys, Q is often available from flow gauges, and A and β can be estimated from topography and bathymetry.

Figure 2.3 shows the surf zone freshwater volume proportion, $\frac{V_{\mathrm{sz}}}{V_{\mathrm{sz}}+V_{\mathrm{is}}}$, as a function of the nondimentional cross-shore flux comparisons for 21 different simulations: $Q = 5$, 10, 20, 40, 60, 80, and 100 m^3 s^{-1} and $H_s = 0.5$, 0.75, and 1 m. As Q increases, the amount of freshwater exiting the surf zone onto the inner shelf increases, and when plotted on a log-log axis, the relation is nearly linear. When the onshore-directed wave momentum flux is approximately equal to the offshore-directed river momentum flux ($\frac{S_{xx}^b}{\rho_0 \beta L_{sz}} \frac{A^2}{Q^2} = 1$, which for these simulations occurs for $40 \leq Q \leq 60$), the surf zone trapped freshwater ranges from 3% to 30% of the total freshwater content. At lower Q and $H_s > 0.5$ m, the curves asymptote to 1, indicating that nearly 100% of the freshwater is retained in the surf zone and negligible amounts are offshore. Figure 2.3 provides ranges of H_s and Q for which wave-current interactions are likely important.

2.5.2 Model Validity and Limitations

The results presented here provide evidence that, at low flow rates, small-scale buoyant plume dynamics and structure are strongly altered in the presence of surface gravity waves, largely due to the presence of a surf zone. Despite their prevalence and impact on coastal ecology and societies, relatively few studies have examined plumes of these scales thus far (*Lahet and Stramski*, 2010; *Nezlin et al.*, 2005; *Romero et al.*, 2016; *Warrick et al.*, 2007; *Warrick and Fong*, 2004). Additionally, the capacity to model the surf zone in a 3-D numerical framework that includes stratification has only recently been developed (*Kirby*, 2017; *Kumar and Feddersen*, 2017a; *Kumar et al.*, 2012). As a first step in understanding the complex dynamics of wave-current interaction with a strongly stratified outflow, a simplified, idealized model setup was used. However, more work should be done in order to understand how the findings of this study may change under various conditions. For example, a logical next step would be to vary the incident wave angle. This will drive an alongshore current (*Longuet-Higgins*, 1970) which can be $O(10 \text{ cm s}^{-1})$. This may significantly augment alongshore transport, resulting in asymmetrical outflow spreading in the direction of the wave-driven current (*Wong et al.*, 2013). Similarly, an angled outflow channel would likely result in asymmetrical alongshore spreading. Further investigations should also consider the role of tides, which can modulate flow rate (*Garvine*, 1999; *Pritchard and Huntley*, 2006) and mixing (*MacCready and Geyer*, 2010; *Geyer and MacCready*, 2014), as well as alter the relevant wave parameters (*Longuet-Higgins and Stewart*, 1960). Addition of the Coriolis force, which can affect plume structure and mixing (*Cole and Hetland*, 2015) as well as introduce additional wave terms in the momentum equations (i.e., the Stokes-Coriolis term) (*Lentz and Fewings*, 2012), should also be considered. Moreover, synoptic and diurnal winds also have the potential to alter plume structure through wind-wave-current interaction and direct plume forcing as a surface stress.

2.5.3 Implications for Terrestrial-Derived Constituents

Despite the simplified model setup, the key finding that wave momentum fluxes and mixing confine freshwater to the coastline is likely robust and especially pertinent for realistic, ephemeral outflows which tend to be nearshore sources of contaminants (*Reeves et al.*, 2004) and nutrients (*Anderson et al.*, 2002). The simulated outflow in the model presented here lasted for over a week to permit a steady state dynamics analysis. However, a steady state may not actually be achieved by realistic small-scale outflows, many of which are transient. Given that the simulations presented here yield surf zone breakthrough times between several minutes and 1 week once the plume has exited the channel mouth, many small-scale transient plumes and their constituents may not break through the surf zone barrier, remaining confined to the coast, particularly at low Q and/or large H_s. Additional exchange mechanisms such as bathymetric (*Brown et al.*, 2015) or transient (*Hally-Rosendahl et al.*, 2015; *Kumar and Feddersen*, 2017b) rip currents would then be crucial to the export of plume water onto the inner shelf. Further investigation of nutrient and contaminant laden freshwater plume dynamics within the surf zone to inner shelf is a necessary step in understanding the interaction between eutrophication/contamination and nearshore circulation and ultimately preserving nearshore ecosystem stability (*Smith and Schindler*, 2009) and water quality.

2.6 Summary

This study analyzes the dynamics and structure of small-scale buoyant coastal outflows (small K and small Q) to the nearshore region in the presence of surface gravity wave forcing using a fully coupled 3-D hydrodynamic and spectral wave model. The simulated distribution of freshwater indicates that the plume is largely confined to the coast and spreads alongshore until it lifts off of the seabed. Wave dissipation injected into the water column as a flux of TKE at the sea surface mixes the plume in the surf zone leading to strong offshore horizontal density gradients. Simulations of low-inflow estuary flow rates combined with typical offshore wave heights result in a parameter space regime that indicates a log-linear relationship between the volume integrated freshwater fraction within the surf zone and the ratio of wave to river momentum fluxes. This nondimensional parameter, easily quantified through observations, could be used to a priori assess whether a plume may be impacted by waves, given the wave and flow conditions. Because the freshwater distribution can be thought of as a proxy for tracers such as pollution, nutrients, or other plume laden constituents, these results have strong implications for beach contamination among other concerns that frequently arise due to the presence of buoyant outflows in the nearshore region.

2.7 Acknowledgments

The authors would like to thank Falk Feddersen, Maitane Olabarrieta, and John Warner for useful conversations in the initial phases of model development, as well as 2 anonymous reviewers whos comments and suggestions greatly enhanced the clarity of this article. This material is based upon work supported by the NSF GRFP under grant DGE-1144086 (A. R. R.), as well as the Environment Blasker-Miah-Rose Grant for Climate Change Research through the San Diego Foundation, and is connected to NSF

OCE 1459389 (S. N. G.). N. K. acknowledges support from ONR (award N00014-17-1-2890). The authors would like to acknowledge high-performance computing support from Yellowstone (ark:/85065/d7wd3xhc) provided by NCAR's Computational and Information Systems Laboratory, sponsored by NSF and the COMPAS/ATLAS cluster maintained by Caroline Papadopoulos and Bruce Cornuelle. The model configuration files/output used in this manuscript are available upon request as described here: https://scripps.ucsd.edu/labs/sgiddings/research/coastal-ocean/smallplume- dispersion/.

Chapter 2, in part, is a reprint of the paper "Impacts of nearshore wave-current interaction on transport and mixing of small-scale buoyant plumes" published in Geophysical Research Letters by A. R. Rodriguez, S. N. Giddings, and N. Kumar in 2018. The dissertation author was the primary investigator and author of this paper.

2.A Coupled Momentum Balance

While the simplified momentum balance in Equation 2.5.3 provides a conceptual framework that has practical application, the full momentum formulation utilized in this study relies on the Vortex Force formalism (*Craik and Leibovich*, 1976; *Uchiyama et al.*, 2010), not the radiation stress tensor. There are significant advantages to this method, and as such, it has been widely adopted among nearshore modelling studies (e.g. *Olabarrieta et al.*, 2011; *Kumar et al.*, 2012, and papers thereafter). An overview of the methodology progression and the numerical implementation is outlined in *Kumar et al.* (2012), wherein wave forcing is separated into conservative and nonconservative contributions following *Uchiyama et al.* (2010). The conservative contributions have a known vertical distribution and consist of the gradients of a Bernoulli head (i.e. the pressure adjustment that accommodates incompressibility) and a vortex force, which is a function of Stokes drift and flow vorticity. The nonconservative contribution is acceleration induced by wave dissipation, and is modeled with an empirically-derived cosh distribution that is a function of water depth and wave height. In the present work, white-capping is not activated and no fraction of the wave dissipation is partitioned into roller generation. Thus, the acceleration due to wave breaking is given by Equation 33 in *Kumar et al.* (2012) with $\alpha^r = 0$.

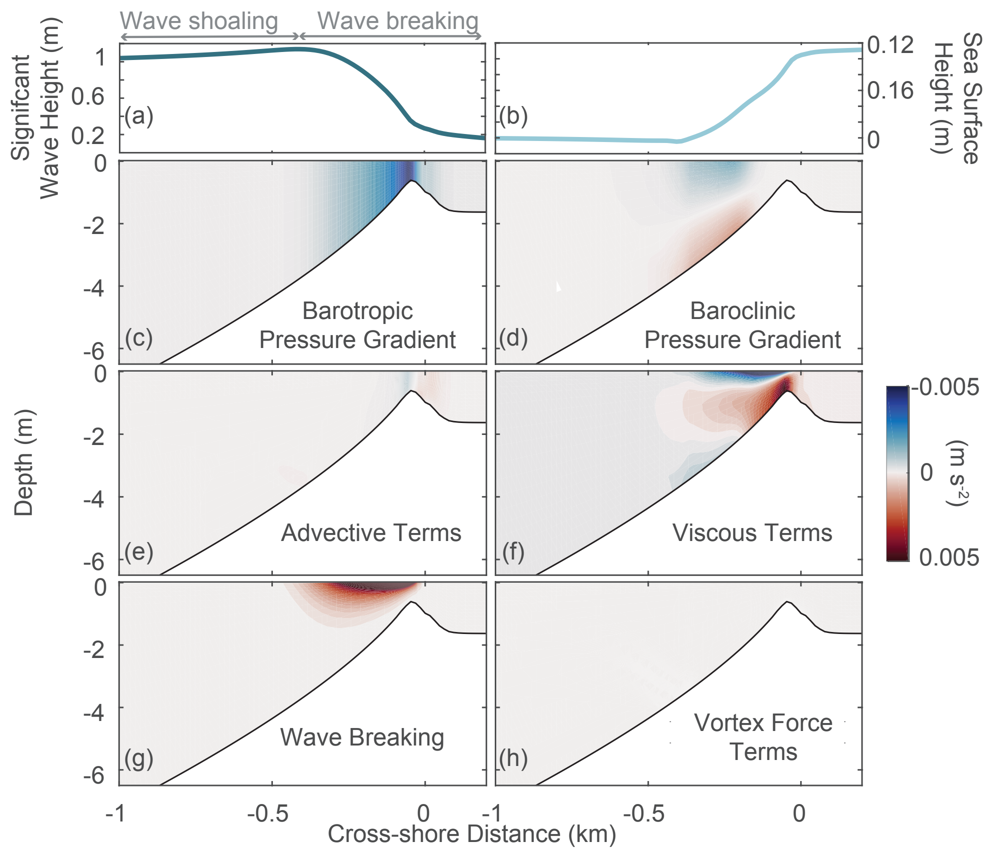

Figure 2.4: Results along the domain centerline from day 9 of a ROMS-SWAN coupled model run shown in Figures 2.1 and 2.2. (a) Significant wave height (m). (b) Quasi-static sea level (m). (c) - (h) Cross-shore momentum equation terms as labeled.

Figure 2.4 shows the coupled cross-shore momentum terms at the domain centerline. The baroclinic pressure gradient is given by the difference in the barotropic (i.e. depth averaged) pressure gradient from the full 3D pressure gradient. The barotropic pressure gradient contains the Eulerian sea level adjustment, the quasi-static sea level adjustment, the surface pressure boundary correction, and the Bernoulli head. Vortex force terms have been grouped in Figure 2.4h. To leading order, the combined effect of wave-induced pressure gradients and plume setup manifested in the barotropic pressure gradient is balanced by wave breaking induced acceleration at the surface, turbulent mixing at mid-water-column levels, and the baroclinic pressure gradient near the seabed within the surfzone. As mentioned in Section 2.4, wave-breaking acceleration in the surf zone plays a major role in offshore plume propagation reduction.

2.B TKE Surface Boundary Condition Tests

Sensitivity tests varying the percentage of wave dissipation provided as a surface boundary condition for turbulent mixing, c_ε, were conducted. Figure 2.5 is similar to Figure 2.2, but comparing test simulations that employ $c_\varepsilon = 5\%$ (left side of Figure 2.5) and $c_\varepsilon = 15\%$ (right side of Figure 2.5). These simulations have a river flow of $Q = 20$ m^3 s^{-1} and significant wave height, $H_s = 1$ m, and are thus directly comparable to the simulation discussed at length in this chapter (i.e. $c_\varepsilon = 25\%$). These values were chosen based on direct estimates of dissipation in the surf zone due to long wave breaking, which range from 9-15% of the total wave energy flux gradient (*Feddersen*, 2012; *Zippel and Thomson*, 2015). The main difference among the tested values is the cross-shore location of plume liftoff, which appears to be set by the location where the surface-enhanced TKE no longer penetrates to the seabed. The key findings of the chapter, enhanced surf zone mixing and alongshore spreading, are robust results that are not sensitive to c_ε within the range of values measured in field experiments (*Feddersen*, 2012; *Zippel and Thomson*, 2015) and used in previous modeling studies (*Feddersen and Trowbridge*, 2005; *Kumar et al.*, 2012).

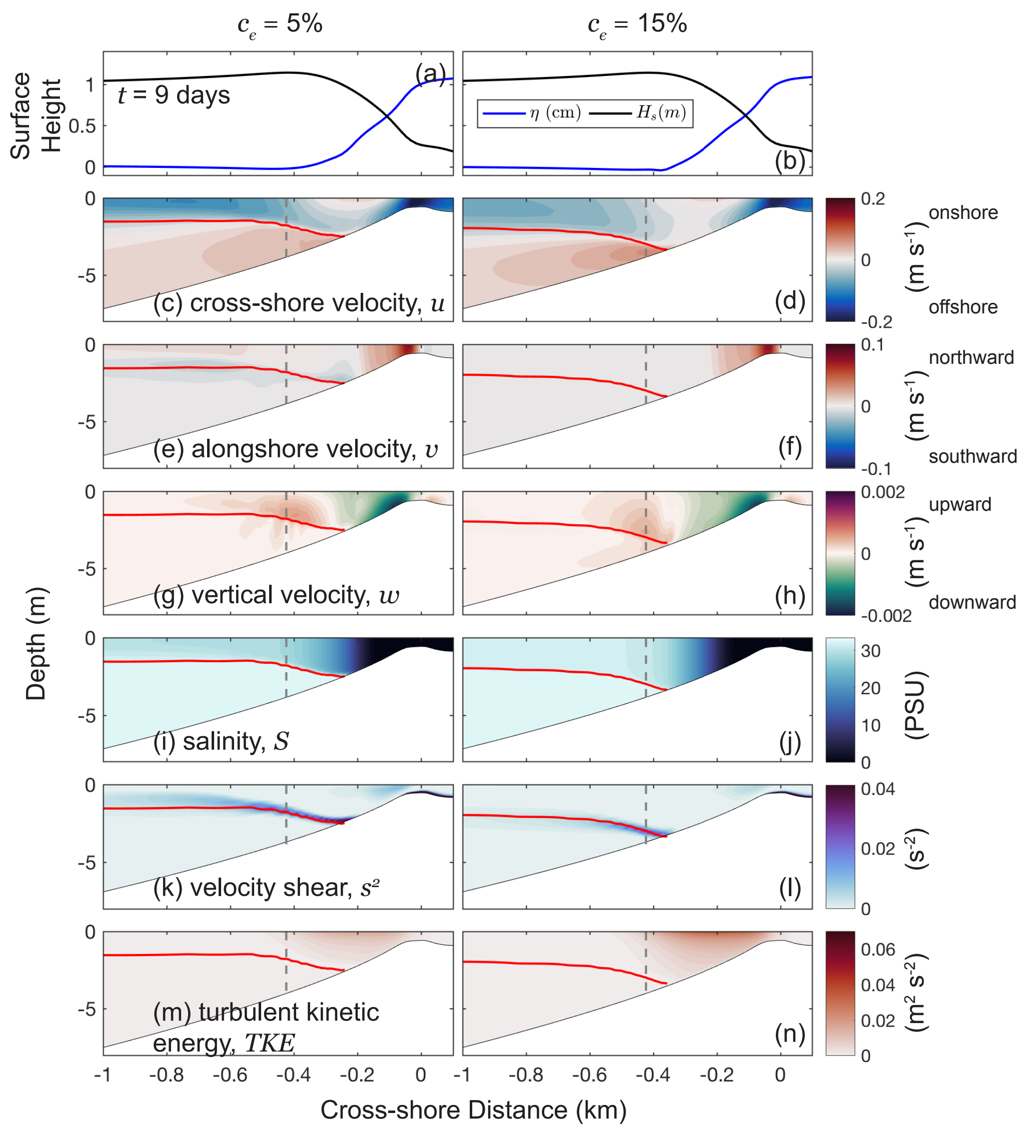

Figure 2.5: Comparison of a simulations with lower wave energy dissipation diffusion. left: c_ε=5% and right: c_ε=15%. The cross-section location ($y = 45$ m), time, and the panels shown are the same as in Figure 2.2.

Chapter 3

Lateral circulation in a low-inflow, seasonally hypersaline estuary

3.1 Abstract

Low inflow estuaries are ubiquitous among Mediterranean climate coastlines, but have been less well studied than systems with intense or regular freshwater input. An observational study was conducted to examine the interplay between seasonal variation in the longitudinal density gradients of a low inflow estuary in Southern California and the impacts on transverse circulation. As has been previously documented and confirmed to be the case during this experiment, negligible precipitation and river flow lead to net evaporation over the estuary, resulting in hypersaline conditions through the summer to fall months. Hypersalinity is accompanied by increased water temperatures during the peak summer months, maintaining density gradients in the traditional direction of a canonical freshwater estuary throughout the majority of the basin. As air temperatures cool into the fall season, shallow bay waters cool as well, reducing the overall longitudinal temperature gradient, and shifting the state of the estuary to a parameter

space that is more sensitive to the hypersaline conditions, thus facilitating inverse longitudinal gradients throughout the inner half of the bay. Full tidal cycle hydrographic and velocity surveys during spring tides in the lateral and longitudinal directions confirm the inversion of longitudinal baroclinic pressure gradients and altered lateral gradients, consistent with a hypothesized mechanism of differential advection during inverse conditions. The second mode empirical orthogonal function of moored current profilers reveals that there is also an inversion in the sign of the transverse circulation patterns, suggesting that the alteration of lateral baroclinic pressure gradients by differential advection may contribute to the lateral momentum balance. However, full tidal velocity does not support a complete inversion of the flow field, which is likely a result of alternative mechanisms dominating the balance. Results are discussed in the context of the important estuarine processes of longitudinal exchange, differential advection, and straining induced periodic stratification. Conjectures on the impact of climate change to circulation within this estuary based on the observations are also presented.

3.2 Introduction

Estuaries, here considered to be semi-enclosed basins bordered by the open ocean on one side and subject to along-estuary baroclinic pressure gradients, have long been recognized as a critical component to coastal ecosystems and societal function. At the coastal boundary, estuarine systems are subject to variability on a variety of spatio-temporal scales, and many are sensitive to anthropogenic activity such as built infrastructure, river damning, and climate change. *Geyer and MacCready* (2014) and *MacCready and Geyer* (2010) nicely summarize the considerable recent advances in communal understanding of estuarine circulation and tracer dispersion, which seek to unify the theory of estuarine dynamics in lieu of site-specific processes. However, conceptualization and quantification of physical processes in estuarine systems is dominated by studies conducted in systems with persistent or considerable freshwater inflow, termed "classical" (*Largier*, 2010).

Yet, there exist a class of estuaries that rarely fit into this paradigm, known as Low Inflow Estuaries (LIEs) due to their lack of persistent river flow (*Gräwe et al.*, 2009; *Hosseini and Siadatmousavi*, 2018; *Largier et al.*, 1996, 1997; *Winant et al.*, 2003; *Wolanski*, 1986). LIEs are characterized by hypersalinity, where the prefix "hyper" refers to the values being greater than the ambient ocean reference state, resulting from evaporation. LIEs are most abundant in Mediterranean climates around the world, but they may exist anywhere freshwater inflow tends to zero for a period of time comparable to the evaporative time scales of the basin. While they cannot be parameterized based on river flow rate, they are still often dynamically driven by along-estuary baroclinic pressure gradients. Thus, the application of the classical framework through which modern estuarine circulation and mixing is understood may prove fruitful in unifying or updating current constructs.

For classical estuaries, a balance of barotropic and baroclinic pressure gradients and friction can often describe the subtidal (i.e. tidally averaged or filtered) longitudinal dynamics quite well (e.g. *Hansen and Rattray*, 1965), and this balance is expected to hold for LIEs (*Winant et al.*, 2003). However, a variety of other processes have been found to be important in modifying the traditional balance in classical estuaries. For example, intratidal variability has been shown to be critical to modification of the stratification that drives subtidal longitudinal exchange (*Giddings et al.*, 2011; *MacCready and Geyer*, 2010). In addition, transverse circulation can redistribute longitudinal momentum through advection (*Lacy and Monismith*, 2001; *Scully et al.*, 2009) and result in mixing that is critical to the overall distribution of tracers (*Lerczak and Geyer*, 2004; *Lucas et al.*, 1999, 2009; *Ralston and Stacey*, 2005; *Smith*, 1977). Such processes have not been well-documented in estuaries where the direction of density-driven subtidal circulation is inverse that of classical estuaries.

In a curvilinear coordinate system with z denoting the vertical coordinate, positive upward, the transverse momentum equation is

$$\frac{\partial u_n}{\partial t}+u_s\frac{\partial u_n}{\partial s}+u_n\frac{\partial u_n}{\partial n}+u_z\frac{\partial u_n}{\partial z}-\frac{u_s^2}{R}+fu_s=-\frac{g}{\rho_0}\frac{\partial \eta}{\partial n}-\frac{g}{\rho_0}\int_z^0\frac{\partial \rho'(z')}{\partial n}dz'+\frac{\partial}{\partial z}A_z\frac{\partial u_n}{\partial z}, \tag{3.2.1}$$

where s is the streamwise (usually longitudinal) direction and n is the normal (or transverse) direction, and it is assumed that $u_s \gg u_n, u_z$. Here, density is decomposed as $\rho = \rho_0 + \rho'$ with ρ_0 a constant reference density taken to be 1000 kg m^{-3} and ρ' a function of space and time. η is the free surface above $z = 0$, R is the radius of curvature, f is Coriolis parameter, g is acceleration due to gravity, and A_ν is the vertical eddy viscosity. Contributions to the baroclinic pressure gradient from the density gradient integral between 0 to η have been omitted here under the assumption that $\eta \ll D_0$ where D_0 is the mean water column depth.

With minimal contribution of Coriolis acceleration and in the absence of flow curvature, the primary driver of transverse circulation is the lateral baroclinic pressure gradient, given by the second term on the right hand side of equation 3.2.1 (*Nunes and Simpson*, 1985). Lateral pressure gradients dominantly arise from transverse shear in the along channel flow acting on the longitudinal density gradient (*Smith*, 1977). In channelized, well-mixed estuaries with classical longitudinal density gradients, differential advection typically establishes lateral pressure gradients that form circulation cells with downwelling in the center of the channel on the flood tide, and upwelling on the ebb tide (*Guymer and West*, 1991; *Nunes and Simpson*, 1985). On a flood tide, these circulation cells move low momentum fluid to the channel flanks and reduce vertical shear, while on the ebb, the opposite is true, and the net effect is to force a residual longituinal circu-

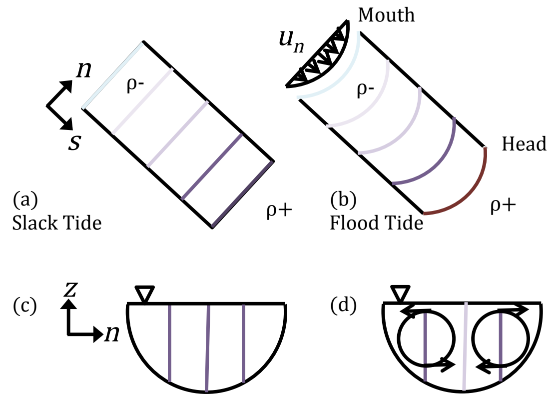

Figure 3.1: Schematic of differential advection during low stratification conditions. a) Plan view of the density distribution for an inverse estuary during slack tide. b) Plan view of the density distribution for an inverse estuary during flood tide, as indicated by the black along-channel/streamwise velocity (u_s) vectors. The gradient is distorted due to differential advection during flood tide. (c) Cross-section of density during slack tide. (d) Cross-section of density during flood tide with arrows indicating the density driven circulation. Lateral shear in the streamwise tidal velocity leads to surface divergence in the center of the channel and bottom convergence, which is the opposite of the expected flow structure in a classical estuary during flood tide.

lation that enhances the baroclinic-driven longitudinal circulation (*Lerczak and Geyer*, 2004; *MacCready and Geyer*, 2010). In addition to its importance on longitudinal dynamics, lateral circulation is important in its own right, as it tends to drive frontogenesis (*Giddings et al.*, 2012) and facilitate shoal-channel exchange that is important for biological processes (*Lucas et al.*, 1999, 2009) and salt transport (*Ralston and Stacey*, 2005).

In an estuary where curvature and Coriolis forcing were small with a relatively simple, quasi-parabolic and symmetric channel geometry, inverse longitudinal density gradients would hypothetically lead to differential advection of less dense water from the mouth of the estuary down the channel axis on the flood tide. Figure 3.1 depicts this scenario, and the resulting lateral baroclinic pressure gradients and transverse circulations that would be divergent at the channel center (i.e., opposite that of a classical estuary). A consequence of this motion would be to move higher momentum fluid at the surface from the channel center to the flanks, reducing the lateral shear in the tidal current, and reducing the transverse circulation. Conversely, the ebb tide would move lower momentum fluid from the channel center to the flanks, and this would enhance an inverse exchange circulation (convergent in the channel center during ebb).

A field experiment was carried out in Southern California during the summer to fall season of 2017 to test these hypotheses. The goals of the study were twofold: To first characterize the seasonal development of hypersalinity and inverse density gradients that should facilitate inverse exchange flow in a LIE, and secondly to test if in an inverse situation, the transverse circulation responds to the density inversion as depicted in Figure 3.1. The experimental setup and data processing are described in Section 3.3. Results showing key aspects of the seasonal variability in temperature, salinity, and velocity are described in Section 3.4. Section 3.5 gives a summary of the observations and a discussion contextualizing the observations in terms of the important estuarine processes of residual circulation, differential advection, and straining induced periodic stratification. Finally, future circulation scenarios in response to a changing climate are considered.

3.3 Data Collection

3.3.1 Field Site

To test these hypotheses, observations were taken throughout San Diego Bay California (SDB) during the summer to fall months of 2017. As one of California's five major ports, SDB, pictured in Figure 3.2, serves as an important hub for industry, commerce, recreation, and the U.S. Navy Pacific Fleet. With nearly 11,000 acres of marine habitat and foraging ground, and the third largest eel grass habitat area in California (*Merkel & Associates*, 2018), it is also an estuary of heightened ecological significance.

Because SDB is an LIE, distinct zonation of hydrographic properties along the bay axis has informed monitoring efforts, which section the bay into four ecoregions (*Sorensen et al.*, 2013). In addition to the hydrographically defined ecoregions, additional grouping of species between channel to intertidal water depths has shown variation among groups (*Williams et al.*, 2016), motivating the need to understand lateral variation and transport mechanisms.

In the northern and outer regions of the bay, buoyant bay water resides higher in the water column than the colder, denser ocean water. Density is thermally driven in this region and the circulation patterns exhibit classical estuarine flow (inflow at depth, outflow at the surface). Exchange between the bay and the inner-shelf is driven by horizontal and vertical tidal pumping at the bay mouth resulting from flood-ebb asymmetry (*Chadwick and Largier*, 1999a,b) and is strongly regulated by thermal stratification (*Chadwick et al.*, 1996).

Largier et al. (1997) show that along-channel density gradients within the bay are complex due to the competing contributions of both temperature and salinity. The bay exhibits both hyperthermal and hypersaline conditions (*Largier*, 2010). Net evaporation over the bay results in estuarine waters that are often saltier than the ambient ocean in the southern bay near the head (furthest inland and shallowest). In the summer months, when freshwater input to the bay is near zero due to lack of precipitation events that result in urban runoff and stream flow input, and the evaporation rate peaks at 125 cm yr^{-1} (*Peeling*, 1975), hypersalinity reaches its maximum (*Largier et al.*, 1996, 1997). SDB longitudinal temperature structure has a seasonal cycle as well giving way to a thermal region near the bay mouth that yields density gradients in the classical direction (*Chadwick et al.*, 1996; *Largier et al.*, 1997) during the warm season. The longitudinal variations in T and S result in regions of differing density dominance (*Largier et al.*, 1997), described as the thermal region near the mouth, the estuarine region near

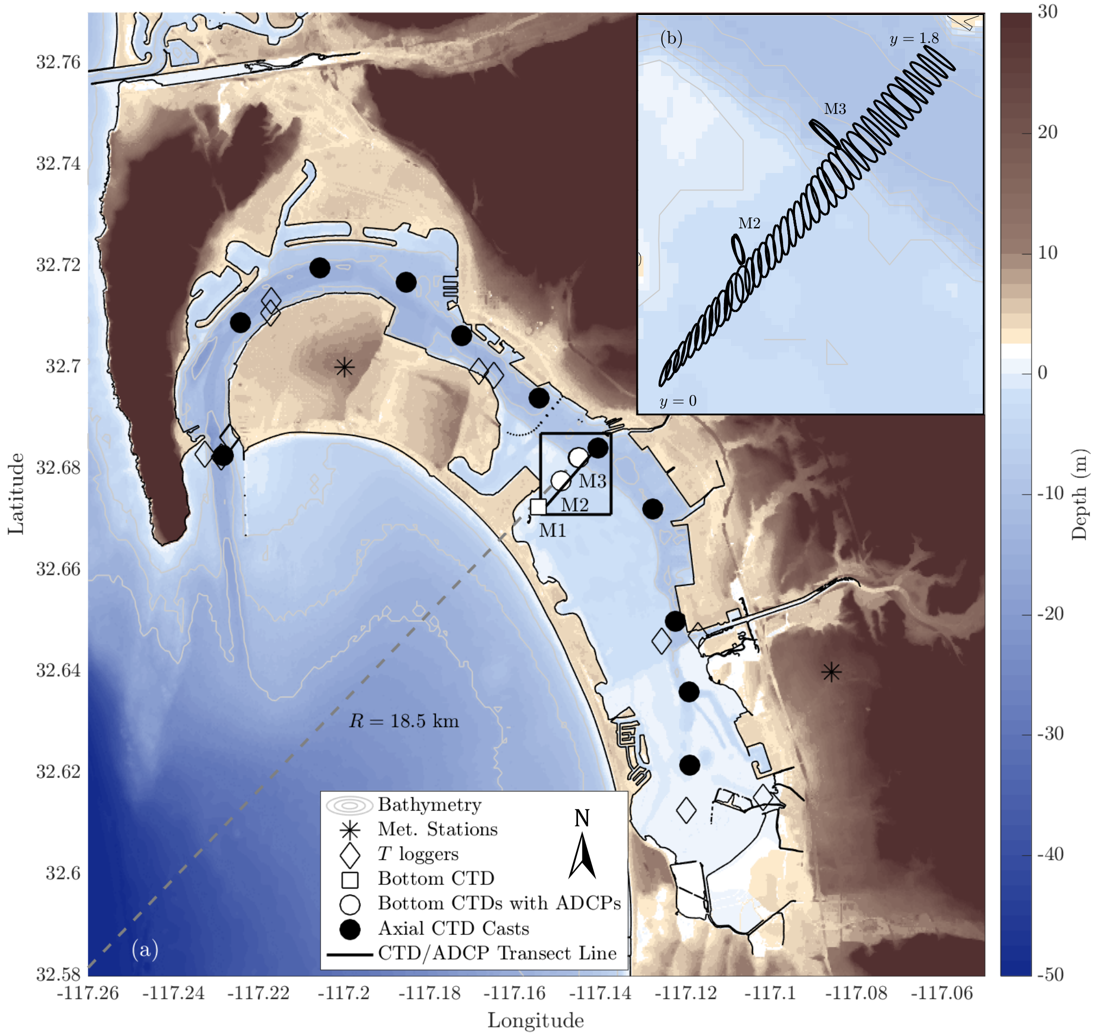

Figure 3.2: San Diego Bay, CA, USA bathymetry with observation locations and current principal axis ellipses (inset). Black diamonds indicate locations of temperature observations throughout the bay (near bottom at all locations and near surface outside of the channel). White circles/squares labeled M1-M3 indicate the mooring array with bottom mounted CTD and, at M2 and M3, velocity profilers tethered to thermistor chains that expand the lower portion of the water column. The black line along the mooring array indicates the location of repeat transects with underway ADCP surveys and CTD casts. Black circles indicate longitudinal hydrographic survey cast locations.

the head and the hypersaline region between the two (*Largier*, 2010). The evolution of the T and S fields, as well as the growth and decay of these zones are further described in this work, with discussion of the resultant baroclinic pressure gradients that may impact lateral processes.

SDB tides are mixed diurnal and semidiurnal and essentially propagate as a standing wave within the bay, with water level maxima/minima leading tidal current peaks in the main channel by $\frac{\pi}{2}$ rad (*Wang et al.*, 1998). During this experiment, the maximum tidal range observed was 2.9 m. Tidal prism has been shown to reach a maximum value of 43% of the bay volume during spring tides and minimum of 3% during neap tides in a barotropic model forced with at least 4 harmonic constants (*Wang et al.*, 1998). Thus, large variability in spring and neap dynamics is expected.

3.3.2 Experimental Setup and Data Processing

The observational time period (shown in Figure 3.3) was determined by assessing historical data collected at the estuary head by the Tijuana River National Estuarine Research Reserve (TRNERR; data not shown) for hypersaline conditions, which were conjectured to indicate the beginning of the transition to inverse conditions within the southern portion of the bay. Meteorological data from stations near the head and near the mouth (depicted as stars in Figure 3.2) indicate only 2 very small, localized precipitation events (Figure 3.3a) and fairly consistent air temperatures during the first half of the experiment with several warm events during the latter portion, until the final net cooling from Oct.–Nov. (Figure 3.3b).

Longitudinal Moorings

Temperature measurements using Odyssey Conductivity and Temperature loggers sampling every 15-minutes were taken along the bay axis (diamonds in Figure 3.2) in order to provide information on along-channel gradients on intratidal to seasonal timescales. Moored sensors were deployed 1 m off the bed at all locations shown in Figure 3.2 with a few near-surface sensors mounted on existing structures just below the low low water height outside of the channel in the northern portion of the bay where infrastructure allowed. Moorings near the channel were deployed near the channel edge due to heavy ship traffic throughout the bay. Co-located salinity observations proved more challenging to acquire due to sensor and maintenance limitations, and thus, the along-channel moored salinity data were not valid.

Lateral Moorings

Velocity profilers placed in the south central bay on the shoal and channel edge (locations M2 and M3 in Figure 3.2 respectively) were intended to reside within the hypersaline region south of the transition between the thermal and hypersaline regions as described in *Largier et al.* (1996). Each mooring consisted of a bottom Sea-bird SBE 37SM/37SMP-ODO CTD (Figure 3.3c-e) mounted with the ADCP (Figure 3.3h-i) which was tethered to a Sea-bird SBE 56 thermistor chain that extended through the lower portion of the water column. A bottom CTD was deployed at M1 without an ADCP. Over the shoal, at M1 and M2, the CTDs were outfitted with dissolved oxygen. Due to their greater energy consumption, these were set to sample every 5 minutes, while at M3 the CTD sampled every 1 minute. Thermistors sampled every 3 seconds. Boat traffic and Navy operations prohibited any near surface measurements, a large limitation in this study. Moreover, the salinity data at the cross-section mooring locations experienced intermittent failure due to sediment and biofouling. Egregiously bad data have been removed from the series, while some questionable data are pictured (specifically, salinity from M1 after September 12, shown as the blue line Figure 3.3d).

The blank space between the velocity time series shown in Figure 3.3 f–g represents a the time period of mooring recovery and redeployment. Reprogramming of instrumentation was necessary for each ADCP. During deployment 1, which lasted from June 6 to August 9, the Signature 1000 kHz ADCP at M2 was in a mean water depth of 5.0 m sampling at 8 Hz continuously in beam coordinates with 0.2 m bin spacing throughout the water column, yielding a horizontal precision of 26 cm s^{-1}. The first depth bin was centered at 0.6 m above the bed accounting for the instrument height and a blanking distance of 0.1 m. Due to battery limitation, the second deployment sampling scheme was altered to facilitate sampling through the end of the experimental period. During the second deployment, the M2 ADCP sampled at 2 Hz with 0.5 m depth bins, moving the first depth cell center to 0.9 m and reducing the horizontal precision to 7 cm s^{-1}. A 1200 kHz Teledyne RD ADCP was deployed at M3, sampling in mode 12 at 0.5 Hz (16 subpings every 4 ms) with 0.25 m depth bins and a blanking distance of 0.3 m. Accounting for instrument height, the first depth cell was 1.37 m above the bed. During the second deployment sampling was reduced to 0.25 Hz, while the beam coordinate configuration was maintained. Upon redeployment, the sea spider that the ADCP and CTD were mounted on was placed in a slightly different location, and due to the steep slope of the channel edge, ended up in deeper water. Thus, during deployment 1, the M3 ADCP recorded in 8.6 m depth and deployment 2 was in 10.8 m yielding a difference of 2.2 m depth.

ADCP data are averaged to 10 min ensembles resulting in standard errors of 0.3 cm s^{-1} and 0.01 cm s^{-1} during deployment 1 and 0.2 cm s^{-1} and 0.02 cm s^{-1} during deployment 2 at M2 and M3 respectively. After screening for data quality, each profile is rotated to the curvilinear coordinate system by aligning the streamwise velocity with the direction of maximum variance of the depth averaged velocity given by principal component analysis. Profiles are subsequently extrapolated to the surface with a parabolic fit using the uppermost two data points with fit parameters that assume no stress such that the shear goes to zero at the surface, as in *Giddings et al.* (2014), while near the bed, profiles are extrapolated with a cubic spline fit that employs a no slip bottom boundary condition (i.e. $u_n = u_s = 0$ in the bin closest to the bed). Extrapolated profiles are next interpolated to a regularly spaced sigma coordinate, $\sigma = (z+D)/D$, where D is the time varying depth and $\sigma = 0$ at the bed and $\sigma = 1$ at the surface where $z = 0$, which are then be mapped back to z coordinates (Figure 3.3f and 3.3g) for filtering. Subtidal (filtered) velocities (shown in Figure 3.3h and 3.3i) are calculated using a Godin filter (*Godin*, 1972), a sequential box average with 24, 25, and 25 hourly periods. This subtidal filter eliminates diurnal and higher frequencies associated with tides and winds illuminating the lower frequency oscillations due to fortnightly and seasonal forcing.

Figure 3.3: Summer 2017 deployment conditions showing: (a) precipitation recorded near the head (black) and near the mouth (green) of SDB (located at the black stars in Figure 3.2), P (mm), (b) air temperature, T_{air}, (°C), (c) bottom temperature, T_b, (°C) at the moorings labeled M1-M3 in Figure 3.2, (d) bottom salinity, S_b (PSU), (e) bottom density, ρ_b (kg m^{-1}), (f) streamwise tidal velocity, u_s, at M2 (m s^{-1}), (g) streamnormal tidal velocity, u_n, (m s^{-1}), (h) streamwise subtidal velocity, $\langle u_s \rangle$, (m s^{-1}), and (i) streamnormal subtidal velocity, $\langle u_n \rangle$, (m s^{-1}).

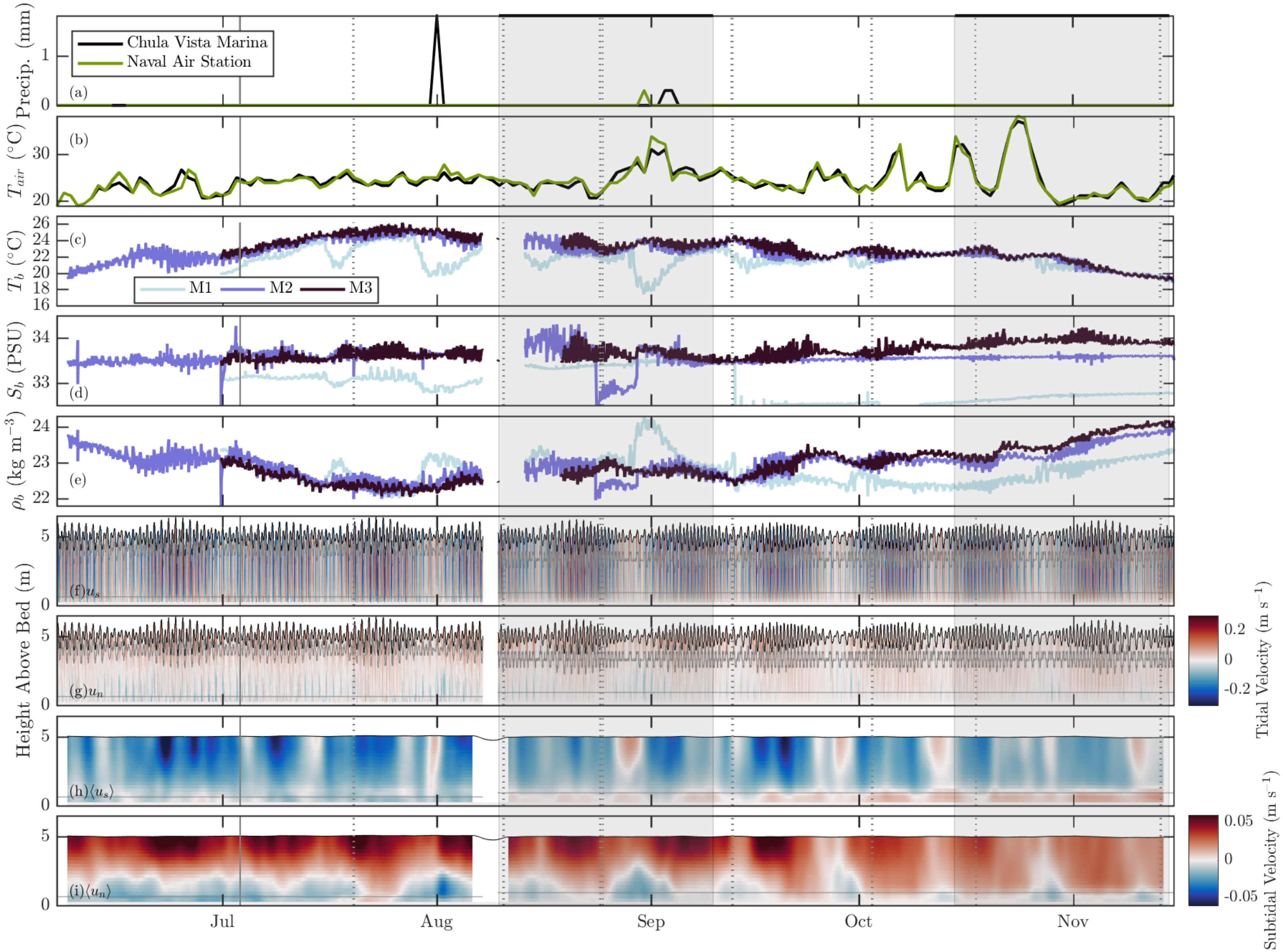

Chula Vista Marina
Naval Air Station
Precip. (mm)
T_{air} (°C)
T_b (°C)
M1
M2
M3
S_b (PSU)
ρ_b (kg m^{-3})
Height Above Bed (m)
(a)
(b)
(c)
(d)
(e)
(f)u_s
(g)u_n
(h)$\langle u_s \rangle$
(i)$\langle u_n \rangle$
Tidal Velocity (m s^{-1})
Subtidal Velocity (m s^{-1})
Jul
Aug
Sep
Oct
Nov

Longitudinal Transects

Axial hydrographic surveys conducted along the bay axis at the locations shown as black circles in Figure 3.2 using a Seabird SBE 25 Sealogger outfitted with pressure, salinity, temperature, and ECO fluorometer sensors during several spring flood tides provide a basin scale picture of the seasonal variability in temperature, salinity, and density. Water samples were not taken to calibrate the fluorescence measurements, however, so the information is purely qualitative and not used here. Downcast data, recorded at 10 Hz, has been processed using vertical bin averages of 0.2 m thickness and interpolated to a vertical grid ranging from 0 to 15 m depth with 0.1 m spacing using a cubic spline interpolation (resulting in data shown in Figures 3.4, 3.5, and 3.6). The distance indicated on the horizontal axis has been corrected for tidal advection using velocity from a moored Acoustic Doppler Current Profiler (ADCP) at M3, discussed below. A total of 11 axial surveys were conducted, of which 8 were conducted on spring flood tides (Figures 3.4-3.6), 1 was conducted on a neap flood tide (Figures 3.4f, 3.5f, and 3.6f), and 3 were conducted on spring ebb tides (not shown).

Lateral Transects

At 12.5 km upstream of the first axial CTD cast located at the bay mouth, which is defined to be the origin of the along-channel coordinate, an additional set of transects were conducted to investigate transverse dynamics (survey track shown as a black line in Figure 3.2). In addition to Seabird SBE 25 CTD casts, current velocities were measured using a towed 1200 kHz ADCP. Surveys were conducted before 10 of the 11 and after 8 of the 11 axial transects, thus depicting the early and late flood/ebb tides. The towed ADCP operated in mode 12 sampling at 1 Hz (10 subpings every 40 ms) with 25 cm depth bins, and a blanking distance of 35 cm. Accurate positioning was ensured with concurrent GPS data, while velocity measurements were referenced to bottom tracking.

Velocity sections shown in 3.9 and 3.10 have been spatially averaged to spatial bins of 40 m length along the track and rotated to a streamwise and streamnormal coordinate system based on the depth averaged principal axis direction using all survey data shown in Figure 3.2b. Because survey efforts were concentrated on the flood tides, this imposes a bias in the principal axis direction to the direction of flow curvature induced by filling of the shallows, as can be seen in *Wang et al.* (1998); *Fagherazzi* (2002); *Fagherazzi et al.* (2003). A spatially varying angle of rotation, as opposed to a single angle (as in *Lacy and Monismith* (2001)) or a time-varying rotation angle (as in *Nidzieko et al.* (2009)) was chosen to reduce the apparent divergence between the channelized tidal velocity and that over the shoal, so as to illuminate the streamnormal processes. There is good agreement between the depth averaged velocity principal axis direction at the mooring array adjacent to (just downstream of) the transect line (labeled M2 and M3 in Figure 3.2). The rotations result in a left-handed coordinate system fixed in time with positive streamwise values corresponding to the upstream (flood) direction and positive streamnormal values to the left of that (i.e. positive inland, negative toward the ocean side of the basin).

3.4 Observations

3.4.1 Longitudinal Structure and Dynamics

Longitudinal transects conducted 11 times over the observation period (Figure 3.4, 2 ebb tide transects not shown) show persistent along-channel salinity gradients of $\sim$1 PSU between the bay mouth and estuarine region (final cast location at 20 km upstream) for the majority of the experiment. Salinity within the south bay continues to increase from June (Figure 3.4a) to August (Figure 3.4f), after which the salinity between 14 and 18 km upstream decreases to a state similar to July (panel 3.4c). Salinity

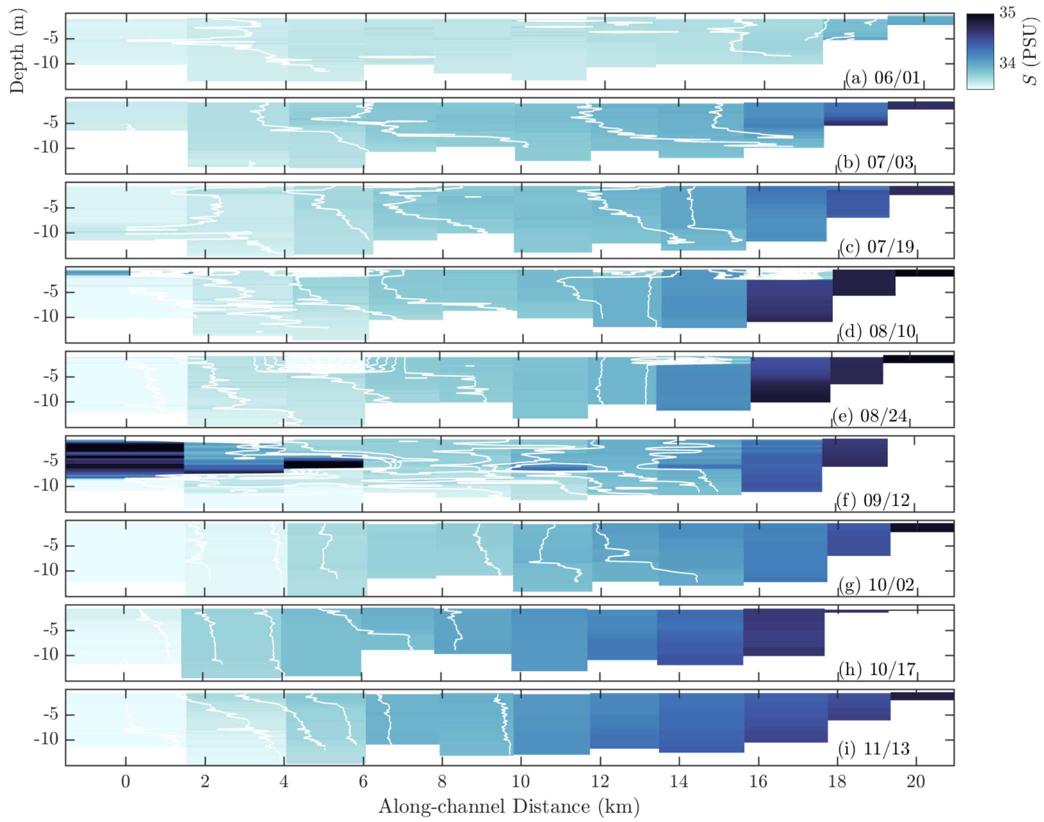

Figure 3.4: Along-channel cross sections of salinity (PSU). The contour interval is 0.1 PSU for all panels and the color ranges from 33.5–35 PSU. Cast locations are shown in Figure 3.2 as filled black circles. The x-axis corresponds to the along-channel distance between each cast location corrected for tidal advection. Panels (a–e) and (g–i) show surveys conducted during a spring tide, while (f) shows a neap survey.

again increases within this region through October, then decreases slightly again by November. Decreases in salinity are suspected to be due to freshening events from upstream following precipitation events. Despite episodic freshening events, the south bay remains hypersaline throughout the observational period.

Temperature sections in Figure 3.5 show the warmest waters in the south bay during July, early August, and September. The largest along-channel temperature gradient between the mouth and the head (10.5 °C) occurs in July. This is also observed in the near bottom temperature observations taken throughout the bay (not shown). As the bay cools, the along-channel temperature gradients minimize.

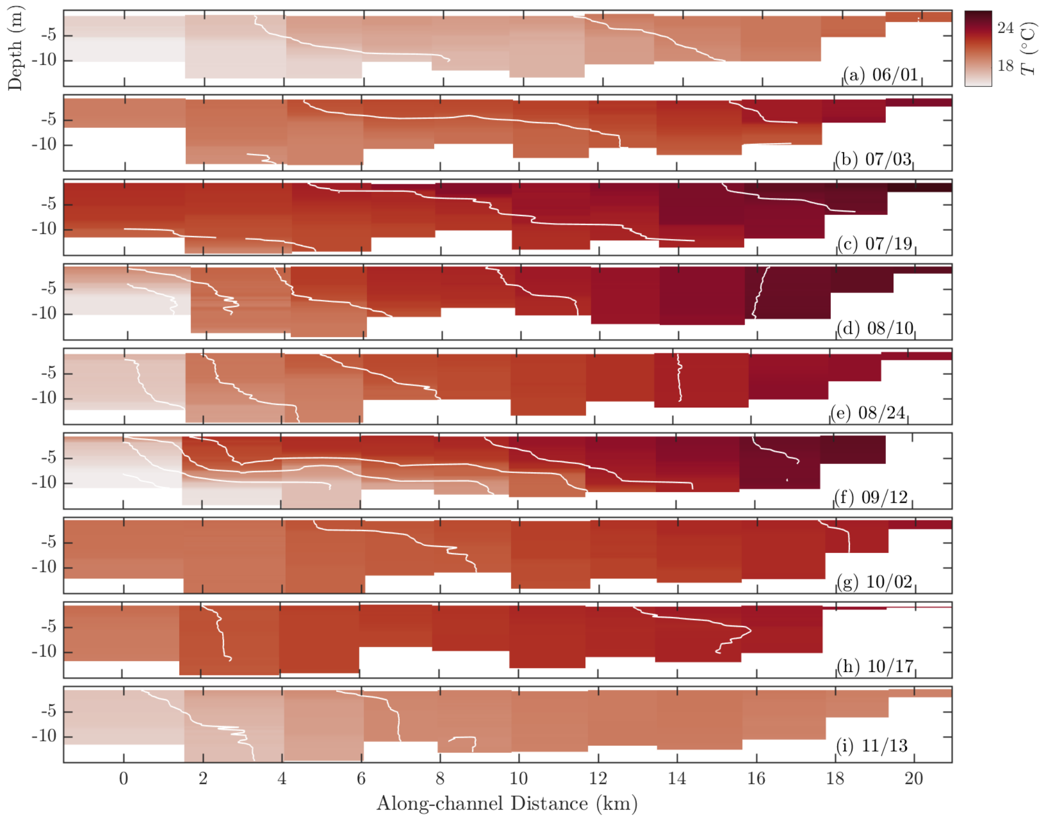

Figure 3.5: Along-channel cross sections of temperature (°C). The contour interval is 2 °C for all panels and the color ranges from 15–27 °C. Cast locations are shown in Figure 3.2 as filled black circles. The x-axis corresponds to the along-channel distance between each cast location corrected for tidal advection. Panels (a–e) and (g–i) show surveys conducted during a spring tide, while (f) shows a neap survey.

As bay temperature decreases and salinity increases, density within the bay increases (Figure 3.6). In July, warm waters facilitate longitudinal density gradients that would induce classical estuarine circulation in the south bay, despite inverse salinity gradients (Figure 3.4c). As the season progresses, the longitudinal gradient within the south bay decreases and then reverses and elongates, extending to the mid bay. Maximum inverse gradients are seen between October and November (Figure 3.4g–i) throughout the southern half of the bay.

On August 24 a full tidal cycle survey was carried out. A freshwater cap 5 km from the mouth results in a region of low density fluid in the thermal region. It is unclear whether this is due to an issue with the data collection, instrument malfunction, or a localized freshwater source. However, a corresponding ebb axial survey shows less pronounced freshening in a similar location, suggesting there may have been an anthropogenic source near the time of the survey.

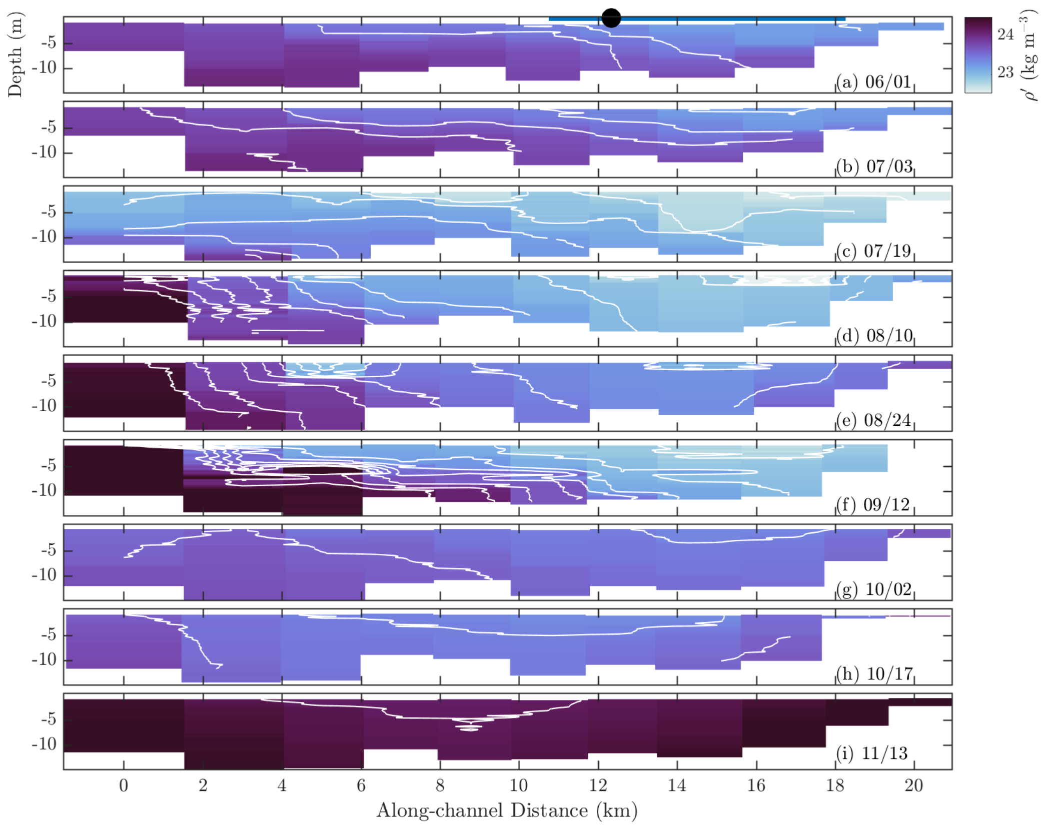

Figure 3.6: Along-channel cross sections of density (kg m^{-3}). The contour interval is 0.2 kg m^{-3} for all panels and the color ranges from 22.5–24.5 kg m^{-3}. Cast locations are shown in Figure 3.2 as filled black circles. The x-axis corresponds to the along-channel distance between each cast location corrected for tidal advection. Panels (a–e) and (g–i) show surveys conducted during a spring tide, while (f) shows a neap survey.

In an effort to view the seasonal trajectory of the observations compactly in T-S space, the difference, Δ, in depth averaged density, $\overline{\rho}$, for each longitudinal transect between $x = 11.8$ km and $x = 18.4$ km (indicated by the thick black line in atop Figure 3.6a) plotted as a function of the difference in depth-averaged salinity, $\overline{S}$, and temperature, $\overline{T}$. Density anomaly contours are centered at $\overline{\rho}$(35 PSU, 25°C). Similar figures have been shown in *Largier* (2010), which used the ocean-estuary difference as the Δ. Here the difference plotted is chosen to emphasize the density minimum present in the mid bay in fall and to capture the density field near our cross-section (indicated by the black dot atop Figure 3.6a). The dot size increases with time and the dotted line shows the trajectory. The horizontal path across isopycnal surfaces indicates the growth of hyper salinity during fairly constant temperature differences until the September warming event, which was observed during a neap tide. After this point, the trend is generally toward zero temperature difference with decreasing salinity differences. As can be seen by the dot color, the density difference across this inner-bay region starts off positive (i.e., classical) and becomes inverse for the last three transects with a fairly consistent seasonal trend (the exception being the neap tide).

Perhaps more informative to the question of density gradient inversion is the depth varying baroclinic pressure gradient shown in Figure 3.8, defined using the right hand side of the streamwise momentum equation (i.e. $-\frac{1}{\rho_0}\frac{\partial P_{Baroclinic}}{\partial s} = -\frac{g}{\rho_0}\int_z^0 \frac{\partial \rho'(z')}{\partial s}$). Panels (a) and (b) in Figure 3.8 correspond to panels (e) and (i) in Figures 3.4–3.6, respectively, and the circled dots in Figure 3.7. While it can be inferred from the density sections shown in Figure 3.6, the growth of the blue region near the head seen in Figure 3.8a to that in 3.8b clearly defines the expansion of inverse conditions due to increased extent of the hypersaline region from the south bay toward the central bay in the presence of cooler, reduced longitudinal temperature gradients. In late August (Figure 3.8a) the strongest baroclinic pressure gradients occur at the mouth in the thermal region. The anomalous freshwater cap 5 km from the mouth (Figures 3.4e and 3.6e) results in an inversion between the mouth and the mid bay. As previously noted, it is unclear

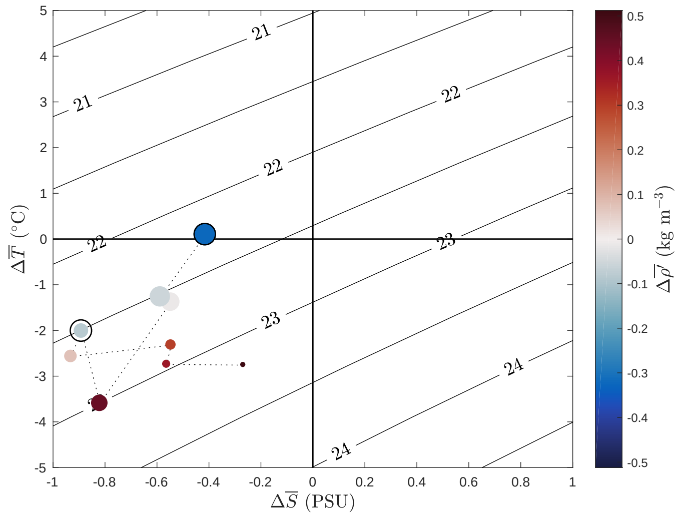

Figure 3.7: The difference, Δ, in depth averaged density, $\overline{\rho}$, for each longitudinal transect between $x = 11$ km and $x = 19$ km (indicated by the thick black line in atop Figure 3.6a) is plotted as a function of the difference in depth-averaged salinity, $\overline{S}$, and temperature, $\overline{T}$. Density anomaly contours are centered at $\overline{\rho}$(35 PSU, 25°C). Black circles indicate values associated with the surveys shown in Figures 3.8, 3.9, and 3.10. The circle size indicates time (latest is the largest).

whether this is due to an anthropogenic source, or is an artifact of bad data. However, the freshwater cap persists between a flood and an ebb survey on the same day as well as between the up and down cast, suggesting the former. In the mid bay, the baroclinic pressure gradient retains the positive direction and extends to 15 km from the mouth where the inversion occurs. By November (Figure 3.8b) this transition shifts toward the mid bay, ∼9 km from the mouth, yielding a much larger region of inverse baroclinic pressure gradient, albeit of weaker magnitude than those present near the head. Positive gradients in the thermal region are also weaker, a product of reduced temperature difference between the ocean and the estuary.

While Figure 3.7 suggests that the mooring array (located 12.5 km from the mouth) should have been in a region of inverse density gradients during late August as well as November, the depth varying baroclinic pressure gradient indicates that classical

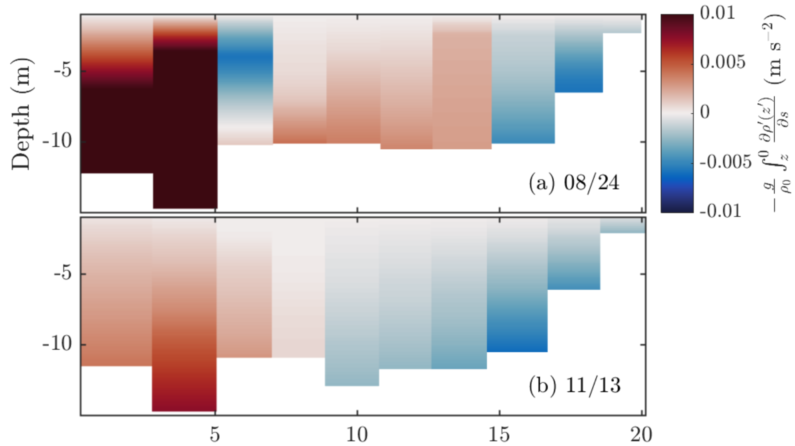

Figure 3.8: Longitudinal baroclinic pressure gradient in (a) classical and (b) inverse conditions. Dates correspond to the panels (e) and (i) in Figures 3.4–3.6 and the circled dots in Figure 3.7.

gradients were still present in the vicinity of the moorings in August. Though the metric presented in Figure 3.7 is useful for visualizing the seasonal progression of the estuarine state in the inner bay, the choice of a depth averaged metric differenced over 8 km may be a misleading indicator of inverse conditions. The limited T-S space spanned by an LIE renders the local gradient (i.e., that in Figure 3.4), the dynamically relevant quantity on tidal time scales, sensitive to seasonal variability, synoptic variability, localized input, as well as intratidal variability that is modulated on fortnightly time scales. Thus we consider inverse conditions near our cross-sectional array to start some time after the October longitudinal section.

3.4.2 Lateral Structure and Dynamics

Baroclinic forcing of transverse circulation will also be subject to these many scales of variability. Lateral cross sections of velocity and density are shown in Figures 3.9 and 3.10 for the same time periods as shown in Figure 3.8 throughout the tidal cycle, indicated by water level insets on panels a–d, which highlight tidal phase with color. Tidal phase is defined based on water level minima and maxima, with corresponding peak ebb/flood velocities in the channel at roughly $\pi/2$ and $3\pi/2$ (water level and velocity are nearly 90 degrees out of phase). Lateral transects were carried out before and after the corresponding longitudinal transects, placing them just before and after the peak flood/ebb velocities at M2. There was not a longitudinal transect between the flood-ebb transition. Earth coordinate velocities have been rotated to u_s and u_n as described in Section 3.3.2. Streamnormal velocity magnitude is approximately 50% of streamwise velocity, and thus, the colorscale between the top and middle panels has been tightened to emphasize lateral structure. The panels are ordered in time, and because the August full tidal survey was conducted from flood through ebb, while the November survey was conducted from ebb through flood, the panels are not directly comparable between Figures 3.9 and 3.10. In lieu of a missing ADCP transect due to marine battery failure on the first lateral ebb survey of 08/24, velocity profiles at the mooring locations (relative position shown atop Figure 3.9a) are plotted in Figure 3.9c and 3.9g.

Streamwise velocity structure consistently shows the strongest flood velocities near the channel slope, indicative of influence by some combination of bathymetry, basin geometry, and potentially Coriolis forcing (discussed further in Section 3.5.2). Draining of the shoals enhances u_s on the ebb tide over the shallow regions (Figures 3.9c and 3.10a). Transverse velocity is much noisier, particularly between tidal phase of π and $3\pi/2$. Larger u_n occur after peak ebb and flood, and show some instances of convergence/divergence. In Figure 3.9f, this occurs in the center channel and appears to be associated with the associated with slumping of the isopycnals after differential advection of denser ocean water has set up a lateral gradient on either side of the channel slope. This mechanism is consistent with the classical view of lateral circulation driven by differential advection, which is expected based on the apparent longitudinal density field and gradients presented in figures 3.6 and 3.8. Ebb currents restratify the water column and lead to a two layer circulation cell that extends from the channel over the

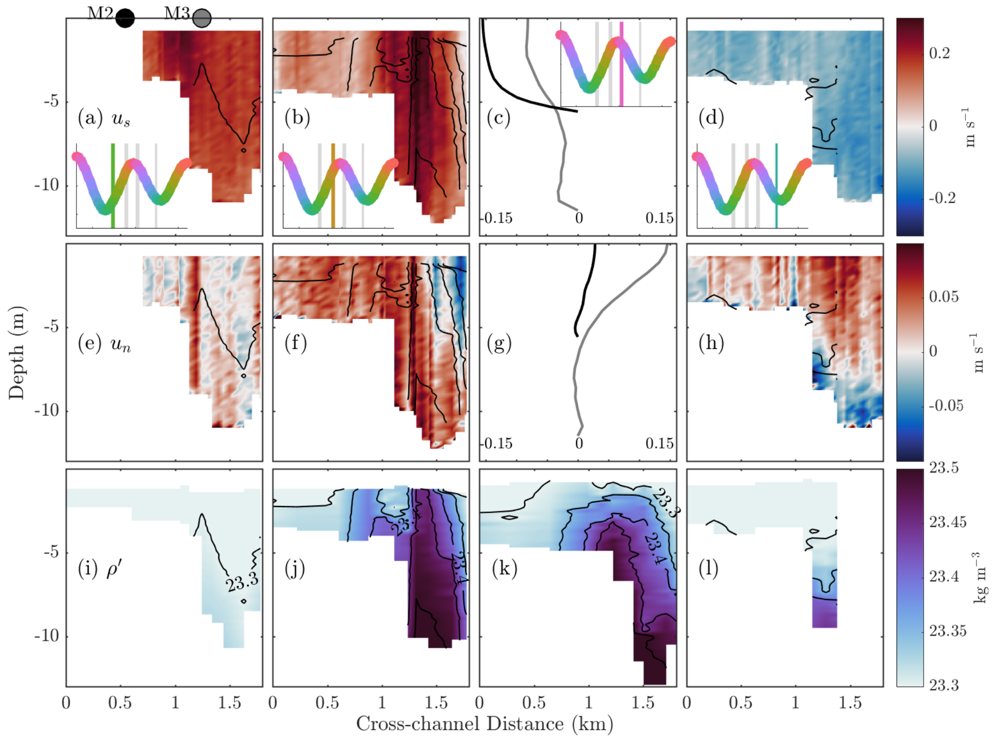

Figure 3.9: Cross sections across the lateral transect line in Figure 3.2 showing (a)–(d) streamwise velocity, water level, and tidal phase, (e)–(h) streamnormal velocity, and (i)–(l) density anomaly with contours every 0.05 kg m^{-3}. Mooring locations just downstream of the transect line are shown atop panel (a).

shoal with surface flows toward the channel and bottom layer flows toward the shoal. This structure is seen in the u_n time series at both M2 (Figure 3.3g and 3.3i) and M3 (not shown) during the early months of the experiment. Restratification is consistent with the process of periodic stratification induced by tidal straining of the longitudinal density field (*Ralston and Stacey*, 2005; *Simpson et al.*, 1990), wherein mixing induced by bottom stress destratifies the water column on the flood tide, and restratifies on the ebb as lighter upstream water is advected over denser water.

During inverse conditions, streamwise velocity shows a structure similar to classical conditions, while the transverse velocity is weaker overall and less coherent. On the ebb tide, the lateral uniformity of the persistent two layer feature breaks down. This

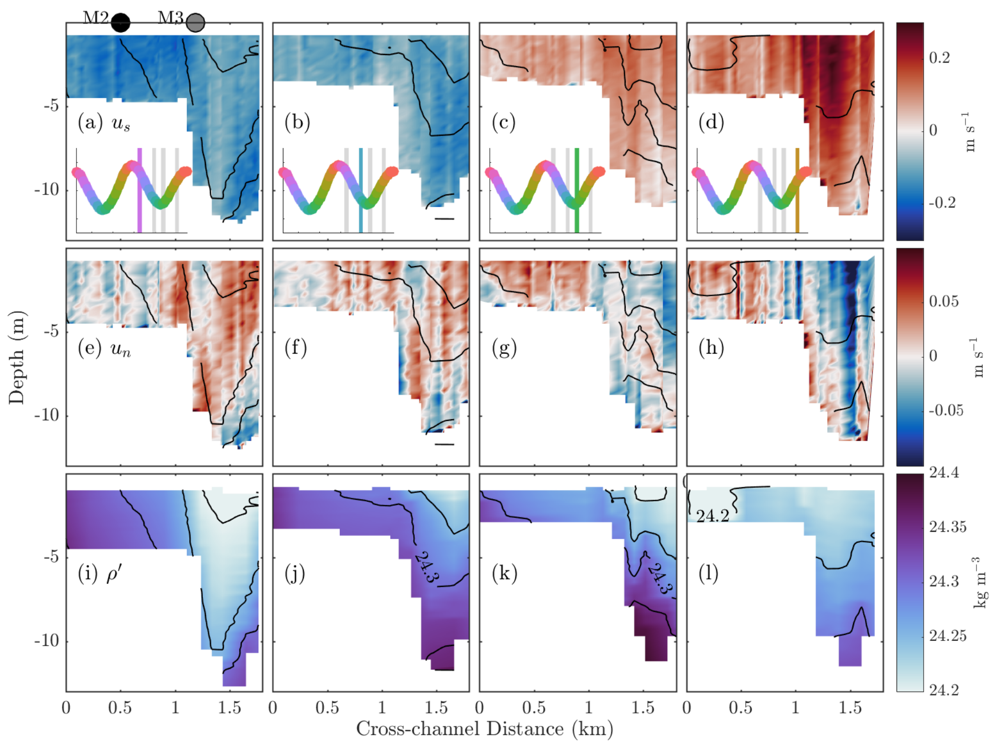

Figure 3.10: Cross sections across the lateral transect line in Figure 3.2 showing (a)–(d) streamwise velocity, water level, and tidal phase, (e)–(h) streamnormal velocity, and (i)–(l) density anomaly with contours every 0.05 kg m^{-3}. Panels (c) and (g) show mooring profiles in lieu of missing towed ADCP data. Mooring locations just downstream of the transect line are shown atop panel (a).

is also apparent in the u_n time series at M2 (Figure 3.3g and 3.3i) and M3. On the ebb tide, two areas of weak surface divergence within the channel and over the shoals border an area of weak convergence over the channel slope (Figure 3.10e and 3.10f). During the early flood tide the convergence shifts to over the shoals, and stronger negative velocities start to develop at the surface within the channel. After peak flood, the convergence migrates farther over the shoals, and surface velocities enhance within the channel (Figure 3.10h). Were it not for the strong band of negative u_n in the center channel (Figure 3.10h), which may be a result of averaging methods, there might appear to exist a two layer flow within the channel to channel slope that has negative surface velocities and positive bottom velocities, opposite that of those seen in on the ebb tide in classical conditions.

The density range displayed between both time periods is the same, but the values are 1.1 kg m^{-3} higher during inverse conditions (comparing panels i–l in Figures 3.9 and 3.10). Throughout the experiment, the transition to ebb velocities happens over the shoals first leading to higher ebb velocities over the shoal than in the channel during the early ebb. This lateral phase shift differentially advects denser water upstream over the shoals during inverse conditions. The lateral gradients are largest, and stratification is weakest during the ebb tide, as was shown to be the case during flood tides in classical conditions. Thus, while the structure in Figure 3.10i might be expected during a flood tide, the phase shift of u_n between the shoals and the channel leads to a density field with more significant lateral baroclinic pressure gradients. The enhanced stratification during the flood tide (Figure 3.10k) is also in contrast to classical conditions, as well as the concept of tidal straining induced periodic stratification.

To examine differences in structure and strength of transverse velocity between M2 and M3 during classical and inverse conditions, sigma coordinate velocities are deconstructed using empirical orthogonal function (EOF) analysis on the full second deployment time series (August-November). Phase averaged EOF mode 1 and mode 2 are shown separately in Figure 3.11 for both moorings during classical and inverse conditions (Figure 3.11 left and right respectively). In Figure 3.3 the averaging time periods are shown as shaded boxes, which were defined based on longitudinal cross sections. Mode 2 holds a significant portion of the variance at both M2 and M3 (listed on the left panels). The uppermost two panels yield similar structure in both classical and inverse conditions. This is to be expected because, although the reconstructed velocity can not be directly attributed to any process, the structure does respond to barotropic forcing, which is not expected to change between the two time periods, as there was negligible freshwater inflow at this time and the difference in tidal range was only 5 cm. The magnitude of mode 1 at both M2 and M3 decreases markedly during the ebb tide (from 0 to π), and slightly during the flood tide (π to 2π), during inverse conditions at both moorings. Mode 1 velocity at M2 is positive throughout the tidal cycle, indicating barotropic forcing other than the tides is important for the transverse circulation over the shoal, while at M3, velocities are positive during the ebb and negative during the flood.

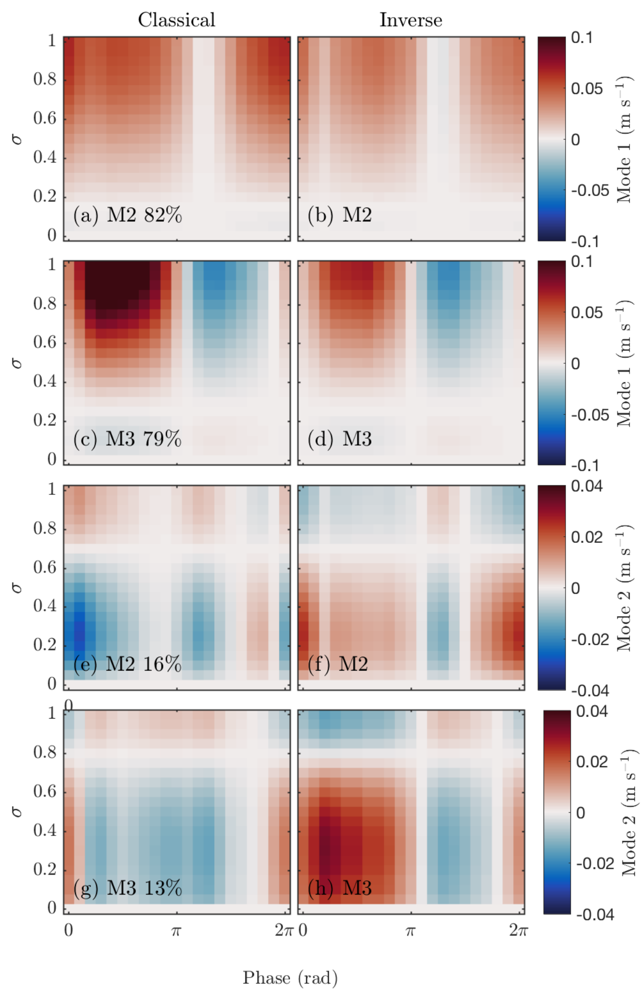

Figure 3.11: Phase averaged transverse empirical orthogonal functions showing mode 1 (a)–(d) and mode 2 (e)–(h) during periods with classical (left panels) and inverse (right panels) longitudinal density gradients. EOFs are calculated using the full time record for deployment 2, while the time period of phase averages are indicated by the gray boxes in Figure 3.3.

Mode 2 velocities may be thought of as a shear velocity driven by any number or combination of processes (*Giddings et al.*, 2014). The shear layer occurs over lower sigma levels at M2 than at M3, which correspond to approximately 1.5 and 2 m from the surface respectively, indicating that the z-level thickness of the upper layers are comparable between the two moorings. The sign is consistent between the two moorings and both show reversed circulation for a brief period of time during the flood tide, albeit at different phases. The sign change between classical and inverse conditions provides strong evidence that the baroclinic pressure gradient is at least in part contributing to the shear velocity, as this is the main forcing mechanism that changes sign between the two time periods (see Figures 3.9i–3.9l and 3.10i–3.10l). At this point, the reason for the phase shift between the two moorings is unclear, and is left for further investigation discussed in Section 3.5.

During classical conditions, mode 1, which is strongly positive at the surface and decays to zero at depth, and mode 2, which is positive at the surface and negative at depth, act in concert to enhance the two-layer circulation seen during the ebb tide in classical conditions. Conversely, in inverse conditions, the shear velocity opposes the mode 1 velocity structure. The net result is to reduce, but not entirely reverse, the transverse flow in inverse conditions. The sums of modes 1 and 2 are shown in the phase averaged profiles pictured in Figure 3.12. The strong positive surface velocities and negative velocities in the lower layer seen during the ebb in classical conditions can be seen in panels 3.12c and e, while in inverse conditions the profiles are more uniform due to opposite signs of mode 1 and the shear velocity (mode 2) in the surface layer. Panels a–b and k–l show that the ebb circulation patterns develop over the shoals before the channel due to bed friction being more important in shallower water (the shoals). Despite reduced velocities at both moorings during the flood tide (panels 3.12g–3.12j), the general direction of flow does not change. Thus, transverse velocities respond to

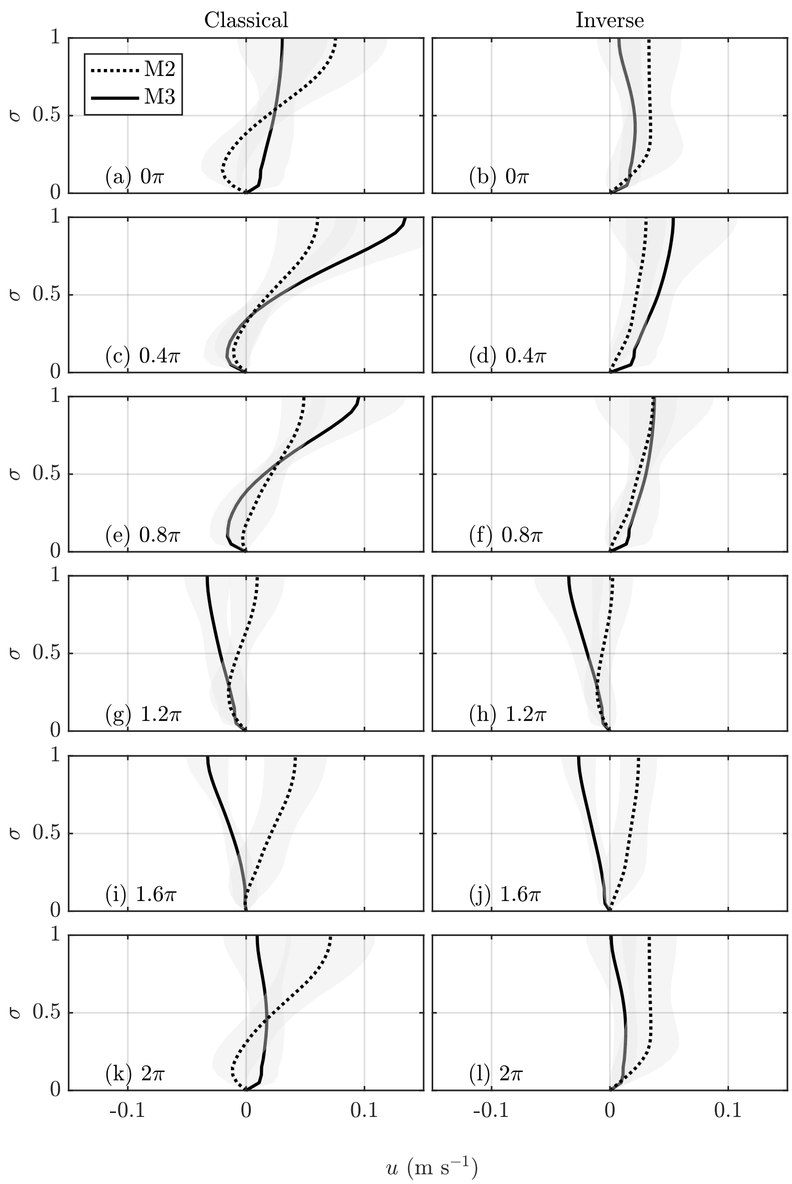

Figure 3.12: Profiles of the sum of the first two streamnormal EOF modes at M2 (dashed line) and M3 (solid line) phase averaged during periods with classical (left panels) and inverse (right panels) longitudinal density gradients, indicated by the gray boxes in Figure 3.3. $\pm$ 1 standard deviation of the average is shaded in gray. Tidal phases are (a)–(b) 0π - beginning of ebb, (c)–(d) 0.4π - early ebb, (e)–(f) 0.8π - late ebb, (g)–(h) 1.2π - early flood, (c)–(d) 1.6π - late flood, (k)–(l) 2π - end of flood.

inverse longitudinal density gradients by decreasing the magnitude of the first mode and homogenizing an initially highly sheared lateral velocity structure.

3.5 Summary and Discussion

3.5.1 Summary

The measurements presented here capture the evolution of hypersalinity in SDB and the growth of inverse baroclinic pressure gradients within this LIE. Axial transects and temperature time series confirm that the density structure is subject to a delicate balance between salinity and temperature which is sensitive to small variations in T and S, leading to inverse conditions that vary in time and spatial extent through the summer to fall season. Longitudinal and transverse sections indicate that straining induced stratification reverses sign in the inverse conditions relative to classical. Moored velocity profilers show strong cross-channel circulation that varies within a tidal cycle, responding to lateral density gradients formed through differential advection of the longitudinal density in both classical and inverse conditions. However, this response does not completely reverse lateral circulation as hypothesized for an idealized estuary geometry (shown in Figure 3.1) due to the dominance of other processes important to the lateral momentum budget as well as the strong deviation from an idealized geometry.

3.5.2 Circulation

While it is apparent that over the course of the experimental period longitudinal density gradients, and hence baroclinic pressure gradients, reversed in the vicinity of the moorings, the subtidal $\langle u_s \rangle$ did not appear to reverse, with the exception of during neap tides. A possible explanation for this is that the basin geometry and depth variation play a larger role in subtidal circulation than baroclinic pressure gradients during spring tides, or there is lateral variability in $\langle u_s \rangle$ which yields these results over the slope but may be different in the channel center. *Valle-Levinson* (2008) discuss the importance of Coriolis forcing in estuaries with differing basin width, bed slope, and stratification in classical estuaries. The relevant quantities are the Kelvin number and the Ekman number.

The Kelvin number, given by $K = \frac{W}{R_d}$, compares the width of the basin, W, to the baroclinic Rossby radius of deformation, $R_d = \frac{\sqrt{g'h}}{f}$, where $g' = g\frac{\Delta\rho}{\rho_0}$ is the reduced gravity and h is the mean water column height in the channel. K is approximately 1.3 for SDB, based on a width of 2.7 km, f at the mooring location, $\Delta\rho = 0.2$ kg m^{-3} as in the lateral transects presented in Section 3.4, and a depth of 13 m. The Ekman values are given by the $Ek = \frac{A_z}{fh.^2}$. An estimate of A_z at M3 can be calculated with the 10 min ensemble averages of vertical shear in the along channel flow and the streamwise Reynolds stress calculated using the variance technique of *Stacey et al.* (1999), i.e. $u_s'u_z' = -A_z\frac{\partial u_s}{\partial z}$ where primed velocities are the fluctuations from the the 10 min ensemble averaged u_s and u_z and the left hand side is the ensemble average. Using an order of magnitude estimate of $u_s'u_z' \sim O(10^{-4})$ and $\frac{\partial u_s}{\partial z} \sim O(10^{-2})$ based on observations at M3, the resulting $A_z \sim O(10^{-2})$, which is consistent with a midwater column deployment average of $A_z = 0.018$ m^{2}s^{-1}, yielding $Ek \sim O(1)$. Cross sections presented in *Valle-Levinson et al.* (2003) imply that SDB is in a regime influenced by both f and friction, potentially resulting in the persistent features in the streamwise and streamnormal velocities seen in Figure 3.3 panels h–i. Interpretation of the subtidal circulation over the basin and across the cross section in the context of *Valle-Levinson et al.* (2003) should be done with caution, however, as the longitudinal density gradient prescribed for those solutions was in the classical direction, and thus may yield differing results for an inverse estuary.

Moreover, subtidal velocity is impacted by asymmetries in the flood and ebb phases of unsteady oscillatory tidal flow interaction with basin geometry and depth variations (*Li and O'Donnell*, 1997; *Pein et al.*, 2014). It is clear that the channel configuration combined with the steep slope from the channel to the shoals plays a role in both the subtidal and tidal dynamics in SDB. A barotropic numerical model (*Wang et al.*, 1998) and analytic solutions that solve for the potential and stream functions show significant curvature in the region of M2 and M3, as was confirmed by the principal axis directions of the lateral transects. The crescent shape of SDB results in a large radius of curvature (Figure 3.2), indicating that this term should be small in the momentum equations. However, local irregularities in the coastline bounding the estuary can act as headlands which tend to force secondary circulation (*Garrett and Loucks*, 1976; *Kalkwijk and Booij*, 1986) as well as downstream eddies in the region of flow separation (*Geyer*, 1993) that are also manifested in the subtidal flow field (*Yang and Wang*, 2013). It is likely that both filling of the shoals, as well as curvature induced by the coastline irregularity near the moorings forces the mode 1 transverse flow throughout the experiment. During classical conditions, the shear velocity, representative of the baroclinic flow, enhances this circulation at the surface, while reversing it at depth, leading to an exchange flow that traverses the channel to shoal. In inverse conditions, this exchange is shut down by a shear flow that opposes the barotropic flow.

3.5.3 Stratification and Mixing

In addition to reversed transverse shear velocity, inverse longitudinal density gradients appear to accompany straining induced stratification during the opposite phase of the tide as seen in classical estuaries (*Simpson et al.*, 1990) and observed during classical conditions in SDB (Figure 3.9i–3.9l). Periodic stratification typically arises on the ebb tide due to straining of the longitudinal density gradient, while on the flood tide, mixing induced by the bottom boundary destabilizes the water column and remixes the stratification that was created during the ebb (termed Strain Induced Periodic Stratification - SIPS; *Burchard et al.*, 1998; *Simpson et al.*, 1990). This pattern of stratified and well-mixed conditions is evident in the density cross sections presented in Figures 3.9i–3.9l and is shown to occur during the opposite tidal phase in inverse conditions Figure (3.10i–3.10l). In classical estuaries, the resultant streamwise velocity profiles exhibit greater shear on the ebb and are more depth uniform on the flood (*MacCready and Geyer*, 2010). To examine this structure in SDB, profiles of the sum of the first two streamwise EOF modes are plotted throughout the tidal cycle as in Figure 3.12. During classical conditions (left side of Figure 3.13) the traditional evolution of velocity is observed at both M2 and M3, with the exception that the ebb shear layer at M3 is lower in the water column due to a subsurface maximum, which is hypothesized to occur as a result of interactions with bathymetry or basin geometry discussed in Section 3.5.2. During inverse conditions, there is little change at both M2 and M3 during the flood tide (Figure 3.13h and 3.13j), while during the ebb tide, there is some indication of homogenization at M2 during the early ebb that does not persist, and clear homogenization at M3 indicated by the reduced subsurface maximum (Figure 3.13d and 3.13f). While the velocity profiles do not completely reverse expectations due to SIPS during inverse conditions, inverse stratification is observed. During inverse conditions, flood tides are more stratified than ebb tides (see Figure 3.10i–3.10l).

3.5.4 Climate Change Impacts and Relevance To Marine Organisms

The seasonal variability in SDB water properties, which ultimately impact circulation and dispersion within the estuary, is vulnerable to a changing climate. Increases in extreme events but more dry days overall with increased precipitation in the core winter months and decreased precipitation in the spring and fall (*Kalansky et al.*, 2018) may contribute to longer periods of hypersalinity. Downscaled climate models predict

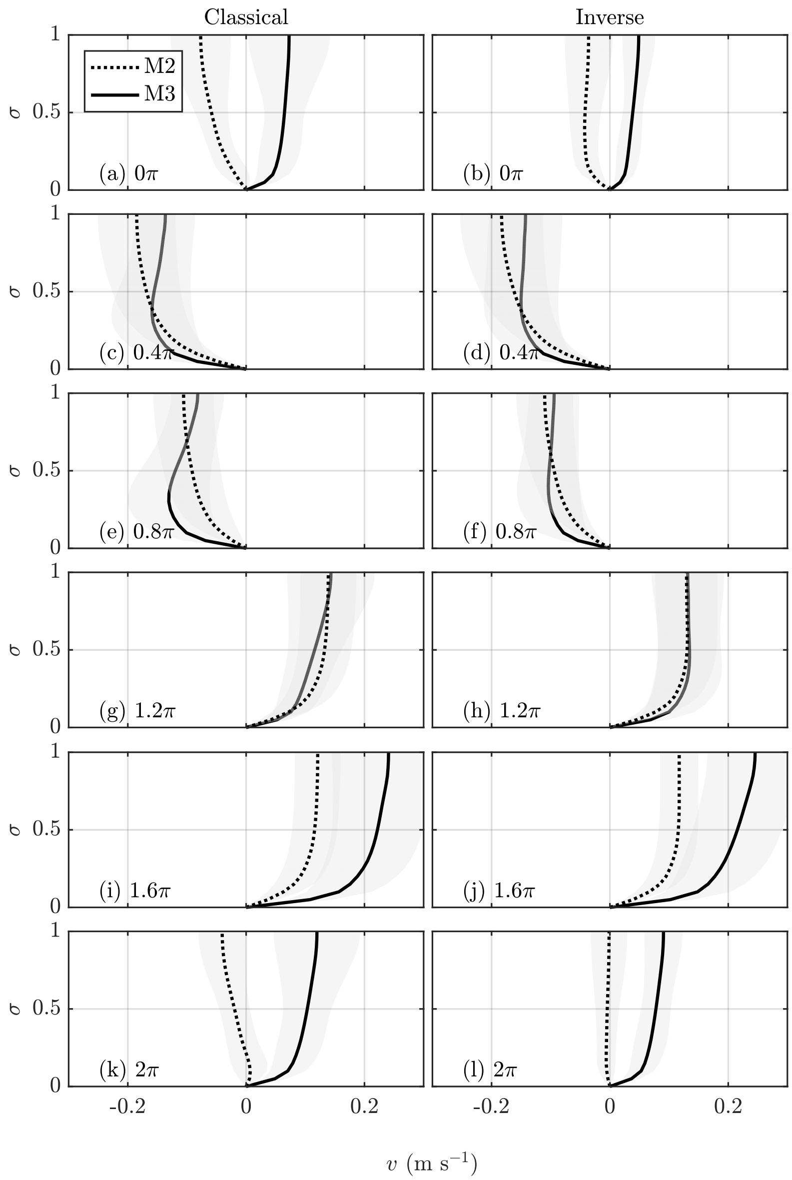

Figure 3.13: the sum of the first two streamwise EOF modes at M2 (dashed line) and M3 (solid line) phase averaged during periods with classical (left panels) and inverse (right panels) longitudinal density gradients, indicated by the gray boxes in Figure 3.3. $\pm$ 1 standard deviation of the average is shaded in gray. Tidal phases are (a)–(b) 0π - beginning of ebb, (c)–(d) 0.4π - early ebb, (e)–(f) 0.8π - late ebb, (g)–(h) 1.2π - early flood, (c)–(d) 1.6π - late flood, (k)–(l) 2π - end of flood.

the largest increases in air temperature for the San Diego region at the end of the summer into the fall (*Kalansky et al.*, 2018), which may slow the progression of inverse conditions towards the central bay, despite prolonged dry periods. There is large uncertainty, however, in temperature trends near the coast (*Kalansky et al.*, 2018) due to the influence of coastal Marine Layer Clouds that are not well represented in current climate models (*Torregrosa et al.*, 2014) but have the potential to regulate air temperatures (*Clemesha et al.*, 2018). Given the importance of estuarine temperature change in allowing hypersaline conditions to give way to inverse conditions, SDB will be sensitive to both air temperature, through combined effects of atmospheric heat fluxes as well as the feedback on evaporation rates, and ocean temperature changes that result from climate change. These trends may be important for species sensitive to small shifts in temperature such as the East Pacific green sea turtles that use the bay for thermal refugia (*Madrak et al.*, 2016), as well as other organisms comprising the over 311 MT of biomass (*Williams et al.*, 2016) that rely on water property distribution, circulation patterns, and mixing zones in forming ecosystem homeostasis.

3.5.5 Conclusions

Differential advection in the presence of inverse longitudinal baroclinic pressure gradients has been hypothesized here to lead to lateral circulation in an LIE. The mechanism is the same as that occurring in classical estuaries, but is reversed due to the inversion of longitudinal density gradients. The observations show a more complex response than that hypothesized in Figure 3.1 given the complex lateral bathymetry and the location of the along-channel velocity maximum over the shoals rather than in the channel center (as expected for an idealized geometry). Altered lateral gradients, consistent with this hypothesis, lead to a sign change in the phase averaged mode 2 EOF of transverse velocity at 2 mooring locations, suggesting that baroclinic pressure gradients driven by differential advection of the inverse longitudinal density distribution may contribute to the lateral momentum balance. However, the full tidal lateral velocity does not support a complete inversion of the flow field, which suggests that alternative mechanisms also contribute to lateral circulation. Further work will assess the terms in the lateral momentum balance, to the extent the observations allow, to identify the dominant forcing. It is likely that circulation due to the geometry of the bay is important. Similarly, inverse conditions lead to a straining induced periodic stratification which is inverse of that expected during classical conditions (more stratified during flood tides as opposed to more stratified during ebb tides under classical conditions). Finally, given the highly sensitive nature of this estuary, and other LIEs to small changes in salinity and temperature, a possible significant change in these patterns might occur under future climate conditions.

3.6 Acknowledgements

The authors would like to thank the Center for Coastal Studies and the Navy Marine Ecological Consortium technitians, contractors, and field crew as well as all of the volunteers who helped conduct the hydrographic surveys presented here. Additionally, A.R.R. would like to thank I. Arzeno, M. E. Harvey, and A. Palóczy for useful conversations regarding deployment preparation and data processing and analysis. This material is based upon work supported by the NSF GRFP under grant DGE-1144086 and the Naval Research Enterprise Internship Program.

Chapter 3 is currently being prepared for submission for publication of the material, and will be submitted as, Lateral circulation in a low-inflow, seasonally hypersaline estuary by Rodriguez, A. R., S. N. Giddings, J. J. Bredvik and S. E. Graham. The dissertation author was the primary investigator and author of this material.

Chapter 4

Summary and Conclusions

Ocean heat uptake and freshwater incorporation occur at a variety of length scales (*de Boyer Montégut et al.*, 2004), after which, water masses are modified and transported within the ocean interior (*Ganachaud and Wunsch*, 2000; *Groeskamp et al.*, 2019; *Wijffels et al.*, 1992). Understanding the mechanisms through which buoyancy is mixed into and transported within the ocean is critical for a number of problems facing coastal societies and ecosystems including climate change, sea level rise, eutrophication, sediment transport, algal blooms, and pollution management. This dissertation has advanced current understanding of several processes pertinent to these issues. The sections below provide summaries of each chapter with some recognition of the questions that remain unanswered.

4.1 Chapter 1

Oceanic circulation plays a significant role in delivering heat to the Antarctic ice shelves (*Holland et al.*, 2008). In Chapter 1, a heat transport pathway to the Amundsen Sea is identified using a Southern Ocean state estimate. In the Amundsen Sea region, the southern branch of the Antarctic Circumpolar Current veers southeastward with a transport of over 1 Sv just north of the shelf break. Relatively warm Circumpolar Deep Water crosses the steep continental shelf slope into the marginal sea in several locations at all depths, with a consistently positive integrated temperature transport throughout 2005–2010. On the Amundsen shelf, below the permanent pycnocline the heat budget is dominated by the divergence of heat advection across the domain boundaries, while diffusion acts to cool the shelf waters to a lesser extent. A follow-on study by *Palóczy et al.* (2018) suggests that heat estimates provided here compare well to those made in an eddy-permitting model with finer resolution than the state estimate utilized in this study, and that the relative role of surface buoyancy and wind forcing, bathymetry, and circulation on the inner and outer shelf varies across the entire Antarctic shelf. Moreover, *Stewart et al.* (2018) suggest that tides are also important. Thus, future work must consider the myriad of complex processes occurring on the Antarctic shelf in order to fully address the role of ocean circulation in forcing ice sheet basal melt.

4.2 Chapter 2

Chapter 2 studies the impacts of wave-current interaction on mixing and transport of small-scale freshwater plumes using a fully coupled 3-D hydrodynamic and spectral wave model. Simulations indicate that in the presence of waves the plume is confined to the coast and spreads alongshore until it lifts off of the seabed. Turbulent kinetic energy provided for mixing through breaking wave dissipation at the sea surface mixes the plume in the surf zone leading to strong offshore horizontal density gradients. This paper defines simple, easily-quantified parameters that assess the influence of waves on plumes based on the outflow plume momentum versus wave momentum flux. However, this scaling requires additional research to fully collapse. While this initial study makes a strong case that wave-current interaction can dominate small plume momentum, future work should examine these processes under additional wave and flow rate conditions (i.e. angles, directional spread, heights, etc.) and in the presence of alternative processes that might alter plume structure and mixing such as tides, bathymetric complexities, and wind-driven circulation.

4.3 Chapter 3

In chapter 3, the interplay between seasonal variation in longitudinal density gradients and its impact on transverse circulation of a low inflow estuary in Southern California, representative of many Mediterranean Climate estuaries, was examined. During the experimental time period, hypersalinity was accompanied by increased water temperatures which maintained density gradients in the traditional direction of a canonical freshwater estuary throughout the majority of the basin. In the fall season, shallow bay waters cooled, reducing the overall longitudinal temperature gradient, and shifting the state of the estuary to a parameter space that is more sensitive to hypersaline conditions, thus facilitating inverse longitudinal gradients throughout the inner half of the bay. These inverse gradients reverse the traditional straining induced periodic stratification process leading to increased stratification during flood tides. Moreover, inverse density gradients may be responsible for the inversion of phase averaged baroclinic transverse velocity, indicating that differential advection may be important to the lateral momentum balance. However, full tidal velocity does not support a complete inversion of the flow field, which is likely a result of alternative mechanisms dominating the transverse velocity structure. In light of the immense disparity in the number of observations collected in low-inflow estuaries compared to classical estuaries, there are a great deal more questions than answers, including questions about the roles of friction, channel/basin geometry, density gradient inversion, and Coriolis forcing in dictating intratidal to spring neap variability in inverse conditions, as well as how these processes fit into modern estuarine circulation concepts.

References

Akan, Ç., S. Moghimi, H. Tuba Özkan-Haller, J. Osborne, and A. Kurapov (2017), On the dynamics of the Mouth of the Columbia River: Results from a three-dimensional fully coupled wave-current interaction model, *J. Geophys. Res. Oceans*, *122*(7), 5218–5236, doi:10.1002/2016JC012307.

Anderson, D. M., P. M. Glibert, and J. M. Burkholder (2002), Harmful algal blooms and eutrophication: Nutrient sources, composition, and consequences, *Estuaries*, *25*(4), 704–726, doi:10.1007/bf02804901.

Armi, L., and D. M. Farmer (1986), Maximal two-layer exchange through a contraction with barotropic net flow, *J. Fluid Mech.*, *164*, 27–51, doi:10.1017/S0022112086002458.

Assmann, K. M., A. Jenkins, D. R. Shoosmith, D. P. Walker, S. S. Jacobs, and K. W. Nicholls (2013), Variability of Circumpolar Deep Water transport onto the Amundsen Sea Continental shelf through a shelf break trough, *J. Geophys. Res. Oceans*, *118*(12), 6603–6620, doi:10.1002/2013JC008871.

Bamber, J. L., R. E. M. Riva, B. L. A. Vermeersen, and A. M. LeBrocq (2009), Reassessment of the potential sea-level rise from a collapse of the West Antarctic Ice Sheet, *Science*, *342*(901), 901–903.

Booij, N., R. C. Ris, and L. H. Holthuijsen (1999), A third-generation wave model for coastal regions: 1. Model description and validation, *J. Geophys. Res. Oceans*, *104*(C4), 7649–7666, doi:10.1029/98JC02622.

Bracegirdle, T. J. (2012), Climatology and recent increase of westerly winds over the Amundsen Sea derived from six reanalyses, *Int. J. Clim.*, *33*, 843–851.

Brown, J. A., J. H. MacMahan, A. J. H. M. Reniers, and E. B. Thornton (2015), Field Observations of Surf Zone-Inner Shelf Exchange on a Rip-Channeled Beach, *J. Phys. Oceanogr.*, *45*(9), 2339–2355, doi:10.1175/jpo-d-14-0118.1.

Burchard, H., H. Baumert, H. Burchard, and H. Baumert (1998), The Formation of Estuarine Turbidity Maxima Due to Density Effects in the Salt Wedge. A Hydrodynamic Process Study, *J. Phys. Oceanogr.*, *28*(2), 309–321, doi:10.1175/1520-

0485(1998)028¡0309:TFOETM¿2.0.CO;2.

Busecke, J. J. M., and R. P. Abernathey (2019), Ocean mesoscale mixing linked to climate variability, *Sci. Adv.*, *5*(1), eaav5014, doi:10.1126/sciadv.aav5014.

Chadwick, D. B., and J. L. Largier (1999a), The influence of tidal range on the exchange between San Diego Bay and the ocean, *J. Geophys. Res.*, *104*(C12), 29.

Chadwick, D. B., and J. L. Largier (1999b), Tidal exchange at the bay-ocean boundary, *J. Geophys. Res. Oceans*, *104*(C12), 29,901–29,924, doi:10.1029/1999JC900165.

Chadwick, D. B., J. L. Largier, and R. T. Cheng (1996), The role of thermal stratification in tidal exchange at the mouth of San Diego Bay, *Buoyancy Eff. Coast. Estuar. Dyn.*, pp. 155–174.

Clemesha, R. E. S., K. Guirguis, A. Gershunov, I. J. Small, and A. Tardy (2018), California heat waves: their spatial evolution, variation, and coastal modulation by low clouds, *Clim. Dyn.*, *50*(11-12), 4285–4301, doi:10.1007/s00382-017-3875-7.

Cole, K. L., and R. D. Hetland (2015), The Effects of Rotation and River Discharge on Net Mixing in Small-Mouth Kelvin Number Plumes, *J. Phys. Oceanogr.*, *46*(5), 1421–1436, doi:10.1175/JPO-D-13-0271.1.

Craig, P. D., and M. L. Banner (1994), Modeling wave-enhanced turbulence in the ocean surface layer, *J. Phys. Oceanogr.*, *24*(12), 2546–2559.

Craik, A. D. D., and S. Leibovich (1976), A rational model for Langmuir circulations, *J. Fluid Mech.*, *73*(3), 401–426, doi:10.1017/S0022112076001420.

de Boyer Montégut, C., G. Madec, A. S. Fischer, A. Lazar, and D. Iudicone (2004), Mixed layer depth over the global ocean: An examination of profile data and a profile-based climatology, *J. Geophys. Res. Oceans*, *109*(C12), doi:10.1029/2004JC002378.

Dean, R. G. (1991), Equilibrium beach profiles: Characteristics and applications, *J. Coast. Res.*, *7*(1), 53–84.

Delpey, M. T., F. Ardhuin, P. Otheguy, and A. Jouon (2014), Effects of waves on coastal water dispersion in a small estuarine bay, *J. Geophys. Res. Oceans*, *119*(1), 70–86, doi:10.1002/2013JC009466.

Dutrieux, P., J. De Rydt, A. Jenkins, P. R. Holland, H. K. Ha, S. H. Lee, E. J. Steig, Q. Ding, E. P. Abrahamsen, and M. Schröder (2014), Strong sensitivity of Pine Island ice-shelf melting to climatic variability, *Science*, *343*(6167), 174–178.

Fagherazzi, S. (2002), Basic flow field in a tidal basin, *Geophys. Res. Lett.*, *29*(8), 62–1–62–3, doi:10.1029/2001GL013787.

Fagherazzi, S., P. L. Wiberg, and A. D. Howard (2003), Tidal flow field in a small basin, *J. Geophys. Res.*, *108*(C3), 3071, doi:10.1029/2002JC001340.

Farmer, D. M., and L. Armi (1986), Maximal two-layer exchange over a sill and through the combination of a sill and contraction with barotropic flow, *J. Fluid Mech.*, *164*, 53–76, doi:10.1017/S002211208600246X.

Feddersen, F. (2012), Scaling surf zone turbulence, *Geophys. Res. Lett.*, *39*(18), doi: doi:10.1029/2012GL052970.

Feddersen, F., and J. H. Trowbridge (2005), The effect of wave breaking on surf-zone turbulence and alongshore currents: A modeling study, *J. Phys. Oceanogr.*, *35*(11), 2187–2203, doi:10.1175/JPO2800.1.

Fenty, I., and P. Heimbach (2013), Coupled sea ice–ocean-state estimation in the Labrador Sea and Baffin Bay, *J. Phys. Oceanogr.*, *43*, 884–904.

Fong, D. A., and W. R. Geyer (2001), Response of a river plume during an up-welling favorable wind event, *J. Geophys. Res. Oceans*, *106*(C1), 1067–1084, doi: 10.1029/2000JC900134.

Forget, G. (2010), Mapping ocean observations in a dynamical framework: A 2004-06 ocean atlas, *J. Phys. Oceanogr.*, *40*, 1201–1221.

Ganachaud, A., and C. Wunsch (2000), Improved estimates of global ocean circulation, heat transport and mixing from hydrographic data, *Nature*, *408*(6811), 453–457.

Garrett, C. J. R., and H. Loucks (1976), Upwelling Along the Yarmouth Shore of Nova Scotia, *J. Fish. Res. Board Canada*, *33*(1), 116–117, doi:10.1139/f76-013.

Garvine, R. W. (1995), A dynamical system for classifying buoyant coastal discharges, *Cont. Shelf Res.*, *15*(13), 1585–1596.

Garvine, R. W. (1999), Penetration of Buoyant Coastal Discharge onto the Continental Shelf: A Numerical Model Experiment, *J. Phys. Oceanogr.*, *29*(8), 1892–1909, doi: 10.1175/1520-0485(1999)029¡1892:pobcdo¿2.0.co;2.

Gerbi, G. P., R. J. Chant, and J. L. Wilkin (2013), Breaking Surface Wave Effects on River Plume Dynamics during Upwelling-Favorable Winds, *J. Phys. Oceanogr.*, *43*(9), 1959–1980.

Geyer, W. R. (1993), Three-dimensional tidal flow around headlands, *J. Geophys. Res. Oceans*, *98*(C1), 955–966, doi:10.1029/92JC02270.

Geyer, W. R., and P. MacCready (2014), The Estuarine Circulation, *Annu. Rev. Fluid Mech.*, *46*(1), 175–197, doi:10.1146/annurev-fluid-010313-141302.

Giddings, S. N., D. A. Fong, and S. G. Monismith (2011), Role of straining and advection in the intratidal evolution of stratification, vertical mixing, and longitudinal dispersion of a shallow, macrotidal, salt wedge estuary, *J. Geophys. Res.*, *116*(C3), C03,003, doi:10.1029/2010JC006482.

Giddings, S. N., D. A. Fong, S. G. Monismith, C. C. Chickadel, K. A. Edwards, W. J. Plant, B. Wang, O. B. Fringer, A. R. Horner-Devine, and A. T. Jessup (2012), Frontogenesis and frontal progression of a trapping-generated estuarine convergence front and its influence on mixing and stratification, *Estuaries and Coasts*, *35*(2), 665–681, doi:10.1007/s12237-011-9453-z.

Giddings, S. N., P. MacCready, B. M. Hickey, N. S. Banas, K. A. Davis, S. A. Siedlecki, V. L. Trainer, R. M. Kudela, N. A. Pelland, and T. P. Connolly (2014), Hindcasts of potential harmful algal bloom transport pathways on the Pacific Northwest coast, *J. Geophys. Res. Oceans*, *119*(4), 2439–2461, doi:10.1002/2013JC009622.

Gille, S. T. (2002), Warming of the Southern Ocean since the 1950s, *Science (80-.).*, *295*, 1275–1277.

Gille, S. T. (2008), Decadal-scale temperature trends in the Southern Hemisphere ocean, *J. Clim.*, *21*, 4749–4765.

Godin, G. (1972), *The Analysis of Tides*, 264 pp., University of Toronto Press.

Grant, S. B., J. H. Kim, B. H. Jones, S. A. Jenkins, J. Wasyl, and C. Cudaback (2005), Surf zone entrainment, along-shore transport, and human health implications of pollution from tidal outlets, *J. Geophys. Res. Oceans*, *110*(C10), doi:10.1029/2004JC002401.

Gräwe, U., J.-O. Wolff, and J. Ribbe (2009), Mixing, hypersalinity and gradients in Hervey Bay, Australia, *Ocean Dyn.*, *59*(5), 643–658, doi:10.1007/s10236-009-0195-4.

Grimes, C. B., and M. J. Kingsford (1996), How do Riverine Plumes of Different Sizes Influence Fish Larvae: do they Enhance Recruitment?, *Mar. Freshw. Res.*, *47*(2), 191–208.

Groeskamp, S., S. M. Griffies, D. Iudicone, R. Marsh, A. G. Nurser, and J. D. Zika (2019), The water mass transformation framework for ocean physics and biogeochemistry, *Ann. Rev. Mar. Sci.*, *11*(1), 271–305, doi:10.1146/annurev-marine-010318-095421.

Guymer, I., and J. West (1991), Field studies of the flow structure in a straight reach of the conwy estuary, *Estuar. Coast. Shelf Sci.*, *32*(6), 581–596, doi:10.1016/0272-7714(91)90076-N.

Hally-Rosendahl, K., F. Feddersen, D. B. Clark, and R. T. Guza (2015), Surfzone to inner-shelf exchange estimated from dye tracer balances, *J. Geophys. Res. Oceans*, *120*(9), 6289–6308, doi:10.1002/2015JC010844.

Hansen, D. V., and M. Rattray (1965), Gravitational circulation in straits and estuaries, *J. Mar. Res.*, *23*, 104–122.

Heimbach, P., and M. Losch (2012), Adjoint sensitivities of sub-ice-shelf melt rates to ocean circulation under the Pine Island Ice Shelf, West Antarctica, *Ann. Glaciol.*, *53*, 59–69.

Hetland, R. D. (2005), Relating river plume structure to vertical mixing, *J. Phys. Oceanogr.*, *35*(9), 1667–1688, doi:10.1175/JPO2774.1.

Heywood, K., L. Biddle, L. Boehme, P. Dutrieux, M. Fedak, A. Jenkins, R. Jones, J. Kaiser, H. Mallett, A. Naveira Garabato, I. Renfrew, D. Stevens, and B. Webber (2016), Between the devil and the deep blue sea: The role of the Amundsen Sea continental shelf in exchanges between ocean and ice shelves, *Oceanography*, *29*(4), 118–129, doi:10.5670/oceanog.2016.104.

Hibler, W. D., and K. Bryan (1987), A diagnostic ice–ocean model, *J. Phys. Oceanogr.*, *17*, 987–1015.

Holland, P. R., A. Jenkins, and D. M. Holland (2008), The response of ice shelf basal melting to variations in ocean temperature, *J. Clim.*, *21*, 2558–2572.

Horner-Devine, A. R., R. D. Hetland, and D. G. MacDonald (2015), Mixing and transport in coastal river plumes, *Annu. Rev. Fluid Mech.*, *47*(1), 569–594.

Hosseini, S. T., and S. M. Siadatmousavi (2018), Field observations of hypersaline runoff through a shallow estuary, *Estuar. Coast. Shelf Sci.*, *202*, 54–68, doi:10.1016/J.ECSS.2017.12.003.

Howard, M. D. A., M. Sutula, D. A. Caron, Y. Chao, J. D. Farrara, H. Frenzel, B. Jones, G. Robertson, K. McLaughlin, and A. Sengupta (2014), Anthropogenic nutrient sources rival natural sources on small scales in the coastal waters of the Southern California Bight, *Limnol. Oceanogr.*, *59*(1), 285–297, doi:10.4319/lo.2014.59.1.0285.

Hughes, C. W., and B. A. de Cuevas (2001), Why western boundary currents in realistic oceans are inviscid: A link between form stress and bottom pressure torques, *J. Phys. Oceanogr.*, *31*, 2871–2885.

Jacobs, S. S., A. Jenkins, G. F. Giulivi, and P. Dutrieux (2011), Stronger ocean circulation and increased melting under Pine Island Glacier ice shelf, *Nat. Geosci.*, *4*, 519–523.

Jenkins, A., P. Dutrieux, S. S. Jacobs, S. D. McPhail, J. R. Perrett, A. T. Webb, and D. White (2010), Observations beneath Pine Island Glacier in West Antarctica and implications for its retreat, *Nat. Geosci.*, *3*, 468–472.

Jenkins, A., P. Dutrieux, S. Jacobs, E. Steig, H. Gudmundsson, J. Smith, and K. Heywood (2016), Decadal ocean forcing and Antarctic Ice Sheet response: Lessons from the Amundsen Sea, *Oceanography*, *29*(4), 106–117, doi:10.5670/oceanog.2016.103.

Jenkins, A. D. (1989), The use of a wave prediction model for driving a near-surface current model, *Dtsch. Hydrogr. Zeitschrift*, *42*(3), 133–149, doi:10.1007/bf02226291.

Johnson, A. E., B. S. Powell, and G. F. Steward (2013), Characterizing the effluence near Waikiki, Hawaii with a coupled biophysical model, *Cont. Shelf Res.*, *54*, 1–13.

Jones, G. R., J. D. Nash, R. L. Doneker, and G. H. Jirka (2007), Buoyant surface discharges into water bodies. I: Flow classification and prediction methodology, *J. Hydraul. Eng.*, *133*(9), 1010–1020.

Joughin, I., and R. B. Alley (2011), Stability of the West Antarctic Ice Sheet in a warming world, *Nat. Geosci.*, *4*, 506–513.

Joughin, I., B. E. Smith, and B. Medley (2014), Marine ice sheet collapse potentially under way for the Thwaites Glacier Basin, West Antarctica, *Science (80-.).*, *344*(6185), 735–738.

Kalansky, J., D. Cayan, K. Barba, L. Walsh, K. Brouwer, and D. Boudreau (2018), San Diego Summary Report. California's Fourth Climate Change Assessment. Publication number: SUM-CCCA4-2018-009, *Tech. rep.*, University of California, San Diego, San Diego, CA.

Kalkwijk, J. P. T., and R. Booij (1986), Adaptation of secondary flow in nearly-horizontal flow, *J. Hydraul. Res.*, *24*(1), 19–37, doi:10.1080/00221688609499330.

Kirby, J. T. (2017), Recent advances in nearshore wave, circulation, and sediment transport modeling, *J. Mar. Res.*, *75*(3), 263–300, doi:10.1357/002224017821836824.

Kumar, N., and F. Feddersen (2017a), The effect of Stokes drift and transient rip currents on the inner shelf. Part II: With stratification, *J. Phys. Oceanogr.*, *47*(1), 243–260, doi:10.1175/JPO-D-16-0077.1.

Kumar, N., and F. Feddersen (2017b), A new offshore transport mechanism for shoreline-released tracer induced by transient rip currents and stratification, *Geophys. Res. Lett.*, *44*(6), 2843–2851, doi:doi:10.1002/2017GL072611.

Kumar, N., G. Voulgaris, J. C. Warner, and M. Olabarrieta (2012), Implementation of the vortex force formalism in the coupled ocean-atmosphere-wave-sediment transport (COAWST) modeling system for inner shelf and surf zone applications, *Ocean Model.*, *47*, 65–95.

Lacy, J. R., and S. G. Monismith (2001), Secondary currents in a curved, stratified, estuarine channel, *J. Geophys. Res. Oceans*, *106*(C12), 31,283–31,302, doi: 10.1029/2000JC000606.

Lahet, F., and D. Stramski (2010), MODIS imagery of turbid plumes in San Diego coastal waters during rainstorm events, *Remote Sens. Environ.*, *114*(2), 332–344, doi: 10.1016/j.rse.2009.09.017.

Large, W. G., J. C. McWilliams, and S. C. Doney (1994), Oceanic vertical mixing: A review and a model with a nonlocal boundary layer parameterization, *Rev. Geophys.*, *32*, 363–403.

Largier, J. (2010), Low-inflow estuaries: hypersaline, inverse, and thermal scenarios, *Contemp. issues Estuar. Phys.*, pp. 247–272.

Largier, J. L., C. J. Hearn, and D. B. Chadwick (1996), Density structures in low inflow estuaries, *Buoyancy Eff. Coast. Estuar. Dyn.*, pp. 227–241.

Largier, J. L., J. T. Hollibaugh, and S. V. Smith (1997), Seasonally hypersaline estuaries in Mediterranean-climate regions, *Estuar. Coast. Shelf Sci.*, *45*(6), 789–797.

Lentz, S. (2004), The response of buoyant coastal plumes to upwelling-favorable winds, *J. Phys. Oceanogr.*, *34*(11), 2458–2469.

Lentz, S. J., and M. R. Fewings (2012), The wind- and wave-driven inner-shelf circulation, *Ann. Rev. Mar. Sci.*, *4*(1), 317–343.

Lerczak, J. A., and W. R. Geyer (2004), Modeling the lateral circulation in straight, stratified estuaries, *J. Phys. Oceanogr.*, *34*(6), 1410–1428.

Li, C., and J. O'Donnell (1997), Tidally driven residual circulation in shallow estuaries with lateral depth variation, *J. Geophys. Res. Oceans*, *102*(C13), 27,915–27,929, doi: 10.1029/97JC02330.

Li, X., D. M. Holland, E. P. Gerber, and C. Yoo (2014), Impacts of the north and tropical Atlantic Ocean on the Antarctic Peninsula and sea ice, *Nature*, *505*, 538–542.

Longuet-Higgins, M. S. (1970), Longshore currents generated by obliquely incident sea waves: 1, *J. Geophys. Res.*, *75*(33), 6778–6789, doi:10.1029/JC075i033p06778.

Longuet-Higgins, M. S., and R. Stewart (1960), Changes in the form of short gravity waves on long waves and tidal currents, *J. Fluid Mech.*, *8*(4), 565–583.

Losch, M., D. Menemenlis, J.-M. Campin, P. Heimbach, and C. Hill (2010), On the formulation of sea-ice models. Part 1: Effects of different solver implementations and parameterizations, *Ocean Model.*, *33*, 129–144.

Lucas, L. V., J. R. Koseff, S. G. Monismith, J. E. Cloern, and J. K. Thompson (1999), Processes governing phytoplankton blooms in estuaries. II: The role of horizontal transport, *Mar. Ecol. Prog. Ser.*, *187*, 17–30.

Lucas, L. V., J. R. Koseff, S. G. Monismith, and J. K. Thompson (2009), Shallow water processes govern system-wide phytoplankton bloom dynamics: A modeling study, *J. Mar. Syst.*, *75*(1–2), 70–86.

MacCready, P., and W. R. Geyer (2010), Advances in estuarine physics, *Ann. Rev. Mar. Sci.*, *2*(1), 35–58, doi:10.1146/annurev-marine-120308-081015.

Madrak, S. V., R. L. Lewison, J. A. Seminoff, and T. Eguchi (2016), Characterizing response of East Pacific green turtles to changing temperatures: using acoustic telemetry in a highly urbanized environment, *Anim. Biotelemetry*, *4*(1), 22, doi: 10.1186/s40317-016-0114-7.

Marshall, J., and K. Speer (2012), Closure of the meridional overturning circulation through Southern Ocean upwelling, *Nat. Geosci.*, *5*(3), 171–180, doi: 10.1038/ngeo1391.

Martinson, D. G., and D. C. McKee (2012), Transport of warm Upper Circumpolar Deep Water onto the western Antarctic Peninsula continental shelf, *Nature*, *8*, 433–442.

Mazloff, M. R., P. Heimbach, and C. Wunsch (2010), An eddy-permitting Southern Ocean State Estimate, *J. Phys. Oceanogr.*, *40*, 880–899.

Mazzini, P. L. F., J. A. Barth, R. K. Shearman, and A. Erofeev (2014), Buoyancy-driven coastal currents off Oregon during fall and Winter, *J. Phys. Oceanogr.*, *44*(11), 2854–2876, doi:10.1175/jpo-d-14-0012.1.

Merkel & Associates, I. (2018), 2017 San Diego Bay eelgrass inventory update, *Tech. rep.*, U.S. Navy Region Southwest Naval Facilities Engineering Command, San Diego, CA.

Moffat, C., and S. Lentz (2012), On the response of a buoyant plume to downwelling-favorable wind stress, *J. Phys. Oceanogr.*, *42*(7), 1083–1098.

Mouginot, J., E. Rignot, and B. Scheuchl (2014), Sustained increase in ice discharge from the Amundsen Sea Embayment, West Antarctica, from 1973 to 2013, *Geophys. Res. Lett.*, *41*(5), 1576–1584, doi:10.1002/2013GL059069.

Nezlin, N. P., P. M. DiGiacomo, E. D. Stein, and D. Ackerman (2005), Stormwater runoff plumes observed by SeaWiFS radiometer in the Southern California Bight, *Remote Sens. Environ.*, *98*(4), 494–510.

Nidzieko, N. J., J. L. Hench, and S. G. Monismith (2009), Lateral Circulation in Well-Mixed and Stratified Estuarine Flows with Curvature, *J. Phys. Oceanogr.*, *39*(4), 831–851, doi:10.1175/2008jpo4017.1.

Nøst, O. A., M. Biuw, V. Tverberg, C. Lydersen, T. Hattermann, Q. Zhou, L. H. Smedsrud, and K. M. Kovacs (2011), Eddy overturning of the Antarctic Slope Front controls glacial melting in the Eastern Weddell Sea, *J. Geophys. Res.*, *116*(C11), doi:10.1029/2011JC006965.

Nunes, R. A., and J. H. Simpson (1985), Axial convergence in a well-mixed estuary, *Estuar. Coast. Shelf Sci.*, *20*(5), 637–649.

Olabarrieta, M., J. C. Warner, and N. Kumar (2011), Wave-current interaction in Willapa Bay, *J. Geophys. Res. Oceans*, *116*(C12).

Olabarrieta, M., W. R. Geyer, and N. Kumar (2014), The role of morphology and wave-current interaction at tidal inlets: An idealized modeling analysis, *J. Geophys. Res. Oceans*, *119*(12), 8818–8837, doi:10.1002/2014JC010191.

Oppenheimer, M. (1998), Global warming and the stability of the West Antarctic Ice Sheet, *Nature*, *393*, 325–332.

Palóczy, A., S. T. Gille, and J. L. McClean (2018), Oceanic heat delivery to the Antarctic continental shelf: Large-scale, low-frequency variability, *J. Geophys. Res. Oceans*, *123*(11), 7678–7701, doi:10.1029/2018JC014345.

Payne, A. J., A. Vieli, A. P. Shepherd, D. J. Wingham, and E. Rignot (2004), Recent dramatic thinning of the largest West Antarctic ice stream triggered by oceans, *Geophys. Res. Lett.*, *31*, doi:10.1029/2004GL02128.

Peeling, T. J. (1975), A proximate biological survey of San Diego Bay, California, *Tech. rep.*, Naval Undersea Center, San Diego, CA.

Pein, J. U., E. V. Stanev, and Y. J. Zhang (2014), The tidal asymmetries and residual flows in Ems Estuary, *Ocean Dyn.*, *64*(12), 1719–1741, doi:10.1007/s10236-014-0772-z.

Pritchard, H. D., S. R. M. Ligtenberg, H. A. Fricker, D. G. Vaughan, M. R. Van˜den˜Broeke, and L. Padman (2012), Antarctic ice-sheet loss driven by basal melting of ice shelves, *Nature*, *484*, 502–505.

Pritchard, M., and D. A. Huntley (2006), A simplified energy and mixing budget for a small river plume discharge, *J. Geophys. Res. Oceans*, *111*(C3), doi:10.1029/2005JC002984.

Purkey, S. G., G. C. Johnson, S. G. Purkey, and G. C. Johnson (2010), Warming of global abyssal and deep Southern Ocean waters between the 1990s and 2000s: Contributions to global heat and sea level rise budgets, *J. Clim.*, *23*(23), 6336–6351, doi: 10.1175/2010JCLI3682.1.

Purkey, S. G., G. C. Johnson, S. G. Purkey, and G. C. Johnson (2013), Antarctic Bottom Water warming and freshening: Contributions to sea level rise, ocean freshwater budgets, and global heat gain, *J. Clim.*, *26*(16), 6105–6122, doi:10.1175/JCLI-D-12-00834.1.

Ralston, D. K., and M. T. Stacey (2005), Longitudinal dispersion and lateral circulation in the intertidal zone, *J. Geophys. Res. Oceans*, *110*(C7), doi:10.1029/2005JC002888.

Reeves, R. L., S. B. Grant, R. D. Mrse, C. M. Copil Oancea, B. F. Sanders, and A. B. Boehm (2004), Scaling and management of fecal indicator bacteria in runoff from a coastal urban watershed in Southern California, *Environ. Sci. Tech.*, *38*(9), 2637–2648, doi:10.1021/es034797g.

Rignot, E., J. L. Bamber, M. R. Van˜den˜Broeke, C. Davis, Y. Li, W. J. Van˜de˜Berg, and E. Van˜Meijgaard (2008), Recent Antarctic ice mass loss from radar interferometry and regional climate modelling, *Nat. Geosci.*, *1*, 106–110.

Rignot, E., S. Jacobs, J. Mouginot, and B. Scheuchl (2013), Ice-Shelf melting around Antarctica, *Science (80-.).*, *341*, 266–270.

Rignot, E., J. Mouginot, M. Morlighem, H. Seroussi, and B. Scheuchl (2014), Widespread, rapid grounding line retreat of Pine Island, Thwaites, Smith, and Kohler glaciers, West Antarctica, from 1992 to 2011, *Geophys. Res. Lett.*, *41*, 3502–3509, doi:10.1002/2014GL060140.

Robertson, R. (2013), Tidally induced increases in melting of Amundsen Sea ice shelves, *J. Geophys. Res.*, *118*(6), 3138–3145.

Roemmich, D., J. Church, J. Gilson, D. Monselesan, P. Sutton, and S. Wijffels (2015), Unabated planetary warming and its ocean structure since 2006, *Nat. Clim. Chang.*, *5*(3), 240–245, doi:10.1038/nclimate2513.

Romero, L., D. A. Siegel, J. C. McWilliams, Y. Uchiyama, and C. Jones (2016), Characterizing storm water dispersion and dilution from small coastal streams, *J. Geophys. Res. Oceans*, *121*(6), 3926–3943, doi:10.1002/2015JC011323.

Rong, Z., R. D. Hetland, W. Zhang, and X. Zhang (2014), Current-wave interaction in the Mississippi-Atchafalaya river plume on the Texas-Louisiana shelf, *Ocean Model.*, *84*, 67–83, doi:http://dx.doi.org/10.1016/j.ocemod.2014.09.008.

Salisbury, J., M. Green, C. Hunt, and J. Campbell (2008), Coastal Acidification by

Rivers: A Threat to Shellfish?, *Eos Trans. Am. Geophys. Union*, *89*(50), 513, doi:10.1029/2008EO500001.

Sallée, J.-B. (2018), Southern Ocean warming, *Oceanography*, *31*(2), doi:10.5670/oceanog.2018.215.

Schmidtko, S., K. J. Heywood, A. F. Thompson, and S. Aoki (2014), Multidecadal warming of Antarctic waters, *Science (80-.).*, *346*(6214), 1227–1231.

Schodlok, M. P., D. Menemenlis, E. Rignot, and M. Studinger (2012), Sensitivity of the ice-shelf/ocean system to the sub-ice-shelf cavity shape measured by NASA Ice-Bridge in Pine Island Glacier, West Antarctica, *Ann. Glaciol.*, *53*, 156–162.

Scully, M. E., W. R. Geyer, J. A. Lerczak, M. E. Scully, W. R. Geyer, and J. A. Lerczak (2009), The influence of lateral advection on the residual estuarine circulation: A numerical modeling study of the Hudson River Estuary, *J. Phys. Oceanogr.*, *39*(1), 107–124, doi:10.1175/2008jpo3952.1.

Semtner, A. J. (1976), A model for the thermodynamic growth of sea ice in numerical investigations of climate, *J. Phys. Oceanogr.*, *6*, 379–389.

Shchepetkin, A. F., and J. C. McWilliams (2005), The regional oceanic modeling system (ROMS): a split-explicit, free-surface, topography-following-coordinate oceanic model, *Ocean Model.*, *9*(4), 347–404.

Simpson, J., W. Bos, F. Schirmer, A. Souza, T. Rippeth, S. Jones, and D. Hydes (1993), Periodic stratification in the Rhine ROM in the North Sea, *Oceanol. Acta*, *16*(1), 23–32.

Simpson, J. H., J. Brown, J. Matthews, and G. Allen (1990), Tidal straining, density currents, and stirring in the control of estuarine stratification, *Estuaries*, doi:10.2307/1351581.

Smith, R. (1977), Long-term dispersion of contaminants in small estuaries, *J. Fluid Mech.*, *82*(1), 129–146, doi:10.1017/S0022112077000561.

Smith, V. H., and D. W. Schindler (2009), Eutrophication science: where do we go from here?, *Trends Ecol. Evol.*, *24*(4), 201–207, doi:https://doi.org/10.1016/j.tree.2008.11.009.

Sorensen, K., B. Swope, and V. Kirtay (2013), Marine ecological index survey of San Diego Bay, *Tech. rep.*, SSC Pacific, San Diego, CA.

Spence, P., O. A. Saenko, W. Sijp, and M. England (2012), The role of bottom pressure torques on the interior pathways of North Atlantic Deep Water, *J. Phys. Oceanogr.*, *42*, 110–125.

Spence, P., S. M. Griffies, M. H. England, A. M. Hogg, O. A. Saenko, and N. C. Jourdain (2014), Rapid subsurface warming and circulation changes of Antarctic coastal waters by poleward shifting winds, *Geophys. Res. Lett.*, *41*(13), 4601–4610, doi: 10.1002/2014GL060613.

St-Laurent, P., J. M. Klinck, and M. S. Dinniman (2013), On the role of coastal troughs in the circulation of warm Circumpolar Deep Water on Antarctic shelves, *J. Phys. Oceanogr.*, *43*(1), 51–64.

Stacey, M. T., S. G. Monismith, and J. R. Burau (1999), Measurements of Reynolds stress profiles in unstratified tidal flow, *J. Geophys. Res. Oceans*, *104*(C5), 10,933–10,949, doi:10.1029/1998JC900095.

Stancanelli, L. M., R. E. Musumeci, and E. Foti (2018), Dynamics of gravity currents in the presence of surface waves, *J. Geophys. Res. Oceans*, *123*, doi: doi:10.1002/2017JC013273.

Steig, E., Q. Ding, D. Battisti, and A. Jenkins (2012), Tropical forcing of Circumpolar Deep Water Inflow and outlet glacier thinning in the Amundsen Sea Embayment, West Antarctica, *Ann. Glaciol.*, *53*, 19–28.

Stewart, A. L., and A. F. Thompson (2015), Eddy-mediated transport of warm Circumpolar Deep Water across the Antarctic Shelf Break, *Geophys. Res. Lett.*, *42*, 432–440, doi:10.1002/2014GL062281.

Stewart, A. L., A. Klocker, and D. Menemenlis (2018), Circum-Antarctic shoreward heat transport derived from an eddy- and tide-resolving simulation, *Geophys. Res. Lett.*, *45*(2), 834–845, doi:10.1002/2017GL075677.

Sverdrup, H. U. (1947), Wind-driven currents in a baroclinic ocean; with application to the equatorial currents of the Eastern Pacific, *Proc. Natl. Acad. Sci.*, *33*, 318–326.

Swart, N. C., S. T. Gille, J. C. Fyfe, and N. P. Gillett (2018), Recent Southern Ocean warming and freshening driven by greenhouse gas emissions and ozone depletion, *Nat. Geosci.*, *11*(11), 836–841, doi:10.1038/s41561-018-0226-1.

Thoma, M., A. Jenkins, D. Holland, and S. Jacobs (2008), Modelling Circumpolar Deep Water intrusions on the Amundsen Sea continental shelf, Antarctica, *Geophys. Res. Lett.*, *35*, doi:10.1029/2008GL034939.

Thompson, A. F., K. J. Heywood, S. Schmidtko, and A. L. Stewart (2014), Eddy transport as a key component of the Antarctic overturning circulation, *Nat. Geosci.*, *7*(12), 879–884.

Thornton, E. B., and R. T. Guza (1986), Surf zone longshore currents and random waves: Field data and models, *J. Phys. Oceanogr.*, *16*(7), 1165–1178, doi:10.1175/1520-

0485(1986)016¡1165:szlcar¿2.0.co;2.

Torregrosa, A., T. O'Brien, and I. Faloon (2014), Coastal fog, climate change, and the environment, *Eos Trans. AGU*, *95*(50), 473–474, doi:10.1002/2014EO500001.

Uchiyama, Y., J. C. McWilliams, and A. F. Shchepetkin (2010), Wave-current interaction in an oceanic circulation model with a vortex-force formalism: Application to the surf zone, *Ocean Model.*, *34*(1–2), 16–35, doi: http://dx.doi.org/10.1016/j.ocemod.2010.04.002.

Umlauf, L., and H. Burchard (2003), A generic length-scale equation for geophysical turbulence models, *J. Mar. Res.*, *61*(2), 235–265, doi:10.1357/002224003322005087.

Valle-Levinson, A. (2008), Density-driven exchange flow in terms of the Kelvin and Ekman numbers, *J. Geophys. Res. Oceans*, *113*(C4), C04,001, doi: 10.1029/2007JC004144.

Valle-Levinson, A., C. Reyes, R. Sanay, A. Valle-Levinson, C. Reyes, and R. Sanay (2003), Effects of bathymetry, friction, and rotation on estuary-ocean exchange, *J. Phys. Oceanogr.*, *33*(11), 2375–2393, doi:10.1175/1520-0485(2003)033¡2375:EOBFAR¿2.0.CO;2.

Venaille, A., G. K. Vallis, and K. S. Smith (2011), Baroclinic turbulence in the ocean: Analysis with primitive equation and quasigeostrophic simulations, *J. Phys. Oceans*, *41*(9), 1605–1623.

Viviano, A., R. E. Musumeci, and E. Foti (2018), Interaction between waves and gravity currents: description of turbulence in a simple numerical model, *Environ. Fluid Mech.*, *18*(1), 117–148, doi:10.1007/s10652-017-9527-y.

Wåhlin, A. K., X. Yuan, G. Björk, and C. Nohr (2010), Inflow of Warm Circumpolar Deep Water in the Central Amundsen Shelf, *J. Phys. Oceanogr.*, *40*, 1427–1434.

Wåhlin, A. K., O. Kalén, L. Arneborg, G. Björk, G. K. Carvajal, H. K. Ha, T. W. Kim, S. H. Lee, J. H. Lee, and C. Stranne (2013), Variability of warm deep water inflow in a submarine trough on the Amundsen Sea Shelf, *J. Phys. Oceanogr.*, *43*, 2054–2070.

Walker, D. P., M. A. Brandon, A. Jenkins, J. T. Allen, J. A. Dowdswell, and J. Evans (2007), Ocean heat transport onto the Amundsen Sea shelf through a submarine glacial trough, *Geophys. Res. Lett.*, *34*, doi:10.1029/2006GL028154.

Walker, D. P., A. Jenkins, K. M. Assmann, D. R. Shoosmith, and M. A. Brandon (2013), Oceanographic observations at the shelf break of the Amundsen Sea, Antarctica, *J. Geophys. Res.*, *118*, 2906–2918.

Walters, S. P., A. L. Thebo, and A. B. Boehm (2011), Impact of urbanization and agriculture on the occurrence of bacterial pathogens and stx genes in coastal waterbodies of central California, *Water Res.*, *45*(4), 1752–1762.

Wang, P. F., R. T. Cheng, K. Richter, E. S. Gross, D. Sutton, and J. W. Gartner (1998), Modeling tidal hydrodynamics of San Diego Bay, California, *J. Am. Water Resour. Assoc.*, *34*(5), 1123–1140, doi:10.1111/j.1752-1688.1998.tb04159.x.

Warner, J. C., C. R. Sherwood, H. G. Arango, and R. P. Signell (2005), Performance of four turbulence closure models implemented using a generic length scale method, *Ocean Model.*, *8*, 81–113.

Warner, J. C., B. Armstrong, R. He, and J. B. Zambon (2010), Development of a Coupled Ocean-Atmosphere-Wave-Sediment Transport (COAWST) Modeling System, *Ocean Model.*, *35*(3), 230–244.

Warren, B. A. (1999), Approximating the energy transport across oceanic sections, *J. Geophys. Res.*, *104*, 7915–7919.

Warrick, J. A., and D. A. Fong (2004), Dispersal scaling from the world's rivers, *Geophys. Res. Lett.*, *31*(4), doi:10.1029/2003GL019114.

Warrick, J. A., P. M. DiGiacomo, S. B. Weisberg, N. P. Nezlin, M. Mengel, B. H. Jones, J. C. Ohlmann, L. Washburn, E. J. Terrill, and K. L. Farnsworth (2007), River plume patterns and dynamics within the Southern California Bight, *Cont. Shelf Res.*, *27*(19), 2427–2448.

Whitworth, T., A. H. Orsi, S. J. Kim, W. D. Nowlin, and R. A. Locarnini (1998), Water masses and mixing near the Antarctic slope front, in *Ocean. Ice, Atmos. Interact. Antarct. Cont. Margin*, edited by S. S. Jacobs and R. F. Weiss, AGU, Washington D. C., doi:10.1029/AR075p0001.

Wijffels, S. E., R. W. Schmitt, H. L. Bryden, and A. Stigebrandt (1992), Transport of freshwater by the oceans, *J. Phys. Oceanogr.*, *22*(2), 155–162.

Williams, J. P., D. J. Pondella II, C. M. Williams, and M. J. Robart (2016), Fisheries inventory and utilization study to determine impacts from El Niño in San Diego Bay San Diego, California for surveys conducted in April and July 2016, *Tech. rep.*, Moore Laboratory of Zoology Occidental College, Los Angeles, CA.

Winant, C. D., G. Gutiérrez de Velasco, C. D. Winant, and G. G. de Velasco (2003), Tidal dynamics and residual circulation in a well-mixed inverse estuary, *J. Phys. Oceanogr.*, *33*(7), 1365–1379, doi:10.1175/1520-0485(2003)033¡1365:TDARCI¿2.0.CO;2.

Wiseman, W. J., and R. W. Garvine (1995), Plumes and coastal currents near large river mouths, *Estuaries*, *18*(3), 509, doi:10.2307/1352368.

Wolanski, E. (1986), An evaporation-driven salinity maximum zone in Australian tropical estuaries, *Estuar. Coast. Shelf Sci.*, *22*(4), 415–424, doi:10.1016/0272-7714(86)90065-X.

Wong, S. H. C., S. G. Monismith, and A. B. Boehm (2013), Simple estimate of entrainment rate of pollutants from a coastal discharge into the surf zone, *Environ. Sci. Tech.*, *47*(20), 11,554–11,561, doi:10.1021/es402492f.

Yang, Z., and T. Wang (2013), Tidal residual eddies and their effect on water exchange in Puget Sound, *Ocean Dyn.*, *63*(8), 995–1009, doi:10.1007/s10236-013-0635-z.

Zhang, J., and W. D. Hibler III (1997), On an efficient numerical method for modeling sea ice dynamics, *J. Geophys. Res.*, *102*, 8691–8702.

Zippel, S., and J. Thomson (2015), Wave breaking and turbulence at a tidal inlet, *J. Geophys. Res. Oceans*, *120*(2), 1016–1031, doi:doi:10.1002/2014JC010025.